Department of Precision and Microsystems Engineering

Improving the accuracy of the topology optimization of turbulent flows

Robert Jan Krol

Report no	**: 2023.011**
Coach	**: Ir. M.J.B. Theulings**
Professor	**: Dr. ir. M. Langelaar**
Specialisation	**: Engineering Mechanics**
Type of report	**: MSc Thesis**
Date	**: February 23, 2023**

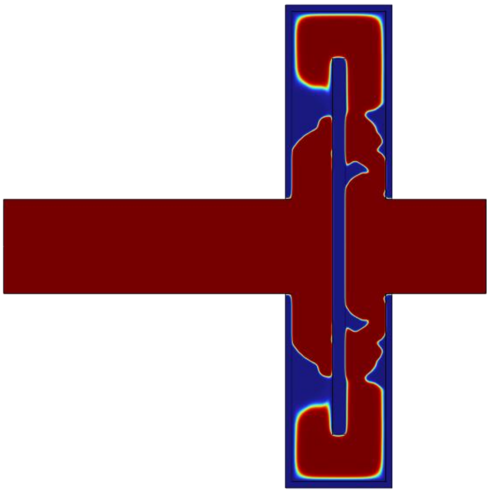

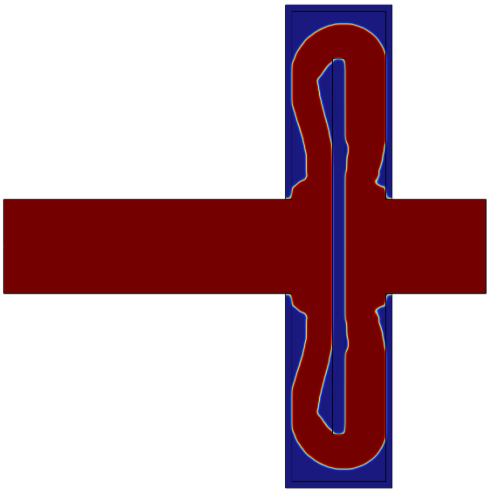

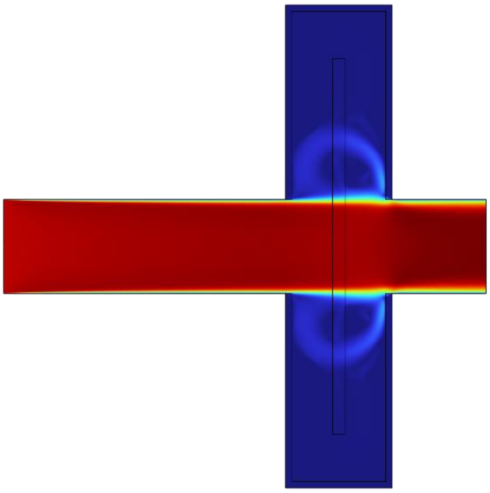

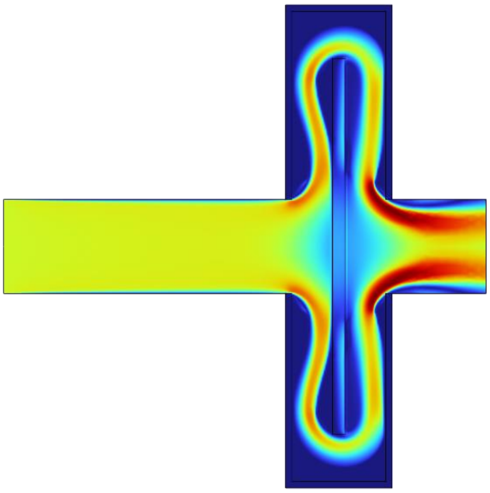

Challenge the future

Improving the accuracy of the topology optimization of turbulent flows

by

R.J. Krol

to obtain the degree of Master of Science
at the Delft University of Technology,
to be defended publicly on Thursday February 23, 2023 at 10:00 AM.

Student number:	4568508	
Project duration:	September 20, 2021 – February 23, 2023	
Thesis committee:	Dr.ir. M. Langelaar,	TU Delft, PME, senior supervisor
	Ir. M.J.B. Theulings,	TU Delft/NLR, PME/AVCE, daily supervisor
	Dr.ir. L.F.P. Noël,	TU Delft, PME
	Dr.ir. M.J.B.M. Pourquie	TU Delft, P&E
	Ir. F.J.P. Hoeven,	Prodrive Technologies, company supervisor
Company supervisor:	Ir. T.B. van der Hout,	Prodrive Technologies

This thesis is confidential and cannot be made public until February 23, 2024.

Preface

This research on the topology optimization of turbulent flows did not always go as expected. I started with ambitious plans to achieve new goals in the field of topology optimization of turbulent flow cooling devices. Unfortunately the addition of heat transport turned out to be too enthusiastic, therefore the work is reduced to topology optimization of turbulent flows only. However, I still found methods to contribute to the field.

The research presented here was conducted with the guidance and support of my daily supervisor Ir. Maarten Theulings. I also want to sincerely thank my senior supervisor Dr.ir. Matthijs Langelaar on his supervision and useful feedback. I would like to express my sincere gratitude to my company supervisors at Prodrive Technologies as well, Ir. Frank Hoeven and Ir. Thomas van der Hout, for their continuous support and knowledge. The expertise of my supervisors provided invaluable insights and guidance throughout my master research and resulted in new insights.

I hope that this master research will serve as a useful resource for others in the field, and that it will inspire further research in the area. Hopefully my initial ambitious plans will be fulfilled by other researchers in the field.

R.J. Krol
Rotterdam, February 2023

Abstract

Silicon based power semiconductors have long been used as the standard in ‘semiconductor technology in power conversion applications’. Recent developments replaces the Silicon with Silicon Carbide as it results in superior performance of the power conversion applications. However, due to the increased performance, challenges regarding heat dissipation emerge and the lifetime of the power semiconductor packaging or power module is compromised. Since this leads to an increase power density, the cooling of the power module is becoming of more importance and the heat sink becomes an interesting component to optimize. The best performance of a heat sink can be obtained when the flow through the device is turbulent. Developing turbulent flow heat sinks by using topology optimization methods can significantly improve the cooling performance compared to the current designs. This work is thus aimed towards improving methods for topology optimization of turbulent flow cooling devices. However, this work focuses on turbulent flow topology optimization only and aims to improve the accuracy of current methods. It is important that the flow physics are accurate since the thermal energy transfer is dependent on the flow field.

The current state-of-the-art method based on the $k - \omega$ turbulence model developed by Dilgen et al. is investigated. A design domain is subdivided into elements since the finite element method (FEM) is used, such that an optimization algorithm is able to turn every element into either fluid or solid with the goal of finding the best performing structure. This density based approach, models the solid domain as a highly impermeably porous material. To inhibit flow in the solid domain a Darcy penalization is added to the momentum equation. Moreover, in the method by Dilgen et al. boundary conditions in the other turbulent fields are also enforced using a similar penalization approach. Weaknesses and errors in the density based method are investigated by comparing solutions to ones computed on a body fitted mesh. It has been found that the largest errors in the solution, by using the state-of-the-art method, appear at the solid/fluid interface in the design. In these regions the penalizations are not applied correctly for the desired boundary conditions. Therefore, in this work it is improved on by the enforcement of the boundary condition by using the *Dilation method*. The Dilation method focuses on the solid/fluid region where it shifts the boundary conditions for the specific dissipation rate (ω) and ensures it reaches the desired value at the solid/fluid interface. Secondly, severe flow leakage is found in the “*porous*” solid domains using the state-of-the-art method. Flow leakage is reduced by using an improved formulation of the maximum Darcy penalization in the solid domain. Finally, the improved approach is investigated in several topology optimization cases and compared to the state-of-the-art Dilgen method. It is shown that by using the new approach, different designs with a better accuracy can be obtained. In an extreme test case, the Dilgen method resulted in an infeasible design which disconnects the flow inlets from the outlets while the new and improved method resulted in a feasible design.

Contents

1

Introduction

Prodrive Technologies (PT) is a company which develops and produces meaningful technologies and has experience in the following fields: Medical, Semiconductor, Infrastructure & Energy, Mobility Solutions and Industrial. The portfolio of Prodrive Technologies can be subdivided in six different categories: Embedded Computing Systems, Motion & Mechatronics, Power Conversion, Controls & Connectivity, Vision & Sensing and Industrial Automation. Power modules and discrete semiconductors devices, which are sometimes produced in-house at PT, are used in nearly all power conversion products of PT. Prodrive Technologies strives for the best possible solutions on the markets they focus on. Therefore, the ‘vertical integration’ way of working is commonly used within Prodrive Technologies, with this way of working PT integrates the most production process stages in-house, which gives PT full freedom of designing their products. This also means that PT manufactures their own custom power modules, which gives them complete freedom in optimizing all the aspects of a power module.

As in most technological fields, new technologies keep being discovered as is the case in the Power Conversion field. The standard Silicon (Si) based power semiconductors are slowly getting replaced by the recent developed Silicon Carbide (SiC) based power semiconductors, where PT mainly uses Silicon Carbide metal-oxide-semicondutor field-effect transistors (SiC MOSFETs). The use of this new material for the power semiconductors highly increases the efficiency of power semiconductors, since all the material properties of SiC based semiconductors are superior to Si based power semiconductors. However, the SiC based power semiconductors are more expensive than the Si based power semiconductors This new technology results in a decreasing size of the power semiconductors whilst the power used in the device remains similar, in other words the power density of the modules is highly increased. Power modules can not convert the power perfectly and losses due to switching and conduction results in temperature swings. The lifetime of the power modules are influenced by these temperature swings of the semiconductors, since these cause stresses in the semiconductor and the components around it. Therefore, a decent cooling system which reduces the temperature swings could be beneficial and ultimately increase the lifetime of the power modules.

Various designs of cooling systems are already available on the market with all kind of different geometries and setups, however to optimize for Prodrive Technologies power modules, PT prefers to develop the cooling system in-house. To push the performance of the cooling system, optimization methods will be involved in the design process. Different kinds of optimization methods could increase the cooling performance of the heat sink, basic optimization methods like size optimization up to the more involved methods as Topology Optimization (TO) are considered. Another way to improve the cooling system is to implement turbulent flow in the design, due to the internal mixing of the fluid, which occurs in turbulent flows, the heat exchange can be increased in comparison to laminar flow. However, simulating and optimizing turbulent flows is a lot more challenging than simulating and optimizing laminar flow. Previous research related to cooling devices within Prodrive Technologies showed promising optimized results for laminar flows, however for turbulent flows no optimized designs were found due to instabilities in the optimization procedure. These instabilities had different causes varying from highly sensitive parameter settings to convection in solid material due to the porosity and also non converging simulations caused problems [1].

In this thesis turbulent flow models will be further developed for use in topology optimization. In **Chapter 2** challenges related to the cooling of the high power SiC MOSFETs power modules will be defined and the research question **‘*Can an accurate method for density-based Topology Optimization of turbulent flows be constructed, which uses the $k-\omega$ turbulence model?*’** is introduced. In **Chapter 3** the necessary background for optimizing a turbulent flow cooling device is given. In **Chapter 4** the state-of-the-art in literature of the Topology Optimization method of turbulent flows by Dilgen et al [2] is examined and some weaknesses are shown inherent to the method. **Chapter 5** elaborates on improvements for a density-based optimization regarding turbulent flows. The improvements are examined in several Topology Optimization cases in **Chapter 6**. Finally, in **Chapter 7** a conclusion can be found followed by further recommendations.

2

Design challenge

This chapter gives a general overview of the problem definition and how the research is developed. First, a power module overview is given in **Section 2.1**. Secondly, in **Section 2.2** the challenges regarding the cooling of a power module are discussed. In **Section 2.3** the optimization methods are presented, followed by the software choice used in **Section 2.4**. Finally, the research question is presented along several subquestions in **Section 2.5**.

2.1. Power module overview

Power modules function as electronic switching devices, which can transform direct current (DC) to alternating current (AC) or the other way around. These power modules are used for different power conversion equipment, for example in motor drives. Prodrive Technologies produces custom power modules in-house (Fig. 2.1) which are on the top end of the market, to remain that position the innovation must proceed. PT sees a trend where more and more power modules are using the new Silicon Carbide (SiC) based semiconductors instead of the standard Silicon (Si) semiconductors. This new material for the power semiconductors can greatly improve the performance of the power modules due to the better material properties of Silicon Carbide in comparison to Silicon but also bring some new challenges with it.

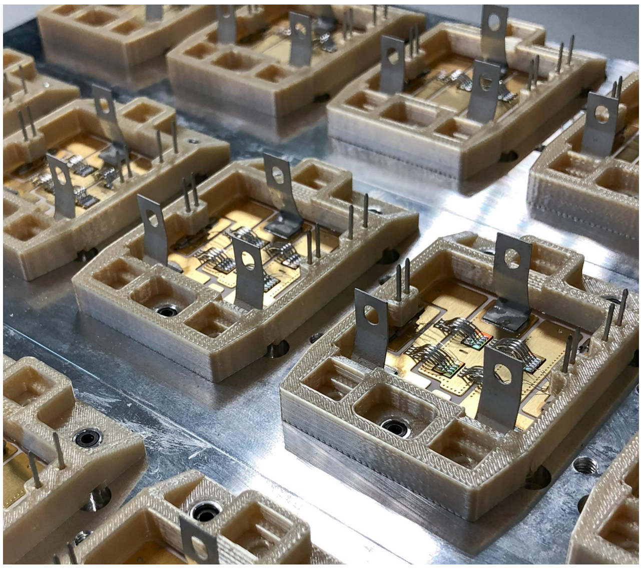

Figure 2.1: Custom power module by Prodrive Technologies

To give a good overview of the challenges caused by the new die material some typical operating circumstances are mentioned. First of all, the power modules PT typically produces are roughly rated at around 1200 volts and can convert energy in the order of kilowatts. The efficiency of these semiconductors is high compared to what is achievable with Si based semiconductors (95-99%) but nonetheless there are still losses in the power semiconductors, in the order of 10-100 W. These dies are typically in the range of 3 mm × 3 mm up to 7 mm × 7 mm and thus the combination of these high loads and relatively small geometries results in enormous heat fluxes in the order of $\mathrm{MW/m^2}$ [1]. A power module consists of multiple SiC MOSFETs which are attached to a substrate, the required electrical connections are constructed by electrically conductive circuits. While the power module is in operation heat is produced by the SiC MOSFETs which is dissipated through the power module, resulting in a temperature gradient through the module. Due to this temperature gradient, components are subjected to thermal expansion and the differences of thermal expansion in the components cause stresses in the power module. Frequent load cycles in the power module also results in cycles of these stresses which can finally result in fatigue failure of the power module. This fatigue behavior is highly influencing the lifetime of the power electronic systems which the power module consists of and thus the lifetime of the power module [3]. If PT succeeds in extending the lifetime of the power modules, trade-offs can be made. PT could decide to: stress the parts harder which result in a higher power density with the lifetime it requires; use semiconductors with lower ratings which save costs or increase the switching frequency and thus increase the efficiency while maintaining the required lifetime. Internal research at PT showed that the performance of the power module could be optimized in several ways: electrically, thermally or mechanically. First of all if the power module would be optimized electrically, this would result in improved switching behavior, which decreases losses and which will increase the lifetime of the power module. Secondly the mechanical stresses could be reduced in the power module by selecting materials which have almost the same thermal expansion coefficient, less stresses between the different layers occur which reduces the fatigue of the power module. Finally, the thermal path could be optimized which should reduce the temperature swings throughout the power module. Simulations performed by PT showed that the thermal resistance contribution changes when the semiconductors size decreases. When decreasing the semiconductor size the contribution of the heat sink to the thermal resistance increases. Therefore the most profit could be gained by optimizing the heat sink. A requirement given by PT is that the heat sink should be water cooled so that the power module could be used in all kind of different applications.

2.2. Cooling device overview

As explained in the previous section the new development of the semiconductors brings new challenges along regarding the heat dissipation of the power module. The new use of SiC causes the power semiconductors to become smaller and the heat source to become more of a point load than in previous designs. Thermal simulations of the new power modules performed by PT showed that the heat sink becomes more dominant in the thermal path and thus makes this an interesting part of the power modules to improve. The cooling performance of each device can be influenced by different aspects. First of all, by the behavior of the flow. A flow can be categorized in different regimes: laminar, turbulent and a transition between laminar and turbulent. By ensuring that the flow inside the cooling device is turbulent, the cooling performance can be greatly increased. In a turbulent flow all the particles behave in a random and chaotic way which cause the fluid to mix heavily and as a result of this the heat exchange in the fluid increases. Another way to increase the cooling performance is by developing the ‘ideal’ structure of the cooling device. Therefore, numerical optimization is used to find the best solution to design the ideal cooling devices.

In the remainder of this section the scope of this thesis will be further narrowed down by stating the boundary conditions of the cooling device. These boundary conditions are partly given by Prodrive Technologies and partly based on previous researches performed within Prodrive Technologies. First, it is important to note that the coolant fluid will be water which is a fixed requirement by Prodrive Technologies. Since water is chosen as coolant fluid, it is realistic in this case to assume the fluid will be incompressible and thus compressibility will be outside of the scope of this thesis. Researches within Prodrive Technologies had in common that the Reynolds number is in the order of 10^4, this research will continue on focusing at a Reynolds number in that order. The Reynolds number is an important dimensionless number which can be used to indicate if a flow regime is laminar or turbulent. More detailed description of the Prodrive Technologies researches can be found in appendix A.

Table 2.1: Overview of important requirements

Req.01	Flow regime is turbulent
Req.02	Reynolds number order 10^4
Req.03	Cooling fluid is water
Req.04	The fluid is incompressible

2.3. Optimization methods

Different optimization methods are available nowadays, such as size optimization, shape optimization and Topology Optimization ([4]). Both size and shape optimization require an initial design concept, while this is not necessary in Topology Optimization (TO) as shown in Figure 2.2. In size optimization, the variable input parameters which define the size of features within a given geometry are optimized. In shape optimization, the initial design will be optimized by tracking the given predefined boundaries and adjusting them throughout the domain, until the most optimal design is reached. In Topology Optimization the optimal material distribution is searched within a given design domain for a given objective under specific boundary conditions. The design in this case is not based on an initial design which leads to geometries which outperform the designs created by sizing or shape optimization. The geometries developed by TO are closer to the global optimum instead of forced into a constrained local optimum. This is also the main reason why TO will be used as the optimization method in the remainder of this thesis. The different optimization methods are graphically shown in Figure 2.2. In TO different methods are developed to execute the optimization process. The Level-set method and Density method are the two most common TO methods and will be shortly discussed in Subsections 2.3.1 and 2.3.2 respectively.

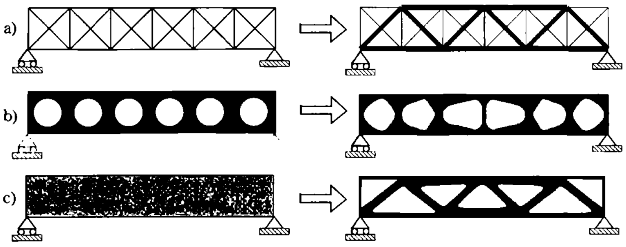

Figure 2.2: Three different optimization methods. a) Sizing optimization, b) Shape optimization and c) Topology optimization. Source: [4]

2.3.1. Level-set based topology optimization

The first level-set based method was proposed by Osher and Sethian [5]. The level-set method makes use of a function called the Level-Set Function (LSF), this LSF is used to define the material distribution within the specified domain. For example, the sign of the LSF can be used to distinguish between the solid and fluid domain, a negative sign represents the solid then a positive sign indicates there is void. If the LSF is zero then the boundary between solid and void is explicitly defined. Since the boundary is explicitly defined by the LSF, a crisp boundary between the solid and void is created. The limits and constraints of a LSF are updated using the sensitivities of the objective with respect to the LSF. The update procedure can influence different aspects of the optimization process like the efficiency and convergence rate and the final result as well. Update procedures can be subdivided in two separate classes [6]:

1. Quasi-temporal process
2. Mathematical programming

The Level-Set Function can be updated by using the Hamilton-Jacobi (HJ) equation which can be assigned to the first class. The HJ equation describes the movement of the boundaries over the optimization iterations and is regulated by a design velocity field $\vec{v}$,

$$\frac{\partial \phi}{\partial \tau} + \nabla \phi \cdot \vec{v} = 0, \tag{2.1}$$

where ϕ is the LSF and the pseudo time is represented by τ which represents the iterations in the optimization process. When the velocity converges to zero and the LSF stagnates, the optimum of the optimization process is reached. The HJ method is rather complex and for particular optimization problems, tuning a large number of algorithmic steps is required [6].

The second class covers mathematical programming methods, which is getting used more often in the level-set method recently. These mathematical programming methods use optimizers which control the LSF. The Method of Moving Asymptotes (MMA)[7] is the most popular optimizer to use nowadays [6].

One of the difficulties in the level-set approach is the fact that the interface generated by the LSF can not be discretely mapped onto a structural mesh [3]. Different methods can be used to solve this problem. First, the 'Ersatz material approach' which creates a transition between the void and solid, however, thus resulting in some areas with intermediate densities which removes the crisp boundary. Although the Ersatz approach has some similarities to density-based methods, in the Ersatz approach the boundaries are still controlled by the LSF. Secondly, the level-set method limits the generation of new boundaries which causes this method to be more dependent on the initial design, since no new boundaries are generated during the optimization process [3]. However, this can be solved by allowing the level-set method to nucleate holes which can be achieved with topological derivatives [6].

2.3.2. Density based topology optimization

Bendsøe and Kikuchi proposed the density method (also known as the material distribution method) for the first time in their topology optimization research [8] and further expanded on the subject in their book [4]. In the density based method we represent the design by subdividing the design space into small elements to which we attach continuous parameters. The design parameters range from 0 (a solid element) to 1 (a void or fluid element). Therefore elements in the optimization domain do not have discrete values and thus require intermediate material properties. To obtain these intermediate material properties, interpolation methods are used which are dependent on the density variable. Each iteration step consists of performing a finite element analysis, after which a sensitivity analysis of the design variables with respect to a set of objectives and constraints is performed. In the last step the design variables are updated, if the solution is converged the results can be plotted. A flowchart of this process is shown in Figure 2.3.

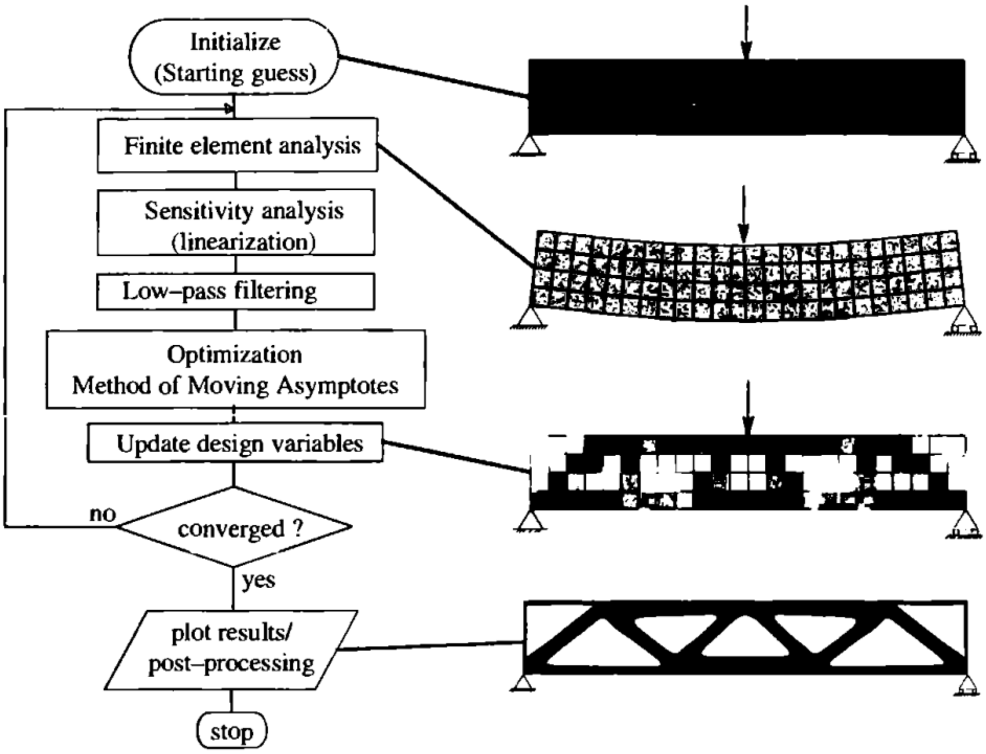

Figure 2.3: The flow of computations for topology optimization using the density method and a MMA optimizer. Source: [4]

2.3.3. Optimization choice

Both Topology Optimization methods have their advantages and disadvantages for the optimization process. A major advantage of the Level-set method is the crisp boundaries which are obtained on the interface between solid and void. However, the Ersatz material approach removes most of the aforementioned advantage. From the previous literature survey ([9]) it is known that the most turbulent flow topology optimizations are performed with the Density method, which makes this a promising method. Papers by Dilgen et al. [2] and [10] showed promising results on the density based topology optimization of turbulent flow with the $k - \omega$ model as this is researched in the literature survey [9]. In this work the choice is made to work with the density based method as it builds upon previous work within Prodrive Technologies.

2.4. Software packages

There are different software packages available for Computational Fluid Dynamics (CFD) analysis, varying from open source software like OpenFOAM to licensed software like Simcenter STAR-CCM+. To quickly narrow down all the available software packages, a Topology Optimization trade-off table created by van der Hout [11] is used as starting point. This table is updated and can be found in Appendix **??**. Many software packages are only focused on structural optimization and are thus not viable for this research, since multiphysics (thermofluid solver) is a requirement. The four remaining packages which have a multiphysics solver are shown in Table 2.2. Secondly, the chosen Topology Optimization method is the density method and thus it is required that the software package is provided with this method, this accounts for the COMSOL Multiphyiscs, OpenFOAM and Autodesk Nastran packages. Thirdly, the $k - \omega$ model is used as a starting point as being state-of-the-art in this thesis research and is therefore the third requirement which has to be included in the software package. From the remaining three packages this is only valid for COMSOL Multiphysics and OpenFOAM. Both software packages have the possibility for Automatic Differentiation (AD) which is an important feature in TO for determining the sensitivities, a small difference is that it is directly included by COMSOL Multiphysics where for OpenFOAM an additional tool is required. It can thus be concluded that COMSOL Multiphysics and OpenFOAM are both suitable packages for this thesis. Since there is already some user experience within PT and the author already has experience with COMSOL Multiphysics makes this the most ideal software for this thesis.

Table 2.2: Final trade off software packages

Software package	**Density based TO**	**$k - \omega$ model**	**Automatic Differentiation**
COMSOL Multiphysics [12]	Yes	Yes	Yes
STAR-CCM+ [13]	No	Yes	No
OpenFOAM [14]	Yes	Yes	Yes
Autodesk Nastran [15]	Yes	No	No

2.5. Research question

In Section 2.1, it is shown that the development of new power modules causes increased heat generation in the module which needs to be dissipated. As explained it is of importance to keep the temperatures in the die as low as possible and the temperature swings within limits. A decrease of these temperature swings and maximum temperatures will increase the power modules' lifetime significantly. Topology Optimization of turbulent-flow cooling systems could be a powerful tool to obtain an improved cooling device for the power module. Topology Optimization of turbulent-flow cooling devices can be seen as a successive process where first the flow physics are solved and secondly the heat transport. Therefore it is important that the flow physics are solved accurately before they are used to determine the heat transport. The scope of this work is therefore narrowed down to the Topology Optimization of turbulent flows only. A previous literature research [9] showed there are some published papers on the Topology Optimization of turbulent-flow cooling devices with interesting results. These papers presents different obtained designs and thus the functionality of the Topology Optimization of turbulent-flow cooling devices. However, the found papers do not comment on the accuracy between the optimized designs and there respective verification models. Therefore the accuracy of the current methods is questioned. This leads us to the research question ***'Can an accurate method for density-based Topology Optimization of turbulent flows be constructed, which uses the $k - \omega$ turbulence model?'***. To answer this research question several sub-questions have been examined:

1. *'What is the state-of-the-art in density-based turbulent-flow Topology Optimization using the $k - \omega$ model?'*
2. *'What are the main sources of errors in the state-of-the-art density-based turbulent-flow Topology Optimization?'*
3. *'How can the accuracy of the state-of-the-art density-based turbulent-flow Topology Optimization be improved?'*
4. *'Are the developed improvements on the density-based model also effective in combination with Topology Optimization?'*

3

Topology optimization of laminar and turbulent thermo-fluid systems

In this chapter the relevant background information regarding the Topology Optimization of turbulent flows is presented. The first section, Section 3.1, introduces a general TO statement. Secondly, in Section 3.2 the laminar and turbulent flow models are presented after which they are adapted for density-based TO. In Section 3.3 a more in-depth explanation of the density-based TO is given including the relevant filtering methods. Additionally in Appendix B.1 background information regarding the thermal convection-diffusion for Topology Optimization can be found.

3.1. General topology optimization statement

A general optimization problem on design domain $\vec{x} \in \Omega$ is written in the following form [16],

$$\boxed{\begin{array}{lll} \underset{\gamma(\vec{x})}{\text{minimize}} & H(\boldsymbol{u}(\gamma), \gamma(\vec{x})) & \\ \text{subject to} & R\,(u(\vec{x}), \gamma(\vec{x})) = 0, & \vec{x} \in \Omega, \\ & R_\Gamma(u(\vec{x}), \partial u(\vec{x})/\partial \vec{x}, \gamma(\vec{x}), \vec{x}) = 0, & \vec{x} \in \Gamma, \\ & g_i\,(s(\vec{x})) \leq 0, & i \in I,\ \vec{x} \in \Omega, \end{array}} \tag{3.1}$$

where $\gamma(\vec{x})$ is the design variable field which is used to minimize the objective function H, R is the Partial Differential Equation (PDE) constraint on domain Ω with boundary conditions R_Γ and g_i are the inequality constraints on the optimization problem. In our examples PDE constraint R will contain the Reynolds-averaged Navier-Stokes (RANS) equations for turbulent flow.

To solve the optimization problem the Finite Element Method (FEM) is used to model the physics. In FEM the domain is discretized and the solution is approximated using numerical methods. To perform TO additional methods are required. Therefore, the density-based Topology Optimization approach is used in which the design variable γ is a continuous variable bounded by the values 0 and 1. However, we discretize the design field $\gamma(\vec{x})$ by adding a density value to each of the discretized elements. Since the design domain is discretized by the design variable, the flow and thermal models must depend on the continuous variable γ to represent the solid/fluid physics.

3.2. Flow physics for topology optimization

First of all a distinction can be made between laminar and turbulent flows. A laminar flow is characterized by smooth streamlines and a highly ordered motion [17], which makes laminar flows in general less complex to model and analyze. The flow can be described by the balance between viscous and inertial forces. If the viscous forces are dominant, the flow is laminar, while in a turbulent flow the inertial forces are dominant. Therefore, a ratio between these two forces is introduced in the so called Reynolds number [18]:

$$Re = \frac{\rho U L}{\mu} \approx \frac{\text{Inertia}}{\text{Viscosity}}, \tag{3.2}$$

where ρ is the density in kg/m^3, U is the velocity in m/s, L is the characteristic length in m and μ is the dynamic viscosity in $\text{kg/(m\,s)}$. The Reynolds number thus gives an indication if the flow is laminar or turbulent. Figure 3.1 shows how the flow regimes relate to the Reynolds number. In the following subsections the laminar and turbulent flow models are explained.

$0 < \mathrm{Re} < 1$:	highly viscous laminar “creeping” motion
$1 < \mathrm{Re} < 100$:	laminar, strong Reynolds number dependence
$100 < \mathrm{Re} < 10^3$:	laminar, boundary layer theory useful
$10^3 < \mathrm{Re} < 10^4$:	transition to turbulence
$10^4 < \mathrm{Re} < 10^6$:	turbulent, moderate Reynolds number dependence
$10^6 < \mathrm{Re} < \infty$:	turbulent, slight Reynolds number dependence

Figure 3.1: Reynolds number relation to different flow regimes obtained from [18].

3.2.1. Modeling of laminar flows

Laminar flow is ordered and no chaotic behavior occurs which makes the flow predictable and easier to model than chaotic turbulent flow. In laminar flow the viscous forces are dominant over the inertial forces and no turbulent behavior is present. Laminar flows for incompressible fluids are described by the Navier-Stokes (N-S) equations [19]:

$$\underbrace{\rho\frac{\partial\vec{u}}{\partial t} + \rho(\vec{u}\cdot\nabla)\vec{u}}_{\text{Inertial forces}} = \underbrace{\mu\nabla^2\vec{u}}_{\text{Viscous forces}} - \underbrace{\nabla p}_{\text{Pressure forces}} + \underbrace{\vec{F}}_{\text{External body forces}}, \tag{3.3}$$

$$\nabla\cdot\vec{u} = 0, \tag{3.4}$$

where ρ is the density of the fluid in $\mathrm{kg/m^3}$, $\vec{u}$ is the velocity field of a fluid in $\mathrm{m/s}$, t is time in s, μ is the dynamic viscosity in $\mathrm{kg/(m\,s)}$, p is the fluid pressure field in Pa and all the external forces are presented by $\vec{F}$ in $\mathrm{N/m^3}$. The Navier-Stokes equations can be seen as a force balance between the inertial forces on the left-hand side and the viscous forces, pressure forces and external body forces on the right-hand side. Equation 3.4 is derived from the formula of conservation of mass:

$$\frac{\partial\rho}{\partial t} + \nabla\cdot(\rho\vec{u}) = 0. \tag{3.5}$$

Because the flow is assumed incompressible and ρ is thus constant, derivatives of ρ are zero and thus Equation 3.5 can be simplified to Equation 3.4 [19].

3.2.2. Modeling of turbulent flows

The modeling of turbulent flows is much more complex than laminar flows. Unlike laminar flows, a turbulent flow is chaotic and mixing occurs in the flow, this makes a turbulent flow unpredictable and thus more difficult to model. In turbulent flow eddies (a vortex-like structure or swirl in a fluid [20]) with different time and length scales occur and interact with each other in a complex way. In CFD simulations, the Navier-Stokes equations could be used to solve a turbulent flow, this method is called Direct Numerical Simulation (DNS) which is an accurate way to model turbulent flows but also computationally expensive. The high computational cost is caused by the fine mesh scale and the transient solver which are required [21]. Another method to model turbulent flows is the Reynolds-averaged Navier-Stokes (RANS) equation and the accompanying closure models. Only the $k-\omega$ model is explained as this model came out as most promising in the literature research ([9]), and is therefore used in this work.

RANS equations and the $k-\omega$ closure model

The essence of the RANS equations is based on the fact that the turbulent quantities can be derived from the flow to a sufficient level of accuracy. To obtain the RANS equations the velocity and pressure in the general Navier-Stokes equations are replaced by an averaged velocity and pressure. This gives the following results for conservation of mass and conservation of momentum respectively [21],

$$\rho\nabla\cdot\vec{U} = 0, \tag{3.6}$$

$$\underbrace{\rho\frac{\partial\vec{U}}{\partial t} + \rho\vec{U}\cdot\nabla\vec{U}}_{\text{Inertial forces}} = -\underbrace{\nabla P}_{\text{Pressure forces}} + \underbrace{\nabla\cdot(\mu+\mu_T)(\nabla\vec{U}+(\nabla\vec{U})^T)}_{\text{Viscous + Reynolds stresses}} + \underbrace{\vec{F}}_{\text{External body forces}}. \tag{3.7}$$

In the equation for conservation of momentum a new variable μ_T is introduced, which is called the turbulent dynamic viscosity. By introducing this new unknown the RANS equations can not be solved and thus additional equations are required, these equations are called the RANS closure models. The closure model which is used in this work is the two equation $k-\omega$ model, this model adds two additional equations to the RANS model and solves for two additional turbulent quantities. The first equation concerns the turbulent kinetic energy k:

$$\rho\,(\nabla k)\cdot\vec{u} = \nabla\cdot\left[\left(\mu+\mu_T\sigma_k^*\right)\nabla k\right] + P_k - \beta_0^*\rho\omega k, \tag{3.8}$$

where $\sigma_k^* = \frac{1}{2}$ and $\beta_0^* = 0.09$ are constants. The second equation concerns the specific dissipation rate ω:

$$\rho\,(\nabla\omega)\cdot\vec{u} = \nabla\cdot\left[(\mu+\mu_T\sigma_\omega)\,\nabla\omega\right] + \lambda_k\frac{\omega}{k}P_k - \rho\beta_0\omega^2, \tag{3.9}$$

where $\sigma_\omega = \frac{1}{2}$ and $\lambda_k = \frac{13}{25}$ are constants and P_k is a production term given by:

$$P_k = \mu_T\left(\nabla\vec{U} : \left(\nabla\vec{U} + \left(\nabla\vec{U}\right)^T\right)\right). \tag{3.10}$$

By combining the k and ω the turbulent dynamic viscosity can be determined:

$$\mu_T = \rho\frac{k}{\omega}. \tag{3.11}$$

Plugging the turbulent dynamic viscosity back into Equation 3.7 the turbulent $k-\omega$ model is complete. An important behavior of the turbulent specific dissipation rate is the singularity at the wall. The specific dissipation rate ω is large in the areas where the turbulence should be reduced. Close to a solid wall, all turbulent energy should be dissipated and the specific dissipation rate should thus be large. The specific dissipation rate thus has a theoretical singularity to infinity when approaching a solid wall. Since ω can not be infinite at the wall due to numerical reasons, COMSOL introduced a wall boundary condition for the specific dissipation rate (ω_b) which approximates this behavior by,

$$\lim_{l_w\to 0}\omega_b = \frac{6\nu}{\beta_0 l_w^2} \tag{3.12}$$

where β_0 is a constant and l_w is the wall distance in m and is determined by,

$$l_w = \frac{1}{G} - \frac{l_{ref}}{2} \tag{3.13}$$

where l_{ref} is a reference length determined by COMSOL based on the mesh size and G is the reciprocal wall distance computed using:

$$\nabla G\cdot G + \sigma_w G\,(\nabla\cdot\nabla G) = (1+2\sigma_w)\,G^4, \tag{3.14}$$

where σ_w is a smoothing parameter with default value 0.2. The equation for the reciprocal wall distance G is a modified Eikonal equation based on the approach by Fares and Schröder [22]. They derived a Partial Differential Equation to compute the distance from a surface, this equation is useful especially in combination with turbulent flow models. The equation of the ω_b is only active at the so called ‘wall elements’, which are elements adjacent to the wall. By using this boundary condition COMSOL can approach the specific dissipation rate at the wall up to order 10^{16}. This boundary condition is especially important when adapting the $k-\omega$ model for topology optimization.

Modeling of the turbulent boundary layer

In turbulence modeling the near wall region is of great importance, this region is relatively small compared to the entire simulation domain but the solutions from this region propagate to the full domain. In the region near the wall the velocity gradient in the wall normal direction is changing quickly and therefore accurate meshing is required to capture this. Important quantities which are used in turbulence modeling are the dimensionless wall normal distance y^+ and the dimensionless velocity u^+, both given by [23]:

$$y^+ = \frac{yu_\tau}{\nu}, \tag{3.15}$$

$$u^+ = \frac{u}{u_\tau}, \tag{3.16}$$

where y is the distance in the wall normal direction in m, ν is the kinematic viscosity of the fluid in $\mathrm{m^2/s}$ and u_τ is the friction velocity in $\mathrm{m/s}$, which can be determined by [24],

$$u_\tau = \sqrt{\frac{\tau}{\rho}}, \tag{3.17}$$

where τ is the shear stress in $\mathrm{kg/(m\,s^2)}$. The friction velocity or sometimes also referred to as the shear velocity is the relation between the shear stress between the flow layers and the velocity of the flow. In CFD the friction velocity quantity is mostly evaluated at the wall so it can be used in the log-law, therefore the shear stress (τ) is replaced by shear stress at the wall [24],

$$u_\tau = \sqrt{\frac{\tau_w}{\rho}}, \tag{3.18}$$

where τ_w is the wall shear stress in $\mathrm{kg/(m\,s^2)}$. The wall shear stress is the shear stress between the wall and the 'first' flow layer, defined as [24]:

$$\tau_w(x) = \mu \left(\frac{\partial u}{\partial y} \right)_{y=0}, \tag{3.19}$$

where u is the velocity parallel to the wall in $\mathrm{m/s}$.

First of all to characterize turbulent flow it is essential to understand what is happening in the near wall region. This region can be split up in three different regions: the viscous sublayer, the buffer layer and the log-law region, after these regions the free-stream flow starts [25]. Closest the wall the viscous sublayer is located, in this layer the viscous forces dominate the inertial forces and thus the local Reynolds number is relatively low. In this viscous sublayer the dimensionless velocity is linearly dependent on dimensionless wall normal distance, $u^+ = y^+$. This viscous sublayer is thus from the wall up to $y^+ = 5$. Moving further away from the wall, at a $y^+ = 30$ the log-law regime starts. In this region the inertial forces dominate the viscous forces and the Reynolds number is relatively high. In contrast to the viscous sublayer in this region u^+ is not linear with the y^+, but the dimensionless velocity is described by the so called log-law [26],

$$u^+ = \frac{1}{\kappa} ln(y^+) + B, \tag{3.20}$$

where κ is the Von Kármán constant and B is an integration constant, both are based on empirical data and are normally fixed as $\kappa = 0.41$ and $B = 5.2$. In between the viscous sublayer and log-law region ($5 < y^+ < 30$), the buffer layer is located which is a transition area where the flow goes from more or less laminar to turbulent [23]. On overview of the flow regions can be found in Figure 3.2 below. Plotting the u^+ against the y^+ the law of the wall is obtained as shown in Figure 3.3. At an y^+ value of around 11.25 the linear and non-linear lines cross, which is an important intersection which is used in many CFD methods. This intersection is used in CFD methods to make a distinction between the so called 'Low Reynolds' and 'High Reynolds' models, which is explained in the following section.

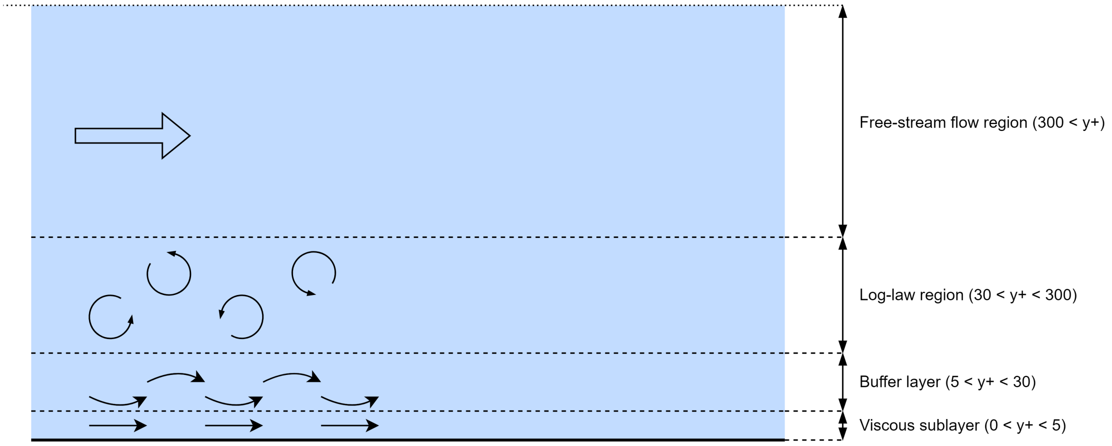

Figure 3.2: Near wall flow regions

'Low Re' versus 'High Re' models

In CFD simulations the 'Low Re' and 'High Re' models refer to the way the flow is resolved close to the wall. In a 'Low Re' model the mesh in the near wall region needs to be very fine and it is required that the first mesh element is placed in the viscous sublayer or at least below the intersection point of $y^+ = 11.25$ (see Fig. 3.4). For this relatively fine mesh the 'Low Re' model can perfectly solve the flow in the near wall region with linear interpolations for the velocity as used throughout the mesh, even despite the very high gradient of the velocity in the near wall region. However, in the 'High Re' models the center of the first mesh cell element is placed in the log-law region. Therefore the interpolation between the mesh elements can not be linear since the behavior of the flow is non-linear, wall functions are introduced here to solve this problem. Wall functions are empirically derived equations and can predict the flow in the near wall region quite well. An advantage of using wall functions is that the mesh elements can be much larger. However, a shortcoming of these 'High Re' models is that the accuracy is less compared to a well used 'Low Re' model. In Figure 3.5 it can

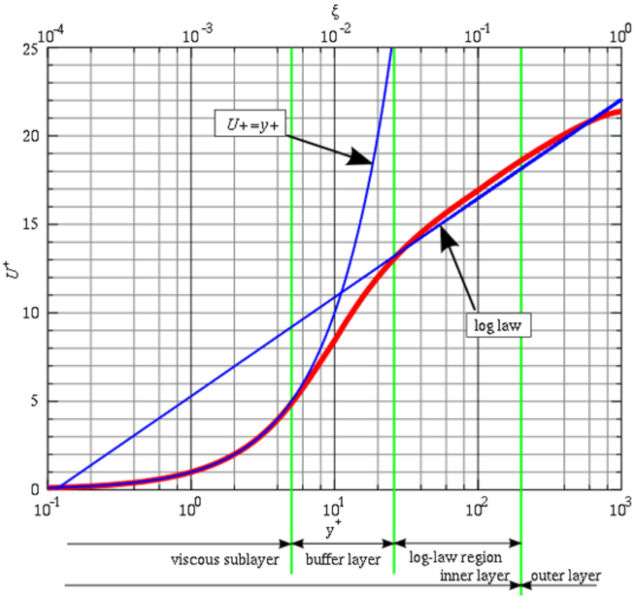

Figure 3.3: The law of the wall, obtained from [27]

be seen that a fine mesh can be used for a 'piecewise' linear interpolation, while for the coarse mesh a wall function is required. The 'Low Re' models thus requires a fine mesh in the near wall region. However, since this is not required in the free-stream a so called body fitted mesh is used to save computation time. The body fitted mesh implements boundary layers close to the wall where small elements of size $h = y^+$ are present, whereas in the free-stream region much larger elements can be used to accurately resolve the flow.

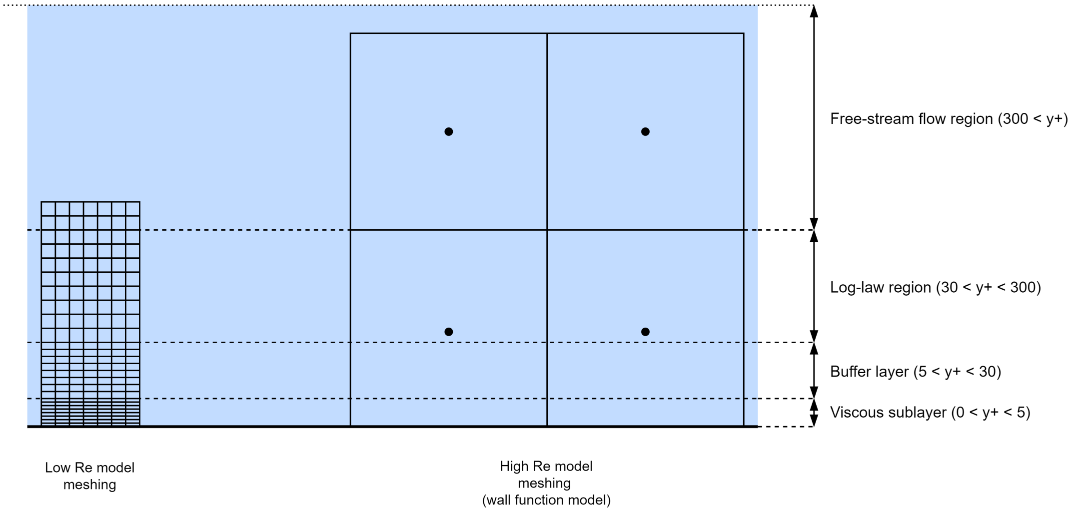

Figure 3.4: Difference between a Low Re model mesh and a High Re model mesh in the near wall region.

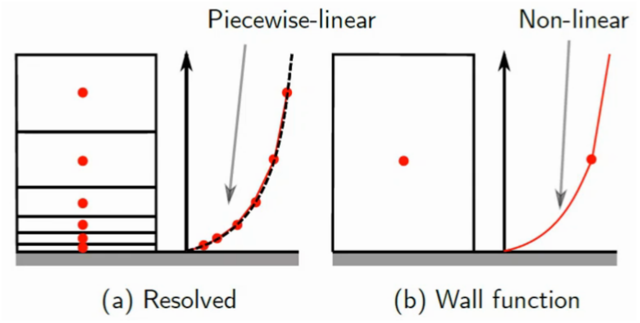

Figure 3.5: The fundamental difference between Low Re and High Re models is shown in this figure. The Low Re models (left) require sufficiently small mesh elements so that the flow can be resolved piecewise-linear. High Re models (right) have significant larger elements where the flow is approximated by non-linear wall functions. Figure obtained from: [28].

3.2.3. Adapting the flow models for topology optimization

The models as explained in the beginning of this section can not directly be applied to Topology Optimization, as they need to be able to continuously describe the solid and fluid domains dependent on the design variable $\gamma(\vec{x})$. We thus aim to introduce a dependence on γ such that one set of flow equations can accurately describe both the fluid region where flow is free, and the solid region where the flow is stagnant ($\vec{u} \to 0$). First the laminar Navier-Stokes equations are adapted. Secondly, the turbulent flow $k-\omega$ model is adapted.

Adapting the Navier-Stokes equations for topology optimization

The topology optimization of a Stokes flow is first introduced by Borrvall and Petersson [29], who introduced the Darcy penalty to use the Navier-Stokes equations in density-based Topology Optimization:

$$\rho(\vec{u}\cdot\nabla)\vec{u} = \nabla\cdot\left[-p\boldsymbol{I} + \mu\left(\nabla\vec{u} + (\nabla\vec{u})^T\right)\right] - \underbrace{\alpha\rho\vec{u}}_{\text{Darcy penalty}}\ , \tag{3.21}$$

where α is the so called impermeability, this impermeability is used to ensure flow becomes stagnant ($\vec{u} \to 0$) in the solid design domain where $\gamma \to 0$. In essence, the Darcy penalization is used to add force in the opposite direction of flow such that it is stopped. In the fluid domain fluids should be free to flow and $\underline{\alpha} = \alpha(\gamma = 1) = 0$ such that no additional force is applied. In the solid domain flow should be stagnant and a high force should be applied which is achieved by $\overline{\alpha} = \alpha(\gamma = 0) \to \infty$. However, due to numerical reasons we cannot use a penalization which is infinitely large and thus introduce a penalization which is sufficiently high to stop the flow [30]. The maximum impermeability can be determined in two ways, the first method is introduced by Kondoh et al. [31] and was later adapted by Li et al. [32],

$$\overline{\alpha} = \left(1 + \frac{1}{Re}\right)\frac{1}{Da}. \tag{3.22}$$

The second method to determine the maximum impermeability is from Olesen et al. [30],

$$\overline{\alpha} = \frac{\nu}{DaL^2}, \tag{3.23}$$

where Da is the Darcy number and L is the characteristic length which depends on the problem specific geometry, for a channel this length is the diameter. To obtain almost impermeable solid material, the Darcy number must be very low, according to Olesen et al. [30] this is the case for $Da \lesssim 10^{-5}$. We determined the extreme values for α namely $\underline{\alpha} = \alpha(\gamma = 1) = 0$ and $\overline{\alpha} = \alpha(\gamma = 0) \to \infty$. However, as said in Subsection 2.3.2, the density design variable can range from 0 which is solid to 1 which is fluid. Therefore we have to couple the impermeability α to the design variable field $\gamma(x)$ which is realized by a convex interpolation function [30]:

$$\alpha(\gamma) = \underline{\alpha} + (\overline{\alpha} - \underline{\alpha})q\frac{1-\gamma}{q+\gamma}, \tag{3.24}$$

where q is the Darcy penalization factor. Since the minimum impermeability is equal to zero we can reduce the interpolation to:

$$\alpha(\gamma) = \overline{\alpha}q\frac{1-\gamma}{q+\gamma}. \tag{3.25}$$

The penalization factor can be adjusted so that a different scaling of the intermediate impermeabilities can be obtained. A low penalization factor results in a sharp interpolation function, meaning the intermediate values are pushed to the extremes. A more linear interpolation is obtained with a high penalization factor. This is demonstrated in Figure 3.6.

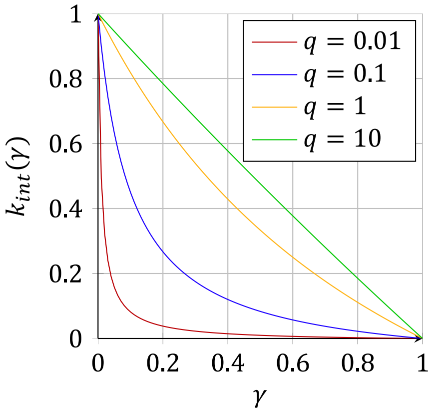

Figure 3.6: Darcy interpolation for different penalization factors, where $k_{int}(\gamma)$ presents the interpolated variable.

Adapting the turbulent k-omega model for topology optimization

For the topology optimization of turbulent flows the governing equations needs to be adapted. Therefore in the RANS equation the Darcy penalization is also introduced:

$$\rho\frac{\partial \vec{U}}{\partial t} + \rho\vec{U}\cdot\nabla\vec{U} = -\nabla P + \nabla\cdot(\mu+\mu_T)\left(\nabla\vec{U} + \left(\nabla\vec{U}\right)^T\right) - \underbrace{\alpha\rho\vec{U}}_{\text{Darcy penalty}} \quad . \tag{3.26}$$

For the $k-\omega$ model, the equations including penalization can be written as [2]:

$$\rho(\nabla k)\cdot\vec{u} = \nabla\cdot\left[\left(\mu+\mu_T\sigma_k^*\right)\nabla k\right] + P_k - \beta_0^*\rho\omega k - \underbrace{\alpha k}_{\text{k-penalty}} \quad , \tag{3.27}$$

$$\rho(\nabla\omega)\cdot\vec{u} = \nabla\cdot\left[\left(\mu+\mu_T\sigma_\omega\right)\nabla\omega\right] + \lambda\frac{\omega}{k}P_k - \rho\beta_0\omega^2 + \underbrace{\alpha\left(\omega_b-\omega\right),}_{\omega\text{-penalty}} \tag{3.28}$$

where α is the impermeability as defined in Eq. 3.25. As shown the *Darcy-* and *k-penalization* have a slightly different form than the *ω-penalization*, this is introduced by Dilgen et al. [2]. The ω_b used by Dilgen et al. is based on the boundary condition given by Menter [33]. Menter uses the distance to the closest cell center near the wall in the boundary condition for ω. Since in Topology Optimization it is difficult to determine this distance, Dilgen et al. replaces this by half the mesh size. In TO it is common to use an uniform grid size and therefore it can be assumed that half the mesh size is always corresponding with the distance to the nearest cell center of the wall. Both boundary conditions are given in the following equation,

$$\omega_b = \frac{60\nu}{\beta_1 y_1^2} = \frac{60\nu}{\beta_1\left(\frac{h}{2}\right)^2} \tag{3.29}$$

where β_1 is a constant with value 0.075, y_1 is that distance from the wall to the cell center nearest at the wall and h is the mesh size in m. In Topology Optimization it is usual to use a uniform mesh, and thus this y_1 value can be approximated by half the mesh size.

3.3. Density-based topology optimization approach

As explained in Section 2.3.2, in this work we investigate *density-based* Topology Optimization. In this approach the optimization domain is divided in mesh elements and each element is assigned a design variable, which in this case is the so called density variable (γ). In the design domain, the solid domain is represented as highly impermeable solid material where $\gamma = 0$ and the fluid domain is a highly permeable porous material where $\gamma = 1$. The ideal optimization process will generate a completely discrete design where only density values of one and zero are present. However, then the optimization could generate designs with small channels with the size of an element, which is most of the time not desired if a small mesh size is used. Secondly, small fluid or solid islands could be generated with the size of one element. Therefore, a blurring filter is used to establish a minimum design length scale [34]. Comparable problems occur in minimum compliance Topology Optimization where checkerboard designs can be generated, as shown in Figure 3.7.

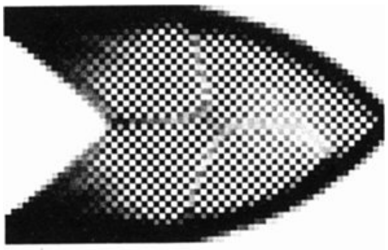

Figure 3.7: Example of a checkerboard structure in a minimum compliance Topology Optimization, where a force is applied on the right side of the structure and the structure is clamped at the left side. Obtained from [35]

Blurring filter

First, the blurring filter is introduced. The blurring filter is used to blur the design such that in a design where only black ($\gamma = 0$) and white ($\gamma = 1$) density variables are present, some gray-scale elements ($\gamma \approx 0.5$) are introduced. The blurring filter determines the density value of an element based on the density values of the elements around it. The size of filter radius R determines the size of the domain around a certain element for which the blurred density is determined by "*averaging*" the densities within the domain. The blurring filter is defined by the following PDE [36],

$$\gamma_f = \gamma_c + r^2\nabla^2\gamma_f, \tag{3.30}$$

where γ_f is the filtered density variable, γ_c is the unfiltered control design variable and $r = 2\sqrt{3}R$ where R is again the filter radius. It is desired that the minimal filtering radius is equal or larger than the used mesh size h. The filtering operation smooths out densities and constructs the density of an element as a weighted average of its own and its neighboring elements. By increasing the filter radius more elements are used by determining the density value of an element. In Figure 3.8 an example is shown with the influence of the filter radius on the density distribution.

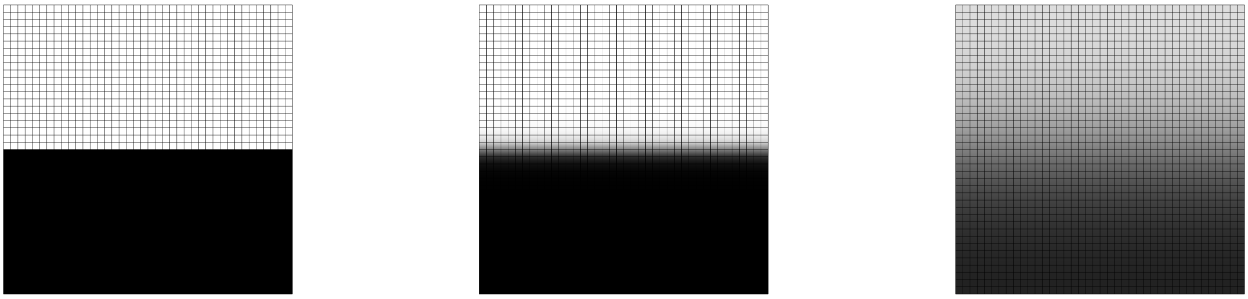

(a) No blurring filter.

(b) Blurring filter with filter radius $R = h$.

(c) Blurring filter with filter radius $R = 10h$.

Figure 3.8: The shown domains consists of elements with mesh size h, different radii are used in the blurring filtering.

Heaviside projection filter

The blurring filter is thus introduced to prevent the solution from having undesired topologies. However, the blurring filter could generate large areas with gray elements which is also an undesired, as the large areas of gray elements are presenting an intermediate porous area which is not in agreement with the physics in the model. To reduce the gray regions a Heaviside projection filter is used to obtain a more discrete domain. The Heaviside projection filter has different formulations, in this work the formulation by Wang et al. [37] is used as this formulation is implemented in COMSOL as well,

$$H(\gamma) = \frac{\tanh(\beta(\gamma_f - \eta)) + \tanh(\beta\eta)}{\tanh(\beta(1-\eta)) + \tanh(\beta\eta)}, \tag{3.31}$$

where β determines the projection slope and η is the projection threshold. Using a higher β increases the projection slope and causes the filter to push a gray design into an increasingly black/white design. The projection slope regulates the steepness of the Heaviside projection filter, a high projection slope means a more binary result. The projection point can be used to shift the Heaviside projection filter which allows to project the γ_f below a certain value to push either to 0 or 1. Different settings could be used as shown in Figure 3.9.

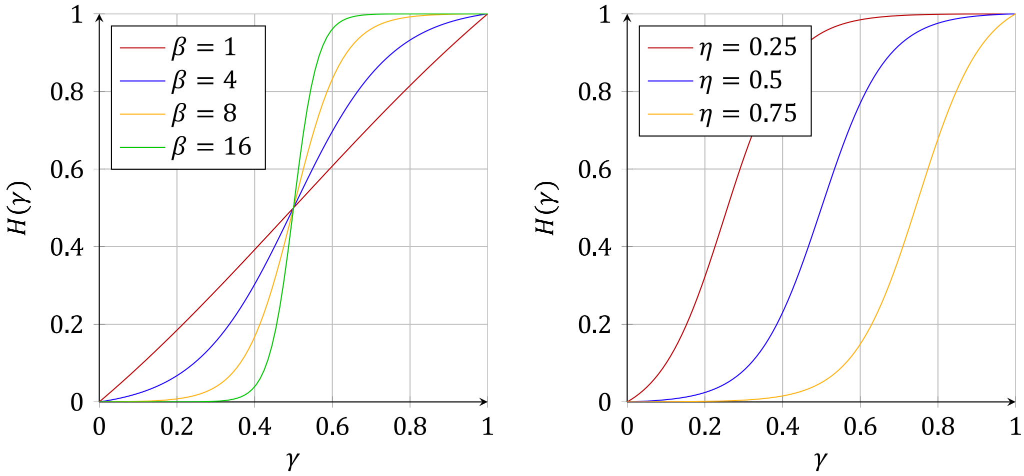

(a) Heaviside projection filter for different projection slopes.

(b) Heaviside projection filter for different projection thresholds.

Figure 3.9: Different settings for the Heaviside projection filter

The complete density filtering process consists of two steps: first the blurring filter is applied to the design, followed by the Heaviside projection. This process is visualized in Figure 3.10. First, a discrete domain is generated by the so called control design variable (γ_c) in Figure 3.10a. Secondly, by using the blurring filter, the discrete domain is transformed to a domain where gray elements are present (Figure 3.10b). Finally, the gray areas are reduced by the Heaviside projection filter as shown in Figure 3.10c, given the final density distribution output.

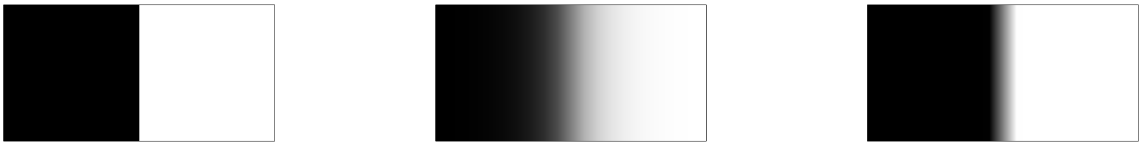

(a) Control design variable (γ_c) distribution.

(b) Filtered design variable (γ_f) distribution, after the blurring filtering step.

(c) Projected design variable (γ) distribution, after the Heaviside projection filtering step.

Figure 3.10: Design variable filtering distribution steps.

3.3.1. Post-processing and verification

The post-processing and verification step is the final step in the TO process, in this step the accuracy of the topology optimized design is verified. As in the density-based design physics and material properties are interpolated between the fluid and solid it is difficult to match the TO model with the verification model. The first step is to do the post-processing, in this step the generated design with gray areas must be transformed to a discrete design. This is normally done by setting a threshold value for the density design variable. All values below the threshold are part of the solid domain, while values above the threshold are fluid. After determining the distinct solid and fluid domains, the geometry is used in a verification model where a normal CFD analysis is performed. In this final analysis the geometry is meshed by using a body fitted mesh.

3.4. Weaknesses in the topology optimization of turbulent flow cooling systems

When performing density-based turbulent flow Topology Optimization several problems may occur. Accurately solving the flow in the near wall region is one of the most important requirements for accurately solving turbulent flow. Normally, in simulations where the geometry is well defined, a body fitted mesh can be created which places a small mesh near the wall and a coarser mesh in the free-stream. This reduces the computation time compared to using a small mesh everywhere, since less mesh elements are used in the simulation. A second way to resolve turbulent flow is by using wall functions. If a fine enough mesh around the wall can not be obtained, the so called wall functions can be used. These wall functions will calculate the turbulent flow variables based on the actual distance away from the wall.

However, when combining these methods with Topology Optimization some problems occur. First of all, in Topology Optimization the location of the walls are not defined *a priori*, and thus no body fitted mesh can be generated. Therefore it is usually standard to use a uniform mesh. This results in some problems when combining it with turbulent flow. Since the size of the mesh elements near the wall are required to be extremely fine the full domain should be meshed with these small elements, this is computationally extremely expensive and thus not realizable. A coarser mesh size could be a solution. However, this will filter away a lot of the turbulence and will thus not result in an accurate design. Secondly, the wall function could be an option to reduce the computation time. However, the wall functions as they are implemented normally create discontinuity in the simulation model, which is undesired for the Topology Optimization since the derivatives of the relevant equations are required and these derivatives might become discontinuous.

4

Investigating the weaknesses of the Dilgen method

In this chapter we are going to investigate and discuss the Dilgen method and investigate the weaknesses of this method. Firstly, a test case is introduced in Section 4.1, the geometry in this case is comparable to a case used by Dilgen et al. [2]. In this way we can investigate the Dilgen method in a case for which it is developed. Secondly, in Section 4.2 the results of the test case are presented. Finally, a discussion on the Dilgen method can be found in Section 4.3.

4.1. U-bend channel test case set-up

The Dilgen method [2] as shown in Section 3.2.3 is currently the state of the art method in density based Topology Optimization when the $k-\omega$ model is used, therefore this model is investigated. The performance of the Dilgen model is tested on a geometry which is similar to the geometry used by Dilgen, namely a bent channel geometry. Secondly, turbulence must occur within this geometry for the chosen Reynolds numbers (of magnitude 10^4 or higher). Finally, this geometry must be similar to an optimized heatsink design which probably will consist of multiple bent channels. Therefore a U-bend channel as shown in Figure 4.1 is used for this test case. In this test case the boundary conditions and settings are similar to those in [2], however some settings might deviate because they are either unknown or computationally not feasible.

The final goal is to perform an optimization of a turbulent flow. An important aspect of the density-based Topology Optimization approach is that the physics in the different domains are dependent on the density variable. Since we first want to investigate the performance regarding the accuracy of the physics, we fix the density values on a design for which we can also calculate more accurate solutions on a body fitted mesh. In this case we can investigate if all physics are handled correctly in the different regions. The solid parts thus have a density value of 0 and the fluid domain has a density value of 1 as shown in Figure 4.1. This density variable is the input control variable γ_c as introduced in Section 3.3, the blurring filter and Heaviside projection slope are applied on this control variable. This results in a small gray area between the fluid and solid. Since it is desired to limit the gray area we chose the blurring filter radius R to be equal to the size of one element.

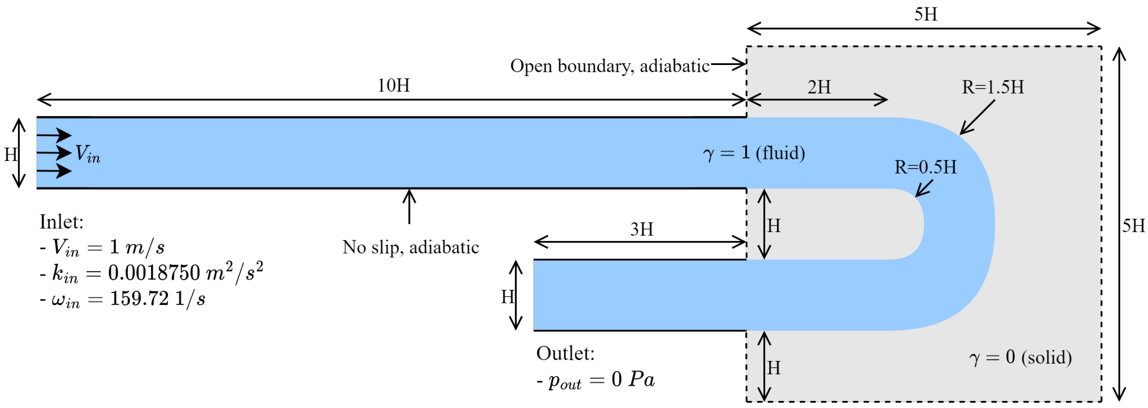

Figure 4.1: U-Bend geometry and boundary conditions overview

For the test case the materials are chosen according to the requirements given in Section 2.1. This means the fluid material has the properties of water and the solid material is aluminum. The specific material properties are specified in Table 4.1.

Table 4.1: Material properties

Material	Property	Symbol	Value	Unit
Fluid (water)	Density	ρ_f	1000	kg/m^3
	Thermal conductivity	k_f	0.6	W/(m K)
	Thermal capacity	c_{pf}	4100	J/(kg K)
	Dynamic viscosity	μ	0.001	Pa s
Solid (aluminum)	Density	ρ_s	2700	kg/m^3
	Thermal conductivity	k_s	237	W/(m K)
	Thermal capacity	c_{ps}	900	J/(kg K)

In Table 4.2 the parameters copied from Dilgen's work are shown. First, this regards the Reynolds number, which is $Re_H = 10^4$. Secondly, Dilgen proposed that a Darcy number between $10^{-5} - 10^{-6}$ should be sufficient to represent the porous material to be solid, we chose $Da = 10^{-6}$ for this case. The penalization factors for the interpolation functions are copied as well, since Dilgen et al. used a sharper interpolation transition for ω the penalizations are separated. Finally, the Heaviside projection parameters are adopted, where the projection slope $\beta = 6$ and the projection point $\eta = 0.5$ are defined.

Table 4.2: Parameters copied from the work of Dilgen et al.

Parameter	Symbol	Value	Unit
Reynolds number	Re_H	10^4	-
Darcy number	Da	10^{-6}	-
Darcy curvature penalization	q_{Da}	0.1	-
Darcy curvature penalty for k	q_k	0.1	-
Darcy curvature penalty for ω	q_ω	10^{-4}	-
Projection slope	β	6	-
Projection point	η	0.5	-

Finally, a characteristic length of $H = 0.01\ m$ is used with which the final properties can be determined. First, the inlet velocity is derived from the given parameters and the Reynolds numbers as:

$$V_{in} = \frac{\mu Re_H}{H\rho_f}. \tag{4.1}$$

The turbulence at the inlet is also defined in terms of the inlet turbulent kinetic energy k_{in} and inlet specific dissipation rate ω_{in}. These are respectively defined as:

$$k_{in} = \frac{3}{2}\left(V_{in}I_T\right)^2, \tag{4.2}$$

$$\omega_{in} = \frac{k^{1/2}}{\left(\beta_0^*\right)^{1/4} L_T}, \tag{4.3}$$

where I_T is a turbulent intensity with a value of 0.05, β_0^* a turbulence model parameter with a value of $\frac{9}{100}$ and L_T a turbulence length scale based on the geometry with a given value of 7×10^{-4}. Finally the maximum impermeability is determined by,

$$\overline{\alpha} = \frac{\nu}{DaH^2}. \tag{4.4}$$

Meshing

As explained in Section 3.2.2, the fundamental difference between the 'Low Re' and 'High Re' models is that the 'Low Re' models solves the fluid behavior up to the wall by linear interpolation. In the 'High Re' models empirical derived wall functions are used to determine the flow in the near wall region. Therefore both models require a different mesh size in the near wall region. For the 'Low Re' turbulence models it is required that the first mesh cell is placed in the viscous sublayer which is roughly below an y^+ of 11.25. Since the Dilgen method is mainly based on the 'Low Re' $k - \omega$

turbulence model its accuracy is compared for different mesh sizes and we hypothesize that for mesh sizes larger than $y^+ = 11.25$ the Dilgen method will become inaccurate. The actual y^+ value is directly related to the normal distance of the wall (y), which is shown in Equation 3.15. Several uniform mesh sizes are used according to the y^+ value of the first cell center based on the inlet. It is decided to have two cases in the viscous sublayer and two cases in the Log-law regime, therefore mesh sizes are used according to the following y^+ values of 5, 10, 50 and 100. An y^+ value of 1 is most desired, unfortunately this is not computationally feasible using the available computing power at the time and therefore could not be used. The used mesh sizes are presented in Table 4.3. Since we decided to use a filter radius of one element the filter radius is equal to the used mesh size.

Table 4.3: Used mesh size in the U-bend problem.

Parameter	**Symbol**	**Value**	**Unit**
Mesh size used for $y^+ = 5$	h_5	8.4667×10^{-5}	m
Mesh size used for $y^+ = 10$	h_{10}	1.6933×10^{-4}	m
Mesh size used for $y^+ = 50$	h_{50}	8.4667×10^{-4}	m
Mesh size used for $y^+ = 100$	h_{100}	1.6933×10^{-3}	m

The meshing is realized by using quadrilateral elements with a maximum allowed mesh size equal to the corresponding wall normal distance for each y^+ value. This ensures that the first mesh cell is placed in the correct region (either the viscous sublayer or the Low-law region). The meshing for the different y^+ cases are shown in Fig. 4.3.

The results of the density simulations are compared with reference simulations. For this reference simulation no density design variable (γ) is used and the interface between the solid and fluid is modeled as a solid no-slip wall. The most accurate results are found when the mesh sizes at the wall (solid/fluid interface) are sufficiently small. To achieve this a body fitted mesh (mesh refinements with boundary layer elements near the wall) is generated where the mesh size decrease in the direction of the fluid-solid interface (Fig. 4.3b). This reference model is referred to as the 'reference best case'. However, beside the simulation on the reference best case, reference simulations are performed on the $y^+ = 5, 10, 50$ and 100 meshes. In these simulations a constant mesh size fixed to the solid/fluid interface is thus used, but contrarily to the density-based simulations a no-slip condition is applied at the solid/fluid interface and no flow is present in the solid domain. These reference simulations are performed to evaluate the errors due to the density-based model (density-based error) while removing errors due to insufficient mesh refinement (mesh error). The difference between the density-based and mesh error are graphically shown in Figure 4.2. The reference models with a specific mesh size are named 'reference h_x' where x is used to compute the mesh size as:

$$h_x = \frac{x y^+ \mu}{u_\tau \rho_f} \tag{4.5}$$

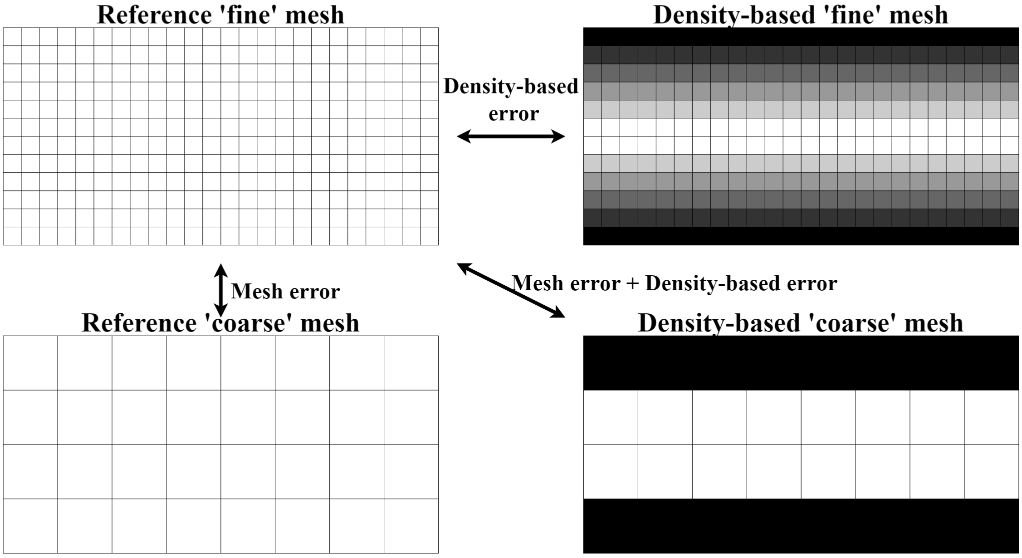

Figure 4.2: Mesh error versus density-based error.

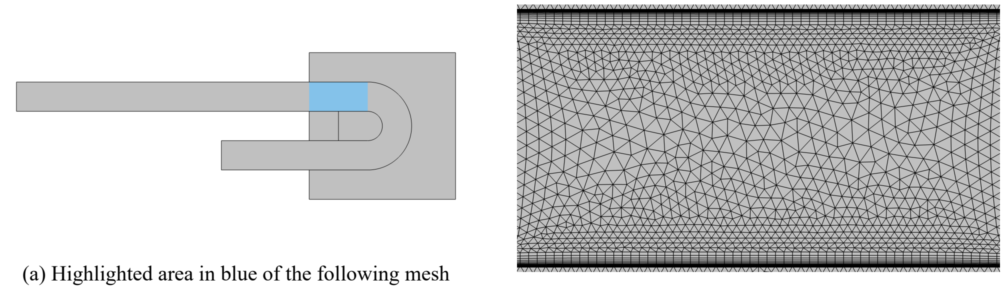

(a) Highlighted area in blue of the following mesh closeups.

(b) Body fitted mesh for the reference simulation.

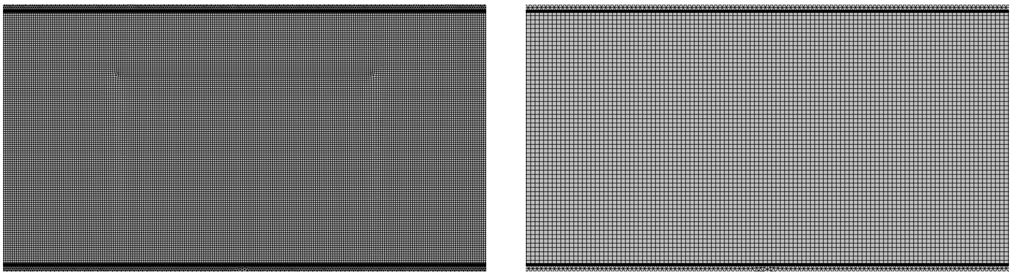

(c) Mesh size h_5.

(d) Mesh size h_{10}.

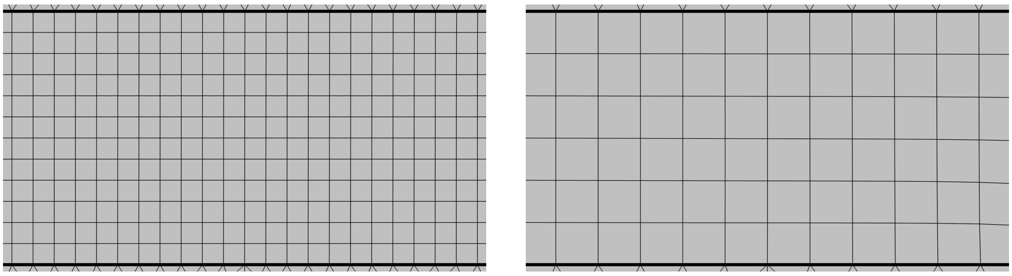

(e) Mesh size h_{50}.

(f) Mesh size h_{100}.

Figure 4.3: Mesh closeups for the different h_x models, where the thicker black line indicates the location of the wall.

4.2. Results of the Dilgen density-based simulation

The behavior of different flow properties are analyzed in the upper channel and in the lower channel. It is expected that in the upper channel only the inlet turbulence is present and no new turbulence is generated since it is a straight channel. Therefore, in the upper channel the influence of the density-based walls on the fluid can be better examined. On the contrary, in the lower channel the turbulence should increase due to the bent channel, therefore the lower channel is also examined to investigate the more turbulent flow. It is desired that the behavior at the wall as well as in the free-stream can be evaluated, therefore two cut lines are introduced. The exact locations of the cut lines are shown in Figure 4.4, where the red and green cut lines are the upper and lower channel respectively. The flow properties which are discussed are the velocity (U), turbulent kinetic energy (k) and specific dissipation rate (ω).

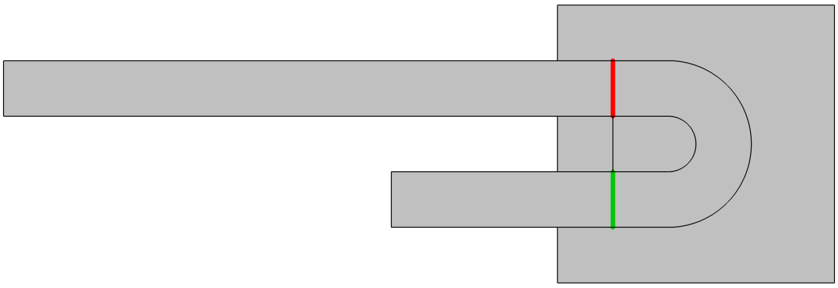

Figure 4.4: The location of the cut lines, where the x location is at $x = H$ from where the fluid enters the domain. Cut line upper channel indicated in red and cut line lower channel indicated in green.

These properties are analyzed visually and by determining the error on the different flow properties. Since different mesh sizes are used in the simulations and the datasets vary in size, it is desired that the error is not affected by the dataset size. This the case with the Relative Root Mean Square Error (RRMSE) and is therefore a suitable error to use. The RRMSE can be calculated by ([38]),

$$RRMSE = \sqrt{\frac{\frac{1}{n}\sum_{i=1}^{n}(y_i - \hat{y}_i)^2}{\sum_{i=1}^{n}(\hat{y}_i)^2}} \cdot 100, \tag{4.6}$$

where y_i is the predicted value and $\hat{y}_i$ is the actual value of a variable. In this case the reference simulation corresponds to the actual value and the density-based models correspond to the predicted value. These RRMSE values are used as a benchmark, so that the improved methods (see Chapter 5) can be evaluated and compared to the Dilgen method.

Density distribution and penalties

The different mesh sizes of h_5, h_{10}, h_{50} and h_{100} influence the behavior of the density distribution throughout the channel. The filtering steps in the model are the same as presented in Section 3.3. The blurring filter radius is equal to the used mesh size. This means that the higher mesh models thus have a larger length over which the density variable converge from maximum $\overline{\gamma} = 1$ to its minimum of $\underline{\gamma} = 0$. The distribution of the density variable in the upper channel on the cut line is shown in Figure 4.5a. The cut line is slightly extended so that the distribution is also shown in the solid domain. In this figure it is shown that the lower y^+ models have a shorter transition length, where design variable γ transitions from 1 to 0. For the larger y^+ values it takes longer to approach $\gamma = 1$, although it looks like it reaches fully fluid this is not the case. In Figure 4.5b $log(1-\gamma)$ is plotted against the vertical distance and this graph shows that there is still some deviation between the results with low and high y^+ mesh resolution, even in the middle of the channel where the density variable should be 1. This behavior also influences the penalties as shown in Figure 4.5c where the impermeability is plotted over the maximum impermeability. The ratio between the impermeability and maximum impermeability should be as low as possible in the fluid domain, in this case the fluid is influenced the least by the penalization terms. It can be seen that the ratios for the models h_{50} and h_{100} are multiple orders higher in the $\gamma = 1$ region compared to the h_5 and h_{10} models. Therefore the penalties are too high in the middle of the channel for the higher mesh size models, causing the fluid to be penalized in a domain where the material properties should be identical to those of a fluid, which is an undesired result.

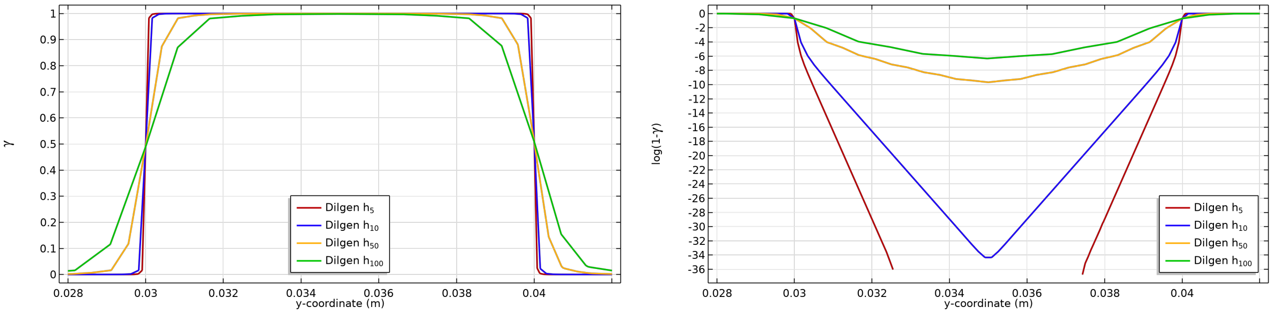

(a) Density variable distribution in the upper channel.

(b) Log(1-γ) distribution in the upper channel.

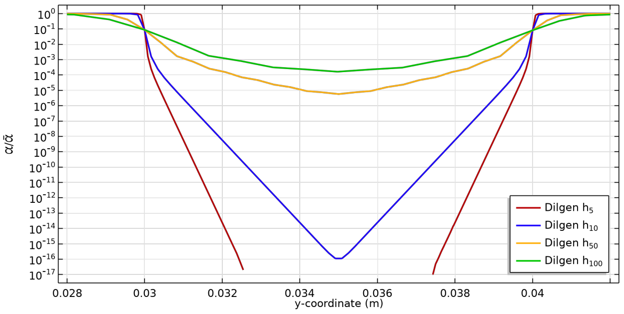

(c) Impermeability normalized by the maximum impermeability in the upper channel.

Figure 4.5: Dilgen density and penalty distributions on a slightly extended cut line in the upper channel.

Velocity (U)

Secondly the velocity is analyzed in the channel. The results of the velocity magnitude for the reference best case as well as the different y^+ mesh sizes in the full domain are shown in Figure 4.6. This gives an overview of the flow in the channel and also the effect of different mesh sizes. It can be seen that the h_5 and h_{10} models show similar behavior as the reference best case model. The largest mesh size (h_{100}) is less accurate, which can be explained by the large transition of the density variable from solid to fluid and the consequent large flow penalization in the fluid domain which is undesired. The h_{50} model shows intermediate results between the lowest and highest mesh sizes. The speed is increased in the corner when compared to the highest mesh size model, however, it does not have the high peak velocities in the inner side of the corner which the lowest mesh size models have.

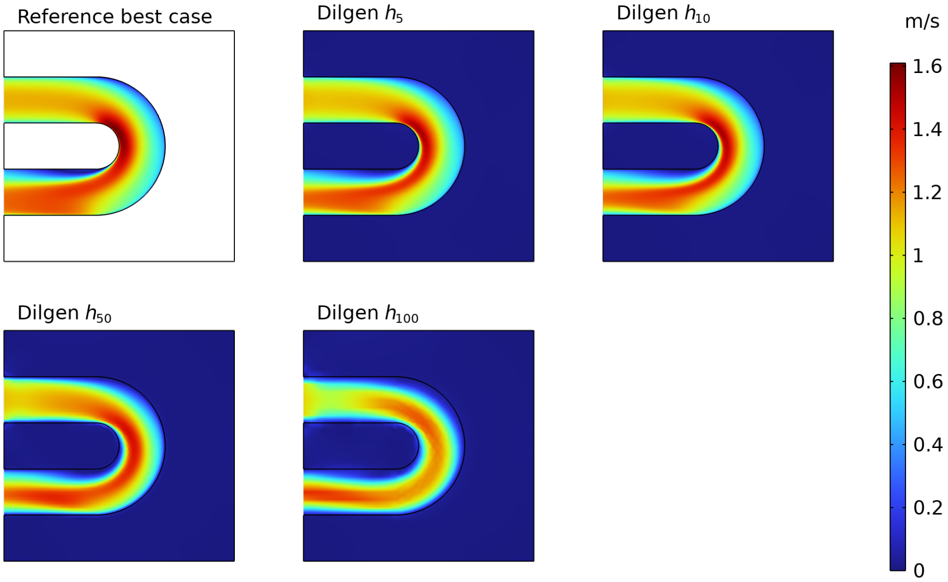

Figure 4.6: Velocity plots reference best case vs. Dilgen for all h_x models.

The difference between the models can be better visualized when looking at the cut lines in the upper channel as shown in Figure 4.7a. This shows directly the inaccuracy of the h_{100} model when compared to the reference best case model. This can be explained by the fact that the mesh is too coarse for an accurate result, and due to the influence of the blurring filter and subsequent penalizations on the flow as shown in Figure 4.5c. Due to the large mesh size the density variable γ is converging less fast to 0 and 1, this means that the penalty on the PDE's are more active in regions where this is not desired and thus influences the flow behavior. Decreasing the mesh size h_x results in the velocity profile converging to the reference simulation. This can be partially explained by the fact that flow penalties become negligible in the free stream region when smaller elements are used. The h_5 model shows the best performance regarding the velocity profiles in this case. The h_5 and h_{10} have a lower velocity profile in the middle of the channel compared to the reference best case simulation. This is due to flow leaking through the center or outer wall which decreases overall mass flow through the channel and consequently maximum mass flow in the channel. The flow leakage is possible since a part of the outer wall is modeled as an open boundary as shown in Figure 4.1, here the flow can leave the domain instead of at the outlet. This flow leakage is confirmed by evaluating the total inlet and outlet velocity in the flow normal direction, if these values do not correspond with each other it means that some flow has leaked. The total inlet velocity in the flow normal direction can be evaluated with the following integral,

$$\text{Total inlet flow in the flow normal direction} = U_{T,in} = \int_0^H U_{n,in}\, dy, \tag{4.7}$$

where $U_{n,in}$ is the flow magnitude at the inlet in the normal flow direction in m/s. The same can be done with the velocity at the outlet. A percentage of the leaked flow is determined as follows,

$$\text{Leaked flow \%} = \frac{U_{T,in} - U_{T,out}}{U_{T,in}} \cdot 100 = \frac{\int_0^H U_{n,in}\, dy - \int_0^H U_{n,out}\, dy}{\int_0^H U_{n,in}\, dy} \cdot 100, \tag{4.8}$$

where thus the $U_{T,out}$ is the total flow velocity at the outlet in $\mathrm{m^2/s}$ and $U_{n,out}$ is the flow magnitude at the outlet in the normal flow direction in $\mathrm{m^2/s}$. Table 4.4 shows the total inlet and outlet velocity and the leaked flow percentage. The flow leakage percentage shows that the flow leakage is increasing when the mesh size is increased as well. To minimize the amount of flow leakage the flow has to be stopped by the porous material.

Table 4.4: Leaked flow overview for the Dilgen method.

h_x	$U_{T,in}$	$U_{T,out}$	**Leaked flow**
h_5	0.0099881 m^2/s	0.0093316 m^2/s	6.57 %
h_{10}	0.0099881 m^2/s	0.0092109 m^2/s	7.78 %
h_{50}	0.0099881 m^2/s	0.0088068 m^2/s	11.83 %
h_{100}	0.0099881 m^2/s	0.0084659 m^2/s	15.24 %

Furthermore, when looking at the velocities for the Dilgen models near the wall (Fig. 4.7b) it shows that the velocities do not converge to zero, which should be the case as we attempt to impose a no-slip boundary condition at the wall through the Darcy penalization.

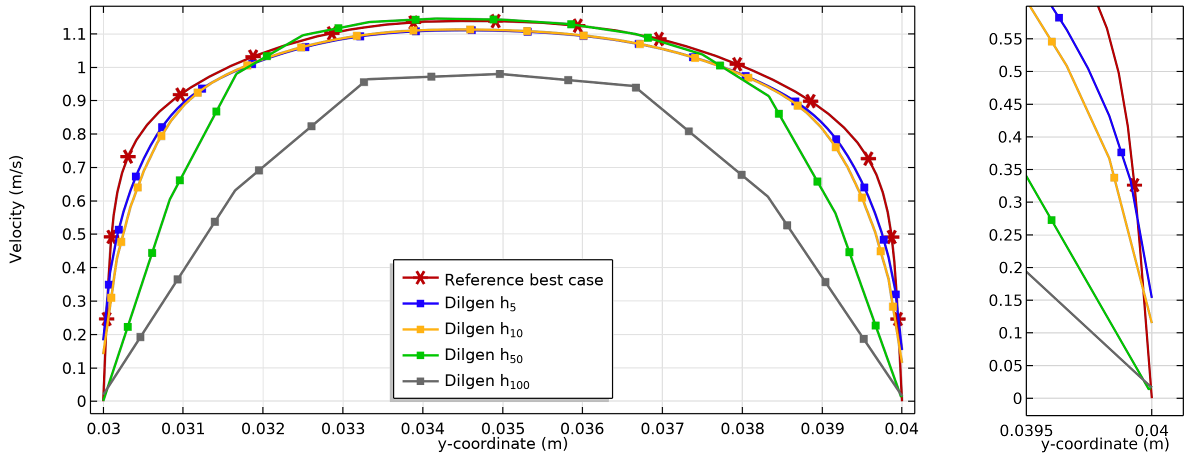

(a) Velocity profiles in the upper channel for the Dilgen method.

(b) Velocity profile at the wall for the Dilgen method.

Figure 4.7: Velocity profile in the upper channel of the Dilgen method for all h_x models.

In Table 4.5 the RRMSE of the density-based velocity profile at the cut lines in the upper and lower channel are given and we have shown that the smaller mesh size results are more accurate as the error are the lowest for the h_5 model. Moreover, the errors show that almost every error decreases when comparing against the reference h_x case instead of the reference best case. As explained in Section 3.2.2 a sufficiently small element size is required to obtain proper results. Therefore when comparing the higher mesh size models (h_{50} and h_{100}) with the reference best case a part of the error could be caused by the coarse mesh size. This is indeed confirmed as the errors are reduced when the results are compared to the reference h_x case. However, the errors h_{50} and especially h_{100} are still too large with values of 13.08% and 31.03% in the upper channel respectively. The h_5 model shows a negligible difference between the reference best case and reference h_x case errors, this means that the mesh size is sufficient enough and that major part of the error is caused by the density-based error. In the lower channel the turbulence is increased due to the bent channel, the errors overall are increased as well in the lower channel. Thus it can be concluded that the Dilgen model has more trouble with finding the correct solution if more turbulence is present in the channel. The velocity for the Dilgen method in the lower channel can be found in Appendix C.1.

Table 4.5: RRMSE of the velocity on the cut lines in the upper and lower channel with the Dilgen method.

Location	**w.r.t.**	h_5	h_{10}	h_{50}	h_{100}
Upper channel	Reference best case	4.62 %	6.33 %	18.09 %	34.11 %
	Reference h_x case	4.48 %	4.77 %	13.08 %	31.03 %
Lower channel	Reference best case	11.13 %	14.34 %	24.71 %	31.67 %
	Reference h_x case	10.12 %	9.50 %	30.53 %	33.41 %

Specific dissipation rate (ω)

The specific dissipation rate is an important flow property to investigate. Especially in the $k-\omega$ model the specific dissipation rate is of importance since it determines the turbulent dynamic viscosity (Equation 3.11) together with the turbulent kinetic energy. In Figure 4.8 the specific dissipation rate is shown versus the vertical distance y in the upper channel. In contrast to the velocity, the specific dissipation rate does not go to zero at the wall but should go to infinity. This is also the reason why the penalty on the ω PDE (Equation 3.28) is slightly different than the Darcy penalty (Equation 3.26) and the turbulent kinetic energy penalty (Equation 3.27). The behavior at the wall is shown in Figure 4.8, where the squares at both sides in the figure indicates the boundary condition where ω should be pushed to ω_b, this boundary condition is dependent on the mesh size as can be seen in Equation 3.29 and is proportional to $\frac{h}{2}$ as:

$$\omega_b = \frac{60\nu}{\beta_1 y_1^2} = \frac{60\nu}{\beta_1 \left(\frac{h}{2}\right)^2} \tag{4.9}$$

The attention is immediately drawn to the boundary condition of the reference velocity which is several orders higher than the Dilgen model, this is due to the 'wall elements' which COMSOL uses as explained in Subsection 3.2.2. It is important to note that the wall elements are not present in the density-based simulations since no crisp wall can be generated and thus the wall in the density-based simulation consists out of gray elements. The non density-based $k-\omega$ model thus uses different equations for determining the ω, where Equation 3.9 is used in the main flow and Equation 3.12 is used in the 'wall elements' to simply fix $\omega = \omega_b$ at the wall. However, different equations in different regions or elements is not possible in Topology Optimization. The reason for this is that one set of continuous equations throughout the whole domain is required to calculate continuous sensitivities in Topology Optimization. This is also the main reason why penalties are added to the PDE's because this guarantees the continuous equations in the optimization domain.

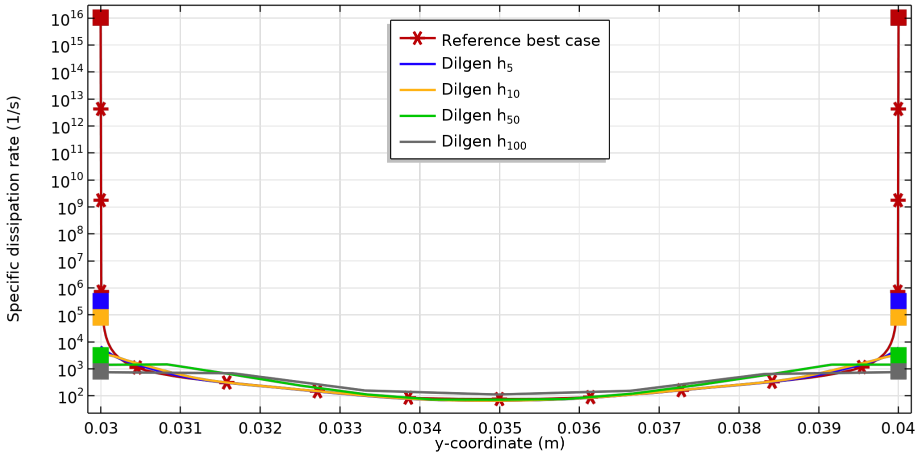

Figure 4.8: Specific dissipation rate in the upper channel reference simulation and density study Dilgen for different mesh sizes $h_5, h_{10}, h_{50}, h_{100}$. The squares at both sides indicate the ω_b target where the specific dissipation rate is pushed to.

To be able to properly inspect the density based results, we generate the plot in Figure 4.9, where we cut off the maximum plotted dissipation at $\omega = 10^6$ such that we do not show the complete ω profile of the reference case. Similar to the velocity profile accuracy, the coarser mesh solutions are less accurate in this case for the specific dissipation rate. The wall boundary value ω_b to which the solutions is pushed is also lower when a larger h_x is used, which is a consequence of its dependence on the element size as shown in Equation 4.9. In the boundary condition the mesh size is in the denominator and thus a higher mesh size results in a lower ω_b target which is an undesired result. The penalties in the h_{50} and h_{100} models also contribute further away from the wall as shown in Figure 4.5c which is undesired. In Figure 4.9b the behavior of ω near the wall is shown. When the mesh size is decreasing the ω_b target is increasing which is desired, however it can also be seen that there is a large mismatch between the ω_b target and the actual value of ω at the wall.

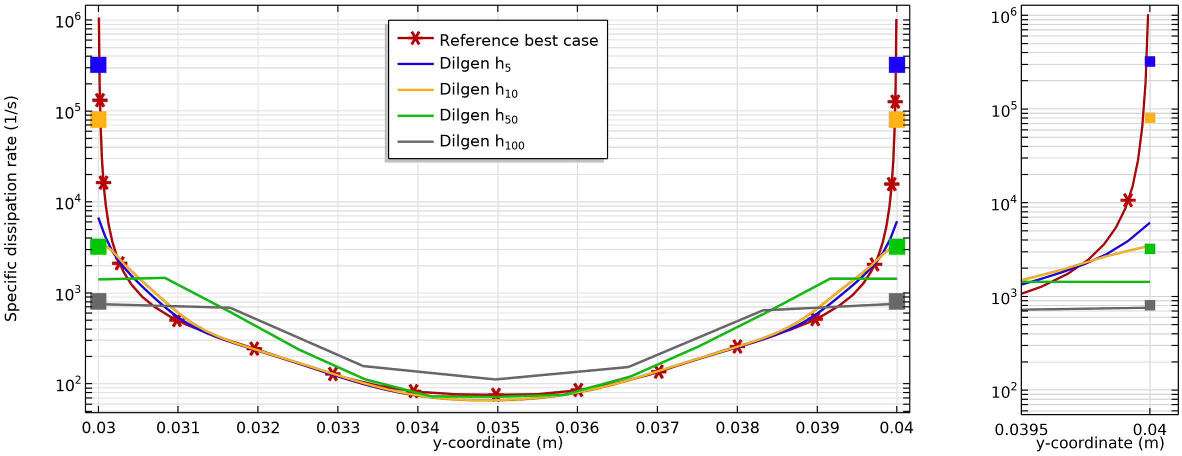

(a) Specific dissipation rate in the upper channel.

(b) Specific dissipation rate at the wall.

Figure 4.9: Specific dissipation rate in the upper channel without wall elements for the Dilgen method. The squares in both figures indicates the wall boundary condition which is implied.

Figure 4.10 shows the specific dissipation rate on an extended cut line in the upper channel, where thus the specific dissipation rate is partly plotted in the solid area. It can be seen that the specific dissipation rate is increasing when moving further into the solid, which is due to the penalization which is not yet at its maximum value at the location of the wall. However, even when reaching the maximum penalization there is still a difference between the specific dissipation boundary condition ω_b and the maximum specific dissipation rate computed by the density-based model in the solid domain. The specific dissipation rates for the Dilgen method in the lower channel can be found in Appendix C.1.

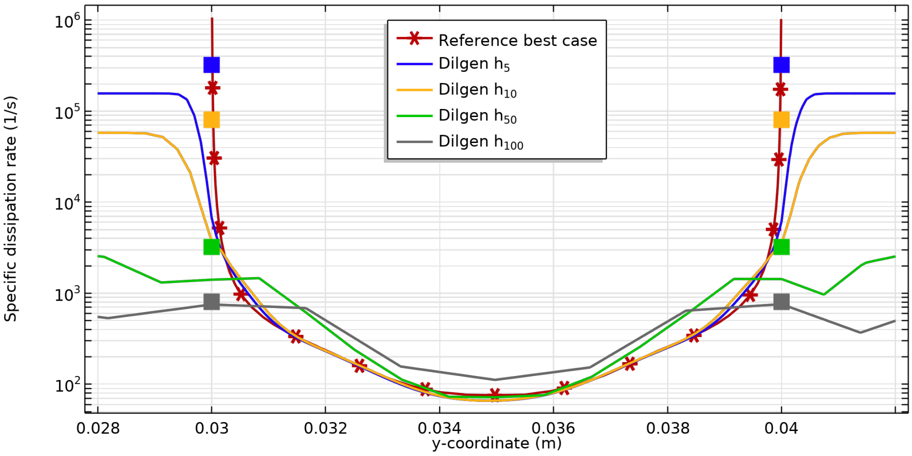

Figure 4.10: Specific dissipation rate at an extended cut line in the upper channel. The squares indicates the ω_b target.

In Table 4.6 the RRMSE of the specific dissipation rate are shown. The errors are tremendous which is probably due to the high specific dissipation rate at the wall in the reference model. This causes a significant difference between the density-based models and the reference models. Secondly, the Dilgen approach is not capable of reaching the ω_b target value which is also adding to the error.

Table 4.6: RRMSE of the specific dissipation rate on the original cut lines in the upper and lower channel with the Dilgen method.

Location	**w.r.t.**	h_5	h_{10}	h_{50}	h_{100}
Upper channel	Reference best case	98.99 %	99.39 %	99.75 %	99.86 %
	Reference h_x case	98.51 %	99.11 %	99.68 %	99.85 %
Lower channel	Reference best case	99.03 %	99.49 %	99.81 %	99.87 %
	Reference h_x case	98.56 %	99.26 %	99.79 %	99.87 %

Turbulent kinetic energy (k)

The turbulent kinetic energy is the final flow property which is analyzed on the cut line in the upper channel, as shown in Figure 4.11. The h_{50} and h_{100} models can not reach the accuracy and performance of the reference model. The low h_5 and h_{10} models react the same as before where in the middle of the channel the models match the reference model. However, near the wall the behavior of the Dilgen models is different from the reference model where the turbulent kinetic energy strongly overshoots the reference turbulent kinetic energy. Similar to the velocity the turbulent kinetic energy should also approach zero at the wall which is not the case in the Dilgen simulations for the low h_x models. The specific dissipation rate in the fluid and the penalty on k should reduce the turbulent kinetic energy. However, the specific dissipation rate is several orders lower than desired at the wall which thus results in a higher turbulent kinetic energy in this region. The turbulent kinetic energy for the Dilgen method in the lower channel can be found in Appendix C.1.

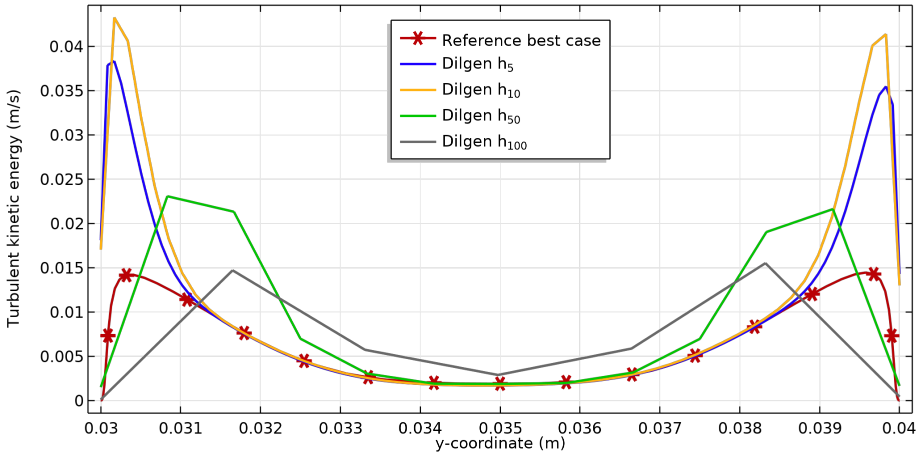

Figure 4.11: Turbulent kinetic energy at the upper channel of the reference best case and Dilgen method.

In Table 4.7 the RRMSE errors in the upper and lower channel are shown for the turbulent kinetic energy k. Especially the errors in the upper channel for the lower mesh size models h_5 and h_{10} with respect to the reference model are quite large. This is due to the significant peak in the near wall region. The h_{10} mesh model in the upper channel with respect to the reference h_{10} shows a relatively low error compared to the other errors. This can be explained by the fact of the difference between the density error and the mesh error as shown in Figure 4.2. The large error of the h_{10} case is this mainly caused by the fact that the mesh in the reference best case is too refined and therefore the h_{10} with respect to the reference best case can never approach the same accuracy as the reference best case.

Table 4.7: RRMSE of the turbulent kinetic energy on the cut lines in the upper and lower channel with the Dilgen method.

Location	**w.r.t.**	h_5	h_{10}	h_{50}	h_{100}
Upper channel	Reference best case	91.92 %	111.65 %	73.49 %	66.14 %
	Reference h_x case	95.07 %	18.82 %	52.51 %	49.57 %
Lower channel	Reference best case	43.89 %	67.11 %	88.67 %	60.72 %
	Reference h_x case	36.40 %	22.32 %	82.53 %	94.36 %

Error analysis

The RRMSE values for each simulation are presented in Table 4.8. In the errors with respect to the reference best case model it can be seen that the best performing model is the h_5 model which has the lowest error for all properties except the specific dissipation rate. However, when the errors are determined with respect to the reference h_x models the h_{10} model seems to be the best solution. It is noticeable that the errors for the turbulent kinetic energy and the specific dissipation rate are extremely high, even for the low mesh size models whereas the velocity errors are acceptable. For the specific dissipation rate this can be explained by the fact that the wall boundary condition in the COMSOL reference simulation is several orders higher than the ω_b target in the density simulations. Secondly, for the turbulent kinetic energy error no logical trend can be detected. A full overview of the full domain RRMSE can be found in Appendix D.

Table 4.8: RRMSE on the full domain of the Dilgen method with respect to reference best case and reference h_x case. Where U is the velocity, k is the turbulent kinetic energy, ω is the specific dissipation rate.

w.r.t.	h_x	**RRMSE** U	**RRMSE** k	**RRMSE** ω
reference best case	h_5	10.39 %	48.22 %	99.24 %
	h_{10}	13.26 %	75.91 %	98.78 %
	h_{50}	26.51 %	103.98 %	89.83 %
	h_{100}	34.26 %	62.41 %	89.38 %
reference h_x case	h_5	9.62 %	43.57 %	99.31 %
	h_{10}	8.63 %	30.88 %	98.57 %
	h_{50}	23.55 %	80.91 %	92.68 %
	h_{100}	30.00 %	92.42 %	99.12 %

4.3. Discussion on the Dilgen method

The results shown in this section illustrate that there remains much room for improvement in the Dilgen method. Especially the errors in specific dissipation rate can be significantly improved, but it has to be noted that a large part of the errors for dissipation rate are caused by the dissipation rate at the boundary which is fixed at extremely high values in the reference simulations and are not attainable by the density based simulations. Nevertheless, the value for the specific dissipation rate at the wall can be significantly increased and improved as illustrated in Figure 4.10. The main issue of the Dilgen method is thus that the targets which are imposed are not met at the wall (interface between solid and fluid). It is desired to adjust the specific dissipation rate at the wall which will in the end also affect the turbulent kinetic energy and finally the velocity at the wall. We expect the significant errors for h_{50} and h_{100} cannot be improved satisfactory as the mesh size is too large for the $k - \omega$ model as explained in Section 3.2.2. Consequently, these mesh sizes will not be used and investigated in subsequent chapters. For these coarser mesh sizes, wall function models could improve the accuracy of the solution. However, these type of models require empirically derived equations in the elements near the wall. This results in different sets of equations for the elements throughout the optimization domain, which will introduce discontinuities in the optimization domain. These discontinuities are unwanted in the gradient based TO process since the derivatives in the domain are used to obtain the sensitivities to find an optimal solution.

5

Improvements on the Dilgen method for the topology optimization of turbulent-flows

In this chapter several improvements on the Dilgen method in the field of turbulent topology optimization are presented. In Table 5.1 an overview of the discussed methods can be found along with the section number where the methods are explained. Every method is introduced in each section followed by the results and a conclusion. Finally, in Section 5.4 conclusions regarding the improved methods are presented along with a discussion on which is the best improvement.

Table 5.1: Overview of the improved methods.

Method	**Section**
Dilation method	Section 5.1
Mesh dependent impermeability method	Section 5.2
Mesh dependent impermeability with dilation method	Section 5.3
Dilgen wall distance approach	Appendix E.1
Forchheimer method	Appendix E.2
Forchheimer with dilation method	Appendix E.3
Mesh dependent impermeability with dilation method including heat transfer	Appendix B.2

5.1. Dilation method

In Chapter 4 the Dilgen method is analyzed on the bent channel geometry so that the weaknesses could be discovered. One of the weaknesses of the Dilgen method is that the imposed boundary conditions at the solid/fluid interface are not met. It can be seen in Figure 4.9 that the specific dissipation rate value at the wall is lower than the ω_b target. The underestimation of the specific dissipation rate at the wall influences the turbulent kinetic energy at the wall as well. Due to the lack of specific dissipation rate the turbulent kinetic energy is not dissipated as it should. This can be seen in Figure 4.11 where the turbulent kinetic energy of the Dilgen h_5 and h_{10} models overshoots the reference best case model. As shown in Figure 4.10 the specific dissipation rate is still increasing in the solid domain. This shows that the Dilgen method is capable of reaching higher values for the specific dissipation rate, which have a better approximation of the ω_b target value. However, this approximation is at the wrong location. The maximum specific dissipation rate should be at the fluid/solid interface instead of inside the solid domain. The specific dissipation rate is controlled by the ω penalization (Equation 3.28) which is dependent on the density variable. When the density variable approaches a solid value of $\gamma = 0$, the ω penalty becomes more active and pushes the specific dissipation rate to the ω_b target. To achieve the maximum specific dissipation rate at the fluid/solid interface, the ω penalty should already be fully active in the last 'fluid' element before the fluid/solid interface instead of in the first 'solid' element after the fluid/solid interface. Therefore, we try to shift the penalization into the fluid domain by adapting the impermeability in the ω penalization (α_ω). The impermeability of the ω penalization is dependent on the design variable. Since we only desire to adjust the ω penalization we split the blurred design variable (γ_f). This results in the projected design variable (γ) used for the RANS penalization (Equation 3.26) and k penalization (Equation 3.27) and an ω projected design variable (γ_ω) used for the ω penalization. The process of shifting the ω penalization $\alpha_\omega(\gamma_\omega)$ by shifting the design variable γ_ω into the fluid domain is shown in Figure 5.1.

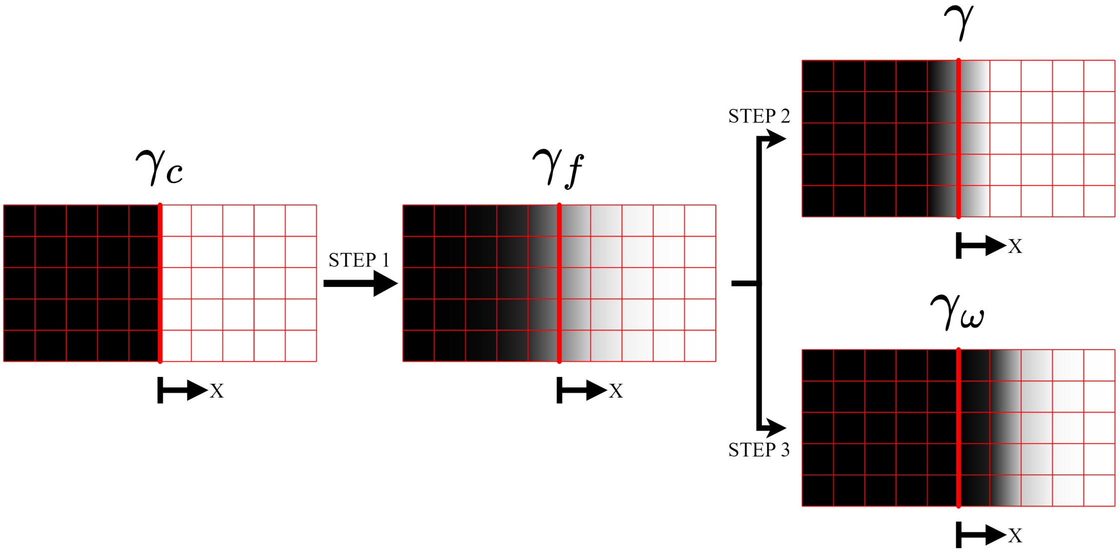

Figure 5.1: Dilation process. Step 1: blurring filter. Step 2: Heaviside projection filter for γ. Step 3: Heaviside projection filter for γ_ω. The mesh grid is indicated in red, the location of the wall is indicated by the thicker red line. For demonstration purposes the dilation is two elements instead of one element in this figure.

To obtain the shifted design variable γ_ω we can use the Heaviside projection filter (Equation 3.31). The Heaviside projection filter is initially used to obtain a more discrete design as explained in Section 3.3. However, this Heaviside projection filter requires a threshold value where values below the threshold are pushed to either 0 or 1. Therefore, this filter can be perfectly used for shifting the ω projected design variable by adjusting the Heaviside threshold value for ω (η_ω). The Heaviside projection filter adjusted for the ω design variable is given by the following equation,

$$\gamma_\omega = \frac{\tanh(\beta_\omega(\gamma_f - \eta_\omega)) + \tanh(\beta_\omega \eta_\omega)}{\tanh(\beta_\omega(1-\eta_\omega)) + \tanh(\beta_\omega \eta_\omega)}, \tag{5.1}$$

where γ_ω is the ω design variable used to calculate the penalization in the ω equations ($\alpha_\omega(\gamma_\omega)$), β_ω the projection slope for the ω design variable and η_ω is the threshold for the ω penalization dependent on the desired dilation.

As it is desired that the ω penalization is active in the last 'fluid' element at the solid/fluid interface, we aim to push density variable γ_ω exactly one element into the fluid domain. In a paper published by Clausen et al [39] a method is presented that can be used to determine the correct threshold value for shifting the solid/fluid boundary exactly one element into the fluid domain. In this paper, threshold η_ω is determined as a function of the used blurring filter radius and the amount of elements the design has to shift. First of all, it is assumed that a perfect discrete function is the input of the design, this corresponds to the control design variable (γ_c) in Figure 5.1. Such a function can be described using a discrete Heaviside step function which is the discrete version of the continuous Heaviside function in Equation 3.31 and Equation 5.1,

$$\gamma_c(x) = \begin{cases} 0 & \text{x<0,} \\ 1 & \text{x≥0.} \end{cases} \tag{5.2}$$

Secondly, the control design variable is filtered by the blurring filter (Equation 3.30 as shown in Step 1 in Figure 5.1), obtaining the filtered design variable (γ_f) . Following [39], the filtered design variable field can be calculated from the control design variable and the blurring filter by,

$$\begin{aligned} \gamma_f(x) &= \gamma_c(x) + \frac{e^{x\frac{2\sqrt{3}}{r}}}{2}(1-\gamma_c(x)) - \frac{e^{-x\frac{2\sqrt{3}}{r}}}{2}\gamma_c(x) \\ &= \gamma_c(x) + \frac{e^{\frac{x}{R}}}{2}(1-\gamma_c(x)) - \frac{e^{-\frac{x}{R}}}{2}\gamma_c(x) \end{aligned} \tag{5.3}$$

where $r = 2\sqrt{3}R$ and R is the blurring filter radius. The value of the filtered design variable field γ_f thus depends on distance x. If the solid/fluid interface is at $x = 0$, as is the case in Figure 5.1, and we want to shift exactly one element, then we can determine the threshold η_ω for the value of γ_f at $x = h$, where h is the element size. When the filtered density variable at $x = h$ is known, the Heaviside projection threshold has to be set to this value to shift the projected density variable. In Figure 5.2 a filtered design variable field is shown with the intersection point at distance one element from the solid/fluid interface. Note that in this figure not the actual values are used but this figure aims to clarify the dilation principle.

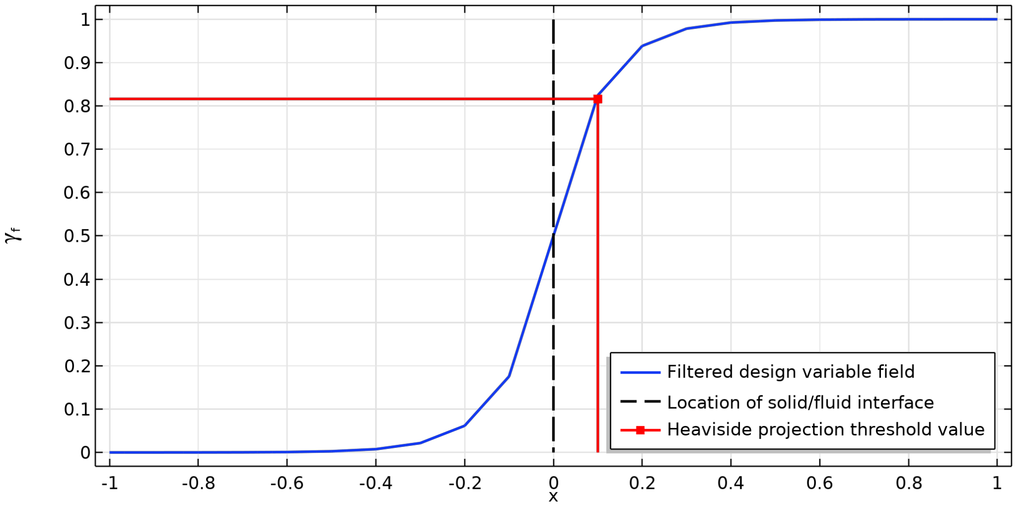

Figure 5.2: Filtered design variable dependent on distance x. The dashed black line indicates a fluid/solid interface in this case at $x = 0$. The red point is shown at $x = h$ and thus the corresponding γ_f value is the Heaviside projection threshold value for the dilation filter. Note that the values in this figure do not correspond to the actual problem but are for demonstration purposes.

All the required information to calculate the Heaviside projection threshold for ω (η_ω) is present. First of all, the blurring filter radius is equal to the used mesh size ($R = h$). Secondly, we want to shift the solid/fluid boundary one element and thus aim to put a threshold at the density $\gamma_f(x)$ at one element shifted to the right ($x = h$). Since both, the blurring filter radius ($R = h$) and the shift distance ($x = h$) are dependent on the mesh size Eq. 5.3 can be reduced to,

$$\gamma_f(x = h) = 1 + \frac{e^1}{2}(1 - 1) - \frac{e^{-1}}{2}1 = 0.82. \tag{5.4}$$

where $\gamma_c(x = h) = 1$ is used. Therefore the dilation is in this case only dependent on the input variable γ_c. As $\gamma_f(x = h) = 0.82$, the projection threshold for ω is defined as $\eta_\omega = 0.82$. As last step the projection slope has to be determined. Since we want to analyze only the effect of the displacement of the ω penalization it is desired that the ω design variable (γ_ω) remains as 'sharp' as possible. Therefore is decided to increase the projection slope for the ω penalization significantly to 80, this ensures that the γ_ω transitions within one element from solid to fluid. Note that this is a high value for the projection slope and such high values often restrict the optimization process. However, since we already know the geometry and do not deal with changing geometries it is possible to use a slope this high.

Parameters used in this case are summed up in Table 5.2.

Table 5.2: Parameters used in the Dilation method.

Parameter	**Symbol**	**Value**	**Unit**
Reynolds number	Re_H	10^4	-
Darcy number	Da	10^{-6}	-
Darcy curvature penalization	q_{Da}	0.1	-
Darcy curvature penalty for k	q_k	0.1	-
Darcy curvature penalty for ω	q_ω	10^{-4}	-
Projection slope	β	6	-
Projection point	η	0.5	-
Projection slope ω	β_ω	80	-
Projection point ω	η_ω	0.82	-

5.1.1. Results on the Dilation method

In this section the velocity profiles, specific dissipation rates and the turbulent kinetic energies are investigated for the Dilation method.

Velocity (U)

The velocity profiles of the Dilation method are shown in Figure 5.3. One of the challenges with the Dilgen method is that simulations were not able to reach the ω_b wall target. By using the Dilation method the simulations are capable of getting closer to the given ω_b target, as shown for the h_5 and h_{10} models respectively in Figure 5.3b and Figure 5.3d. By adapting the penalty for ω, the velocity at the wall is thus also influenced and more capable of reaching the wall targets. Unfortunately this method also has some drawbacks, it causes the penalty to be more active not only directly near the wall but also somewhat further away from the wall in the fluid domain. This results in the strange bends in the upper corners of the velocity profiles for both h_x models (Fig. 5.3a and Fig. 5.3c). Due to this the maximum velocity in the free stream also appears to be lower than the reference best case. The velocity for the Dilation method in the lower channel can be found in Appendix C.2.

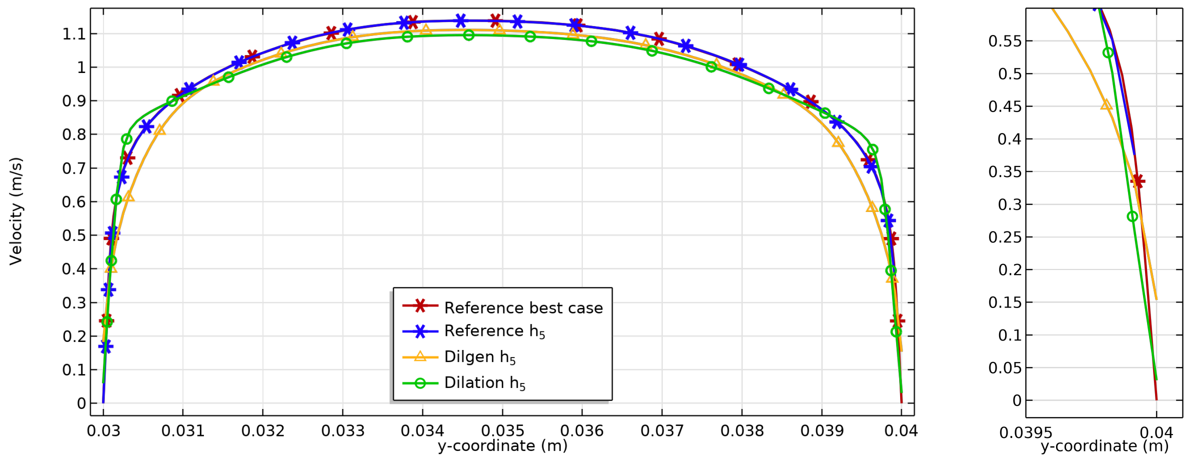

(a) Velocity profile in the upper channel for h_5.

(b) Velocity profile at the fluid/solid interface for h_5.

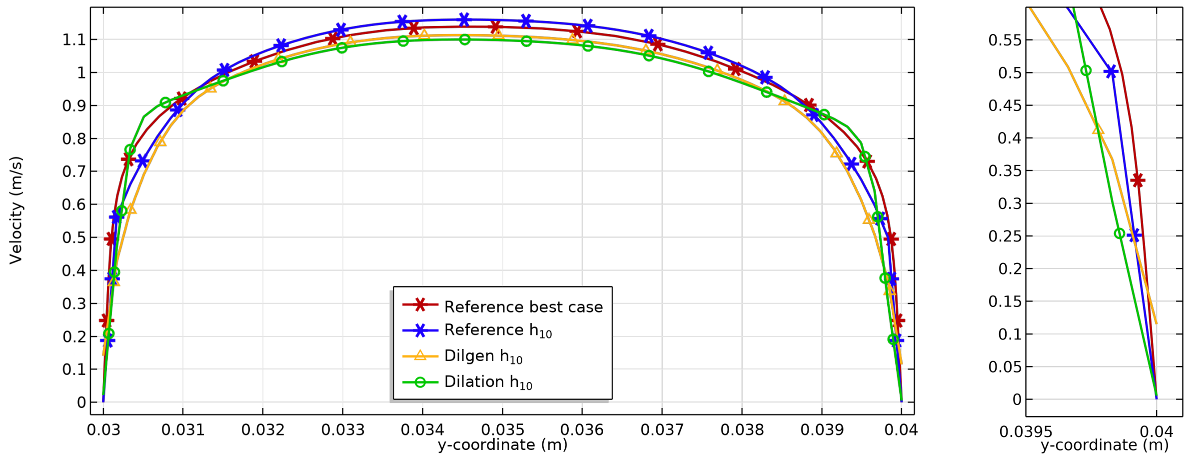

(c) Velocity profile for h_{10}.

(d) Velocity profile at the fluid/solid interface for h_{10}.

Figure 5.3: Velocity profile in the upper channel with the Dilation method.

The flow leakage for the Dilation method is shown in Table 5.3. It shows that the flow leakage is slightly reduced in the Dilation method. Since the velocity at the wall is decreased, less fluid has flowed through the porous material and thus the flow leakage is reduced compared to the Dilgen method.

Table 5.3: Percentages leaked flow for the Dilation method and the Dilgen method.

h_x	**Dilation leaked flow**	**Dilgen leaked flow**
h_5	4.90 %	6.57 %
h_{10}	4.90 %	7.78 %

In Table 5.4 the RRMSE of the velocity in the upper and lower channel are presented. It can be seen that the velocity error in the upper channel is slightly reduced compared to the Dilgen method, except for the h_{10} with respect to the reference h_{10} case. The reduction could be caused by the velocity approaching the boundary target at the wall better than the Dilgen method. The Dilgen method performs better in the free-stream which could be the reason why the mutual difference so small. In the lower channel the Dilgen method errors are increased instead of reduced.

Table 5.4: RRMSE of the velocity on the cut lines in the upper and lower channel with the Dilation method. The RRMSE of the Dilgen method are included as well for comparison.

		Dilation method		**Dilgen method**	
Location	**w.r.t.**	h_5	h_{10}	h_5	h_{10}
Upper channel	Reference best case	3.84 %	5.20 %	4.62 %	6.33 %
	Reference h_x case	3.80 %	5.01 %	4.48 %	4.77 %
Lower channel	Reference best case	14.91 %	22.58 %	11.13 %	14.34 %
	Reference h_x case	14.65 %	21.83 %	10.12 %	9.50 %

Specific dissipation rate (ω)

The specific dissipation rates for the Dilation method are displayed in Figure 5.4. The most important improvement this method shows is that the simulations are better capable of reaching the ω_b wall target. It can be seen that the gap between the ω_b target and the specific dissipation rate at the fluid/solid interface for the Dilation method is much smaller than in the Dilgen method. This is the case for both the h_5 and h_{10} model and is observed even better in the close ups in Figures 5.4b and 5.4d. Although, it looks like the density-based models produce ω_b targets which are higher than the reference h_x models this is not the case. Similar as in Figure 4.9 the wall elements of the reference models are removed which again reach extremely high values. The specific dissipation rate for the Dilation method in the lower channel can be found in Appendix C.2.

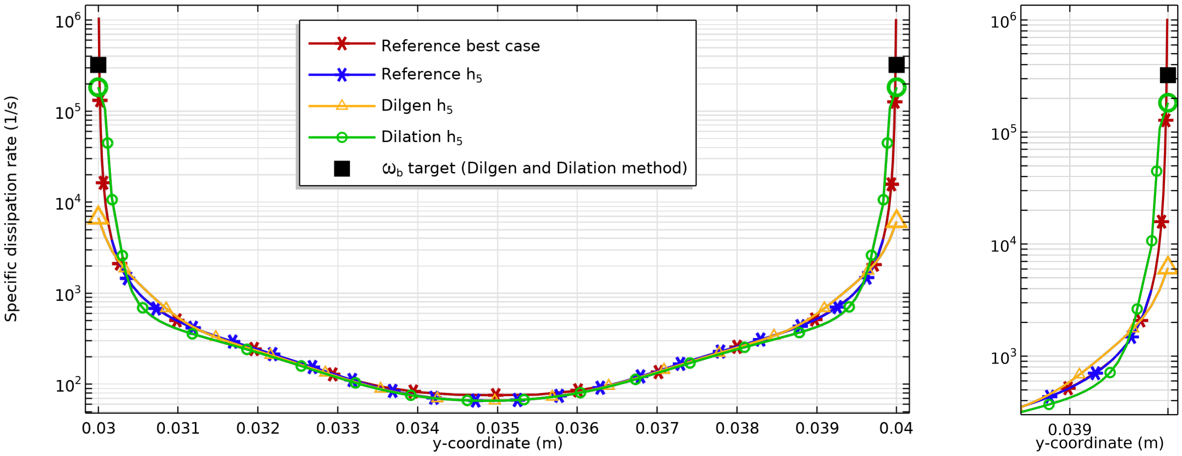

(a) Specific dissipation rate for h_5.

(b) Specific dissipation rate at the fluid/solid interface for h_5

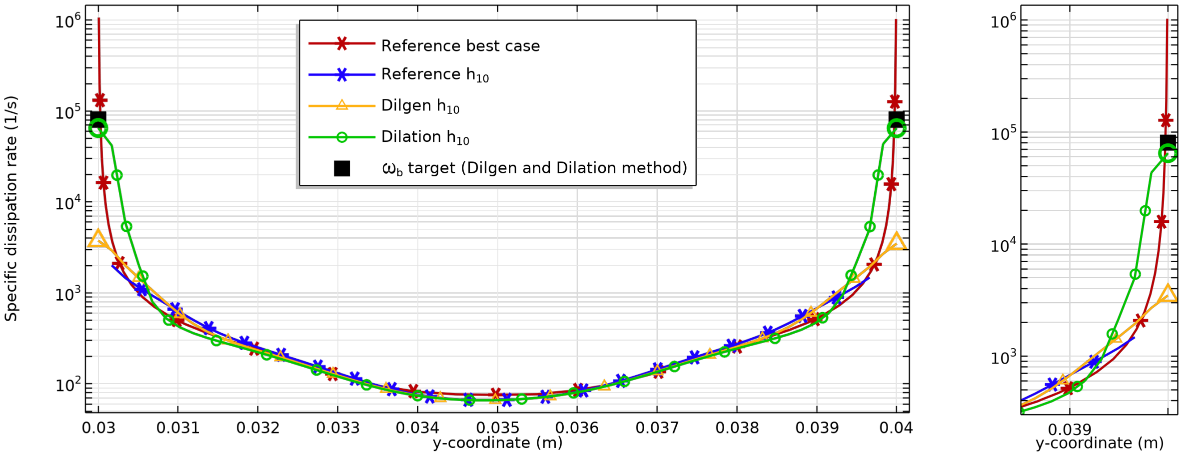

(c) Specific dissipation rate for h_{10}.

(d) Specific dissipation rate at the fluid/solid interface for h_{10}

Figure 5.4: Specific dissipation rate in the upper channel with the Dilation method. The largest mark at the outer sides represents the value at the fluid/solid interface.

The results seems promising since it reaches the ω_b target closely with the Dilation method. However, the Dilation method has some drawbacks as well, Figures 5.4b and 5.4d for the h_5 model and h_{10} model respectively, show that there is a sharp turn close to the fluid/solid interface. Therefore, the specific dissipation rate profile does not completely match with the reference simulations. To find the origin of this problem we look into the ω penalization in Figure 5.5. In this figure the ω penalization for the h_{10} is shown in the upper channel and also slightly into the solid domain. It can be observed that the Dilgen penalization is already decreasing when still in the solid domain and not passed the solid/fluid interface yet, while the penalization in the Dilation method is still on the maximum value until it reaches the fluid/solid interface. It must be noticed that the penalization in the Dilgen method has a less sharp transition, this is due to the smaller projection slope which is $\beta = 6$. However, even if the Dilgen method had the same projection slope of 80 as in the Dilation method, the penalization would still decrease in the solid domain although the decrease would be closer to the solid/fluid interface. It can be seen in Figure 5.5 that the penalization for the Dilation method drops quite heavily in a small distance, this can affect the behavior of the specific dissipation rate. If the penalty changes quite largely within the distance equal the size of an element the strange corners as in Figure 5.4 can occur. So the large projection slope is useful in obtaining the maximum penalty at the fluid/solid interface, but also causes large differences in penalizations over a small distance.

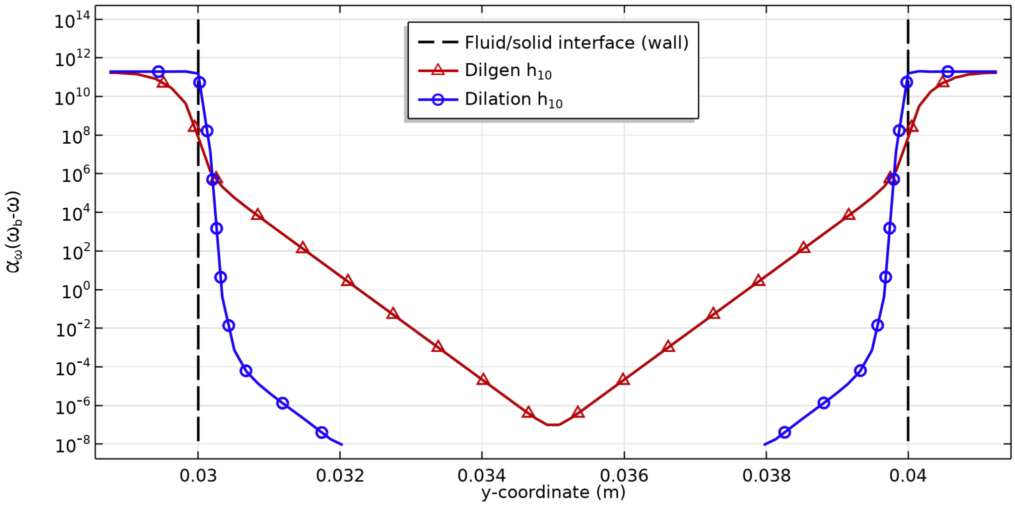

Figure 5.5: ω penalization in the upper channel for the Dilgen method and Dilation method with the h_{10} mesh size.

In Table 5.5 the errors are presented regarding the specific dissipation rate. Still the errors are quite large however they mostly are reduced with almost around 17% for the reference best cases when compared to the Dilgen method. The Dilation model with the h_5 mesh with respect to the reference h_x case is decreased with more than 20%. So with the Dilation method the specific dissipation rate at the wall is approached better, as already could be seen in Figure 5.4.

Table 5.5: RRMSE of the specific dissipation rate on the cut lines in the upper and lower channel with the Dilation method. The RRMSE of the Dilgen method are included as well for comparison.

		Dilation method		**Dilgen method**	
Location	**w.r.t.**	h_5	h_{10}	h_5	h_{10}
Upper channel	Reference best case	81.45 %	92.60 %	98.99 %	99.39 %
	Reference h_x case	77.46 %	90.25 %	98.51 %	99.11 %
Lower channel	Reference best case	81.68 %	92.73 %	99.03 %	99.49 %
	Reference h_x case	77.88 %	90.48 %	98.56 %	99.26 %

Turbulent kinetic energy (k)

The turbulent kinetic energy results in the upper channel can be obtained in Figure 5.6. In the Dilgen method the turbulent kinetic energy had a large overshoot in the region near the fluid/solid interface, as shown in Figure 5.6. The Dilation method shows the opposite for the h_5 model in Figure 5.6a. It is shown that the turbulent kinetic energy is actually lower than both reference simulations. As explained the ω penalization is still on its maximum for a short range beyond the fluid/solid interface resulting in a higher specific dissipation rate than desired. This higher specific dissipation rate also influences the turbulent kinetic energy in a way that it dampens out the turbulent kinetic energy. Therefore the turbulent kinetic energy is lower than the reference simulations in the region near the fluid/solid interface. The turbulent kinetic energy for the Dilation method in the lower channel can be found in Appendix C.2.

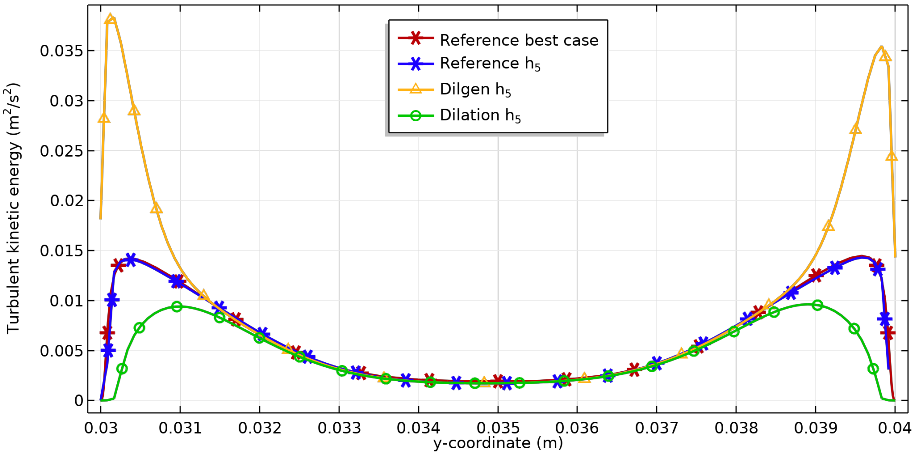

(a) Turbulent kinetic energy for h_5.

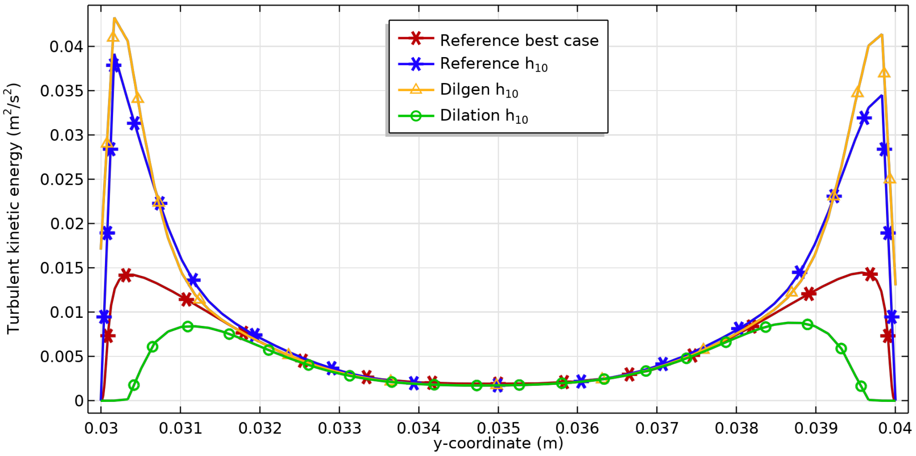

(b) Turbulent kinetic energy for h_{10}.

Figure 5.6: Turbulent kinetic energy in the upper channel with the Dilation method.

The RRMSE of the turbulent kinetic energy remain high as can be seen in Table 5.6, but especially for the h_5 results this method is an improvement on the Dilgen method where the errors in the upper channel are reduced from 91.92% (w.r.t. reference best case) to 42.60%. However, RRMSE of the Dilgen h_{10} model compared to the reference h_{10} case shows a significant lower error. This is due to the fact that the reference h_{10} model also overshoots the reference best case as can be seen in Figure 5.6. Therefore, the results of the Dilgen h_{10} and reference h_{10} model are similar and the error is reduced.

Table 5.6: RRMSE of the turbulent kinetic energy on the cut lines in the upper and lower channel with the Dilation method. The RRMSE of the Dilgen method are included as well for comparison.

		Dilation method		**Dilgen method**	
Location	**w.r.t.**	h_5	h_{10}	h_5	h_{10}
Upper channel	Reference best case	42.60 %	56.98 %	91.92 %	111.65 %
	Reference h_x case	41.35 %	56.12 %	95.07 %	18.82 %
Lower channel	Reference best case	51.90 %	63.61 %	43.89 %	67.11 %
	Reference h_x case	46.04 %	57.82 %	36.40 %	22.32 %

5.1.2. Discussion on the Dilation method

The complete RRMSE table can be found in Table 5.7. The velocity error did not improve by this method which is caused by the leakage through the porous areas. However, the Dilation method shows the desired results in improving the error on the specific dissipation rate. For the h_5 case with respect to the reference best case this means an improvement on the specific dissipation rate error from 99.24% to 84.53%. This error is still quite large which is again caused by the significant difference in specific dissipation rate at the wall. It can be concluded that this dilation method improves on the behavior of the specific dissipation rate and partly in the turbulent kinetic energy. However, for the velocity the errors are increased and thus an improvement needs to be implemented which counters the leakage through the porous areas.

Table 5.7: RRMSE of the full domain of the Dilation method with respect to the reference best case and reference h_x case. The RRMSE of the Dilgen method are included as well for comparison.

		Dilation method			**Dilgen method**		
w.r.t.	h_x	**RRMSE** U	**RRMSE** k	**RRMSE** ω	**RRMSE** U	**RRMSE** k	**RRMSE** ω
reference best case	h_5	14.91 %	47.44 %	84.53 %	10.39 %	48.22 %	99.24 %
	h_{10}	20.95 %	55.40 %	85.73 %	13.26 %	75.91 %	98.78 %
reference h_x case	h_5	14.19 %	43.27 %	85.28 %	9.62 %	43.57 %	99.31 %
	h_{10}	16.99 %	52.78 %	84.34 %	8.63 %	30.88 %	98.57 %

5.2. Mesh dependent impermeability method

In this section a new method is presented in which the impermeability is dependent on the mesh size, therefore this method is named the Mesh dependent impermeability method (MDI method). In the MDI method, which is presented by Theulings [40], the penalizations on the RANS equation (Equation 3.26), the turbulent kinetic energy (Equation 3.27) and the specific dissipation rate (Equation 3.28) is adjusted to using the Reynolds number and parameters in the optimization set-up. Before the impermeability can be determined an initial estimate of the *elemental Reynolds number* is made. The elemental Reynolds number measures the respective relevance of the inertial and viscous forces in a discrete element in the mesh. The elemental Reynolds number is defined as,

$$Re_e = \frac{\rho|\vec{v}^f|h}{\mu}, \tag{5.5}$$

where $\vec{v}^f$ is a velocity estimate at the inlet in m/s and h is the mesh size in m. The elemental Reynolds number evaluates if the viscous forces ($Re_e \ll 1$) or the inertial forces ($Re_e \gg 1$) are dominant on the element scale. Dependent on the value of the elemental Reynolds number and thus if the viscous forces or the inertial forces are dominant, the maximum impermeability is defined by Theulings [40] as,

$$\overline{\alpha}^h = \begin{cases} 10^q \dfrac{\mu}{\rho h^2}, & \text{if } Re_e \leq 1, \\ 10^q \dfrac{|\vec{v}^f|}{h}, & \text{if } Re_e > 1, \end{cases} \tag{5.6}$$

where the bar over α ($\overline{\alpha}$) indicates it concerns a maximum value of α and 10^q can be used to increase the magnitude, where the penalization factor q is a small whole number (generally $q = 0$, $q = 1$, $q = 2$). It is important to note that the elemental Reynolds number is an initial guess before the simulations starts. From this initial guess the maximum impermeability is determined and thus the maximum impermeability is a fixed value throughout the domain. The maximum impermeability is thus not varying if it turns out that the elemental Reynolds number is different for particular elements. In the case of the bent channel the elemental Reynolds number is estimated as larger then one. By using the correct formulation for the maximum impermeability (where $Re^e > 1$) and a penalization factor $q = 1$, the maximum impermeability can be determined. The values for the maximum impermeability for the h_5 and h_{10} case are presented in Table 5.8.

Table 5.8: Maximum impermeability for the h_5 and h_{10} models.

Parameter	**Symbol**	**Value**	**Unit**
Maximum impermeability for h_5	$\overline{\alpha}_5^h$	1.1811×10^5	1/s
Maximum impermeability for h_{10}	$\overline{\alpha}_{10}^h$	5.9055×10^4	1/s

Furthermore, note that the Heaviside projection filter for the ω penalization is reset to the initial values as we only investigate the MDI approach and do not investigate the Dilation approach. All parameters used in the MDI approach are shown in Table 5.9.

Table 5.9: Parameters used in the MDI method

Parameter	Symbol	Value	Unit
Reynolds number	Re_H	10^4	-
Darcy number	Da	10^{-6}	-
Darcy curvature penalization	q_{Da}	0.1	-
Darcy curvature penalty for k	q_k	0.1	-
Darcy curvature penalty for ω	q_ω	10^{-4}	-
Impermeability penalization	q	1	-
Projection slope	β	6	-
Projection point	η	0.5	-

5.2.1. Results on the Mesh dependent impermeability method

In this section the MDI approach is investigated by examining the errors of the velocity, specific dissipation rate and turbulent kinetic energy.

Velocity (U)

Firstly, the velocity profiles for the h_5 and h_{10} cases are presented in Figure 5.7. In both cases it can be seen that the maximum velocity is increased in the middle of the channel compared to the reference models. Due to the higher impermeability less flow leaks through the solid domain and in combination with a slightly different velocity profile the maximum velocity is higher in the middle of the channel. The difference in the flow profile can be seen in the near wall regions (between $0.03 < y < 0.031$ and $0.039 < y < 0.04$), here the flow is underestimated compared to the reference models and this is compensated for in the middle of the channel. In Table 5.10 the flow leakage for the MDI and Dilation method are presented. It can indeed be seen that the flow leakage is significantly decreased in the MDI method due to the increased impermeability. A second improvement of the MDI method is that the velocity approaches zero at the wall where the Dilgen method does not, as can be seen in Figure 5.7b and Figure 5.7d for respectively the h_5 and h_{10} models. Due to well determined maximum impermeability in this problem, which is higher than in the Dilgen method where $\overline{\alpha} = 10^4$, the penalizations in the near wall and solid region become higher. Therefore the velocity is pushed to the imposed boundary targets at the wall.

Table 5.10: Leaked flow overview for the MDI method and the Dilgen method added for comparison.

h_x	MDI leaked flow	Dilgen leaked flow
h_5	0.84 %	6.57 %
h_{10}	1.84 %	7.78 %

Overall the errors are quite low in the upper and lower channel as can be seen in Table 5.11 although the errors in the previously presented Dilation method remain lower as shown in Table 5.4. The increase in error is caused by the high maximum velocity in the middle of the channel. In this case the problem at the wall and boundary conditions is improved however the overall problem is not improved. The velocity for the MDI method in the lower channel can be found in Appendix C.3.

Table 5.11: RRMSE of the velocity on the cut lines in the upper and lower channel for the MDI method. The RRMSE of the Dilgen method are included as well for comparison.

		MDI method		Dilgen method	
Location	w.r.t.	h_5	h_{10}	h_5	h_{10}
Upper channel	Reference best case	5.95 %	9.35 %	4.62 %	6.33 %
	Reference h_X case	5.75 %	5.79 %	4.48 %	4.77 %
Lower channel	Reference best case	9.61 %	13.55 %	11.13 %	14.34 %
	Reference h_x case	7.80 %	7.73 %	10.12 %	9.50 %

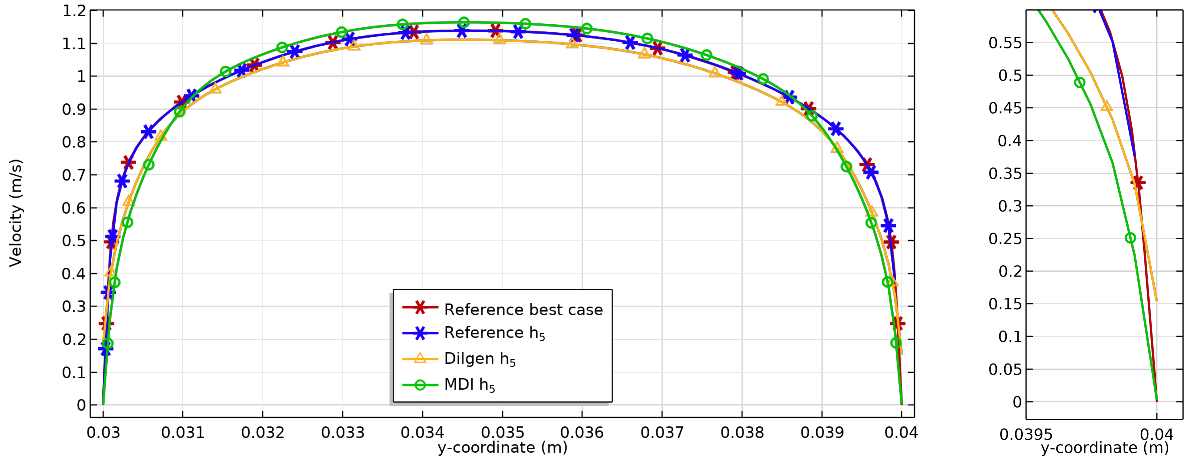

(a) Velocity profile for h_5.

(b) Velocity profile at the fluid/solid interface for h_5.

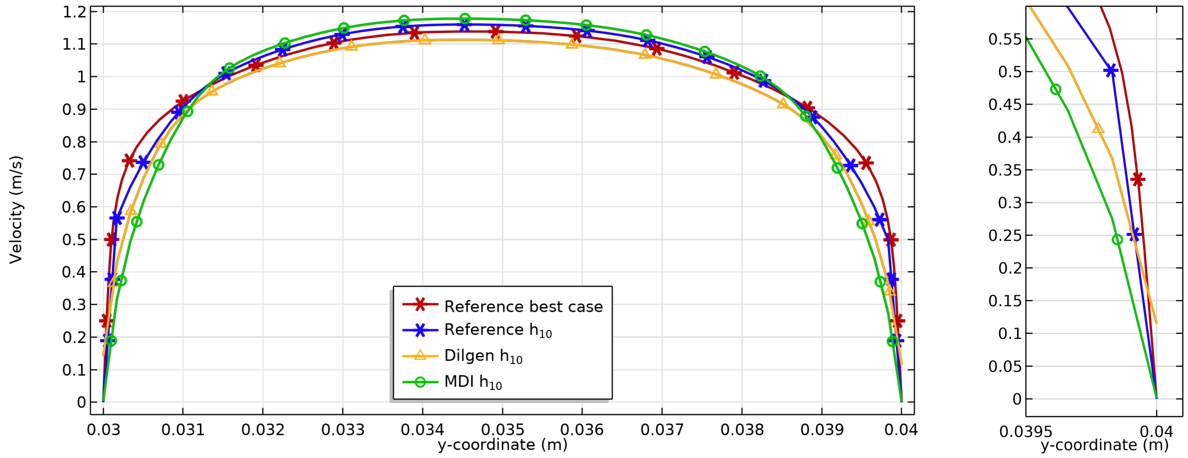

(c) Velocity profile for h_{10}.

(d) Velocity profile at the fluid/solid interface for h_{10}.

Figure 5.7: Velocity profile in the upper channel with the MDI method.

Specific dissipation rate (ω)

In case of the specific dissipation rate no large improvement can be noticed when compared to the Dilgen method. In Figure 5.8a, where the specific dissipation rate for the h_5 is shown, it can be seen that the specific dissipation rate is slightly higher at the wall but also has a larger error further away from the wall. In the h_{10} case the results further away from the wall are even worse, as can be seen around $y = 0.031\ m$ in Figure 5.8c. The specific dissipation rate for the MDI method in the lower channel can be found in Appendix C.3.

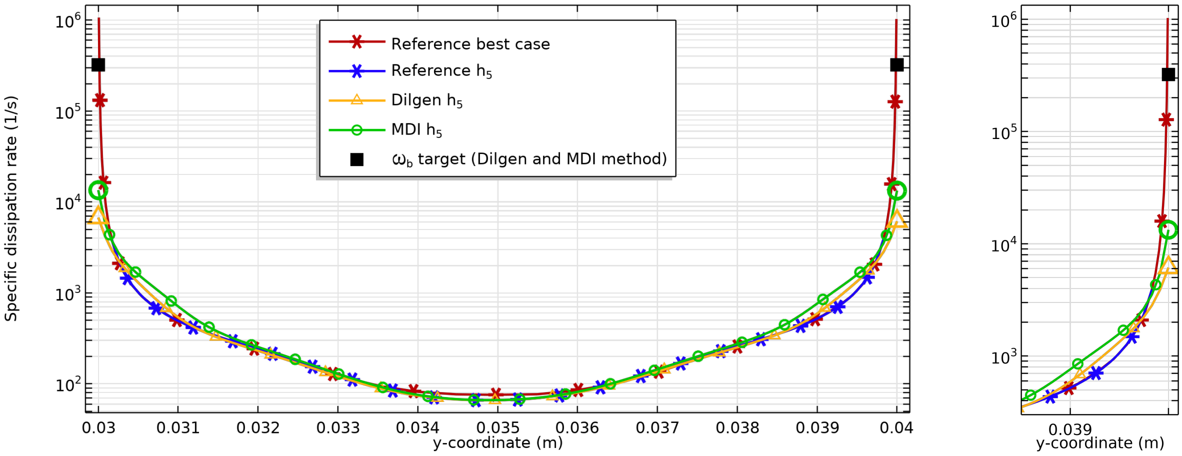

(a) Specific dissipation rate for h_5.

(b) Specific dissipation rate at the fluid/solid interface for h_5

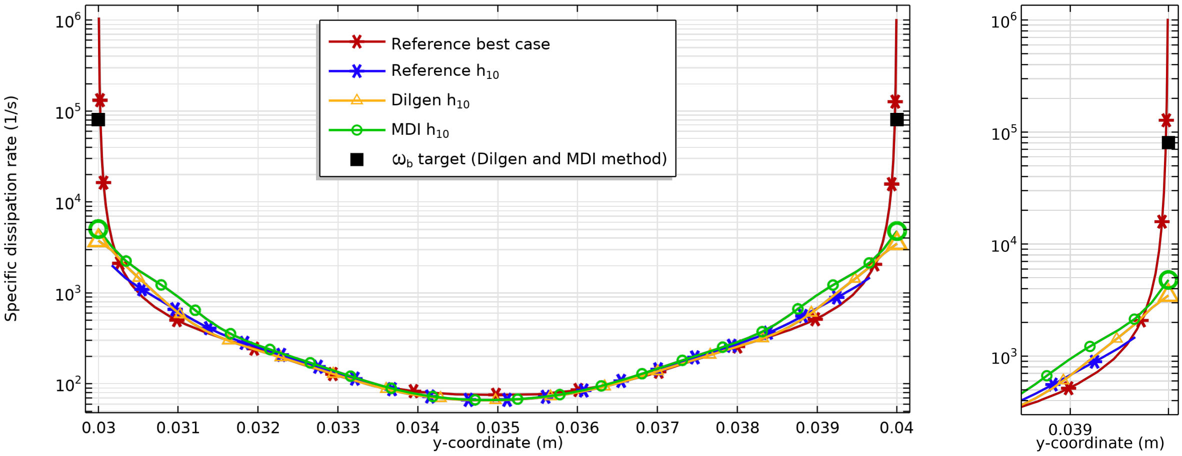

(c) Specific dissipation rate for h_{10}.

(d) Specific dissipation rate at the fluid/solid interface for h_{10}

Figure 5.8: Specific dissipation rate in the upper channel with the MDI method for h_5 and h_{10}

The specific dissipation rate for h_5 is shown on an extended cut line in Figure 5.9. Here it can be clearly seen that the specific dissipation rate can reach higher values in the MDI method, this is due the increase in maximum impermeability. However, if we look at the solid/fluid interface (at the dashed line) we see that the difference between the MDI approach and the Dilgen approach is negligible. A similar problem as in the Dilgen method thus occurs where the penalties are 'activated' too far into the solid domain past the fluid/solid interface. The specific dissipation rate is not improved as

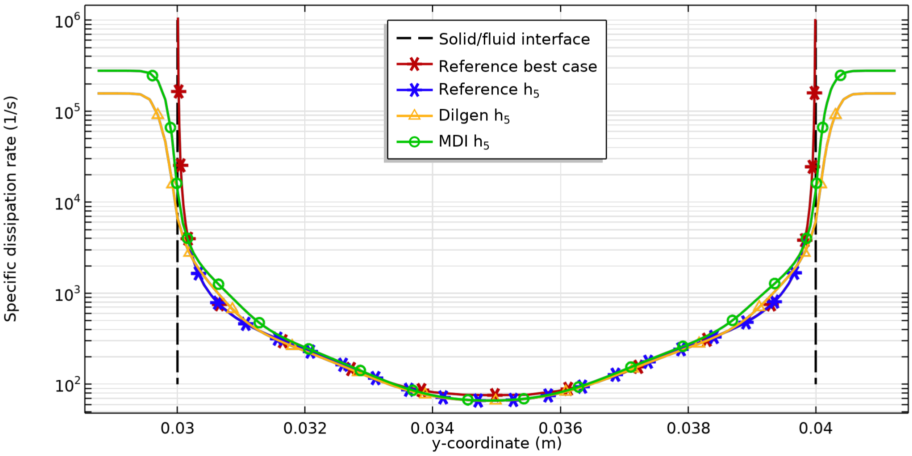

Figure 5.9: Specific dissipation rate at an extended cut line in the upper channel.

can be seen by analyzing the cut lines in the upper channel, this is confirmed by the errors in Table 5.12. The errors are in the same order as in the Dilgen method and the MDI method is not an improvement on its own regarding the specific dissipation rate. However, it must be commented that with this method the specific dissipation rate is able to reach higher values although this just happens in the solid domain instead of at the fluid/solid interface.

Table 5.12: RRMSE of the specific dissipation rate on the cut lines in the upper and lower channel with the MDI method. The RRMSE of the Dilgen method are included as well for comparison.

		MDI method		**Dilgen method**	
Location	**w.r.t.**	h_5	h_{10}	h_5	h_{10}
Upper channel	Reference best case	98.04 %	99.20 %	98.99 %	99.39 %
	Reference h_x case	97.12 %	98.83 %	98.51 %	99.11 %
Lower channel	Reference best case	98.03 %	99.21 %	99.03 %	99.49 %
	Reference h_x case	97.10 %	98.86 %	98.56 %	99.26 %

Turbulent kinetic energy (k)

Finally, the turbulent kinetic energy is analyzed as shown in Figure 5.10. First, analyzing the MDI method h_5 results in Figure 5.10a it can be seen that the turbulent kinetic energy reaches the boundary target of zero at the wall. As before, the specific dissipation rate and turbulent kinetic energy have a relation where the specific dissipation rate dampens out the turbulent kinetic energy. Since the specific dissipation is not increased in the near wall region the turbulent kinetic energy is not damped out well enough, resulting in some significant peaks of turbulent kinetic energy. For the MDI method with h_{10} mesh size similar conclusions can be drawn, where a large peak of turbulent kinetic energy is present in the near wall region and the boundary target at the wall is achieved. The turbulent kinetic energy for the MDI method in the lower channel can be found in Appendix C.3.

Furthermore, when comparing the errors in Table 5.13 no large improvements can be noticed when comparing to the Dilgen method, which is expected after analyzing Figure 5.10.

Table 5.13: RRMSE of the turbulent kinetic energy on the cut lines in the upper and lower channel with the MDI method. The RRMSE of the Dilgen method are included as well for comparison.

		MDI method		**Dilgen method**	
Location	**w.r.t.**	h_5	h_{10}	h_5	h_{10}
Upper channel	Reference best case	94.42 %	142.86 %	91.92 %	111.65 %
	Reference h_x case	97.59 %	37.32 %	95.07 %	18.82 %
Lower channel	Reference best case	49.49 %	74.61 %	43.89 %	67.11 %
	Reference h_x case	41.53 %	30.07 %	36.40 %	22.32 %

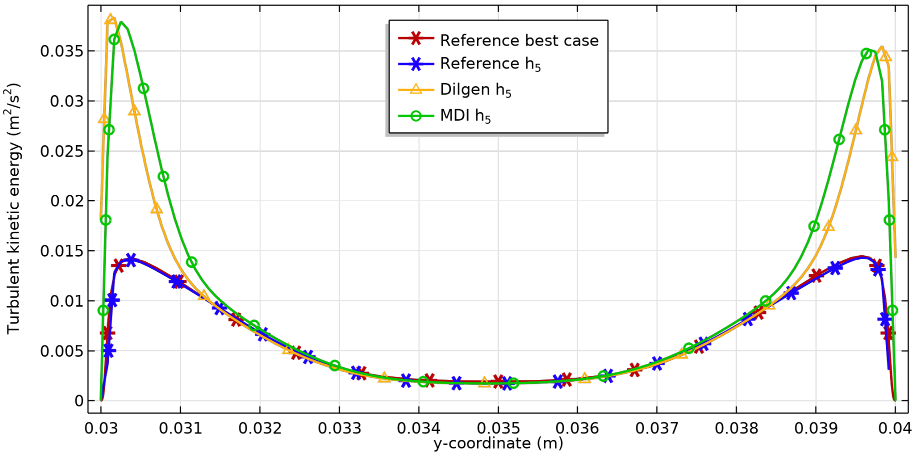

(a) Turbulent kinetic energy for h_5.

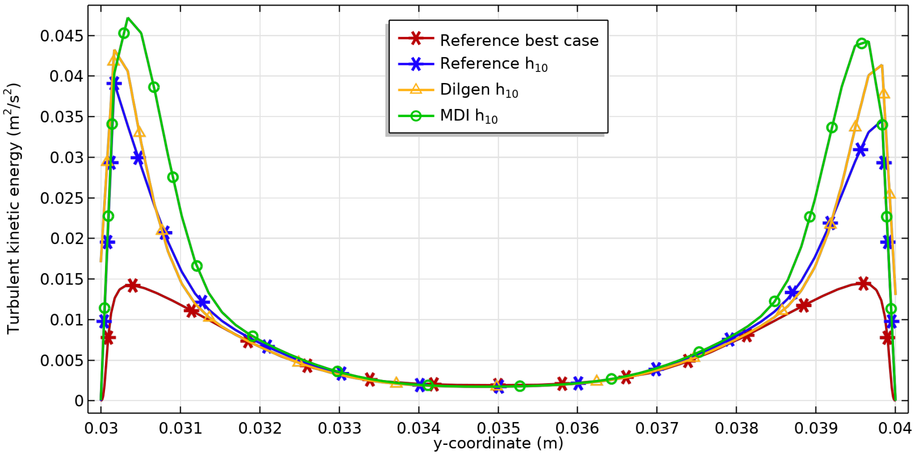

(b) Turbulent kinetic energy for h_{10}.

Figure 5.10: Turbulent kinetic energy in the upper channel with the MDI method for h_5 and $_{10}$.

5.2.2. Discussion on the Mesh dependent impermeability method

In this method the maximum impermeability is increased when compared to the Dilgen method. By using this higher impermeability the solid regions are less porous and stop more flow from passing through the solid domains. Therefore the boundary conditions for the velocity and turbulent kinetic energy were achieved at the wall. Unfortunately this was not the case for the specific dissipation rate at the wall. In the region slightly further away from the wall the results did not improve either, mainly caused by the low specific dissipation rate which did not dampen the turbulent kinetic energy enough, resulting in significant peaks. It can thus be concluded that this method works for reaching the boundary conditions for velocity and turbulent kinetic energy but it does not improve the overall RRMSE results. Finally, all the errors throughout the whole domain regarding the MDI method are presented in Table 5.14. Comparing these results to the Dilgen method indeed shows no significant improvements and thus it can be concluded that this method is no improvement on the Dilgen method.

Table 5.14: RRMSE throughout the whole domain with the Mesh dependent impermeability method with respect to reference best case and reference with corresponding h_x mesh.

		MDI method			**Dilgen method**		
w.r.t.	h_x	**RRMSE** U	**RRMSE** k	**RRMSE** ω	**RRMSE** U	**RRMSE** k	**RRMSE** ω
reference best case	h_5	9.14 %	54.87 %	98.46 %	10.39 %	48.22 %	99.24 %
	h_{10}	12.90 %	84.57 %	98.17 %	13.26 %	75.91 %	98.78 %
reference h_x case	h_5	8.01 %	50.06 %	98.55 %	9.62 %	43.57 %	99.31 %
	h_{10}	7.16 %	37.09 %	97.84 %	8.63 %	30.88 %	98.57 %

5.3. Mesh dependent impermeability with dilation method

The two previous presented methods, the Dilation method and MDI method, showed improvements in different aspects of the simulation. The Dilation method is capable of shifting the specific dissipation rate penalty to different locations and places the penalty in the correct region. The MDI method adjusts the impermeability according to the given boundary conditions resulting in penalties of different magnitudes. Therefore these two methods are combined in this section resulting in the Mesh dependent impermeability with dilation method (MDI-D method). As explained in Section 5.1 the dilation can be determined precisely. To shift exactly one element a projection threshold of 0.82 is used in combination with a blurring filter radius which is equal to the mesh size. The projection slope for ω is also similar as in the proposed Dilation method in Section 5.1, thus 80 which is different from the parameters proposed in Table 4.2. The values for the maximum impermeability are shown in Table 5.15. Since the boundary conditions are identical the values for the maximum impermeability are the same as in the MDI method.

Table 5.15: Maximum impermeability dependent for the h_5 and h_{10} models.

Parameter	Symbol	Value	Unit
Maximum impermeability for h_5	$\overline{\alpha}_5^h$	1.1811×10^5	1/s
Maximum impermeability for h_{10}	$\overline{\alpha}_{10}^h$	5.9055×10^4	1/s

The other parameters used in this case are summed up in Table 5.16.

Table 5.16: Parameters used in the MDI-D method.

Parameter	Symbol	Value	Unit
Reynolds number	Re_H	10^4	-
Darcy number	Da	10^{-6}	-
Darcy curvature penalization	q_{Da}	0.1	-
Darcy curvature penalty for k	q_k	0.1	-
Darcy curvature penalty for ω	q_ω	10^{-4}	-
Impermeability penalization	q	1	-
Projection slope	β	6	-
Projection point	η	0.5	-
Projection slope ω	β_ω	80	-
Projection point ω	η_ω	0.82	-

5.3.1. Results on the Mesh dependent impermeability with dilation method

The results of the velocity, specific dissipation rate and turbulent kinetic energy with this MDI-D method are evaluated in this subsection.

Velocity (U)

The velocity profiles in the upper channel for this method are shown in Figure 5.11. In these figures it can be seen that the velocity profile is significantly improved and matches the reference results in the middle of the channel. On the solid/fluid interface the velocity reaches zero as can be seen in Figure 5.11b. However this figure also shows that the velocity close to the wall does not completely match the reference results. For the h_{10} model in Figure 5.11c it is shown that the results matches the reference simulation with the same y^+ mesh in the free stream. This is the best possible accuracy since there is no complete mesh convergence for the h_{10} simulations, this can be observed since the reference best case and reference h_{10} case differ in the middle of the channel. The h_{10} results shows the same behavior at the wall as the h_5 case where it reaches zero at the wall but has a slightly different behavior a small distance from the wall. As the velocity profiles match the reference simulations quite well the flow leakage should be reduced as well. The calculated flow leakage percentages are presented in Table 5.17, where there is a significant decrease in flow leakage when compared to the Dilgen method. The flow leakage in the h_5 model is almost reduced to zero, meaning that the porous material stops the most fluid from leaving the domain at the open boundary. By visually inspecting the results in the upper channel the MDI-D method shows a quite accurate behavior, however the RRMSE's on these cut lines as shown in Table 5.18 are not significantly decreased in the upper channel. However, the lower channel showed a decrease in error, going from 11.13 with the Dilgen approach to 8.31 with the MDI-D approach for the h_5 case with respect to the reference best case simulation. The velocity figures for the MDI-D method in the lower channel can be found in Appendix C.4.

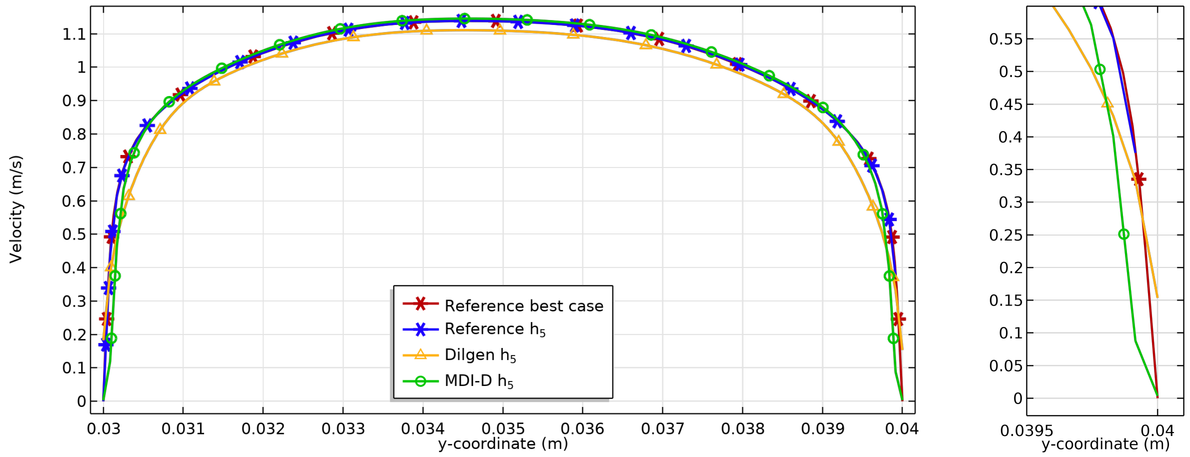

(a) Velocity profile for h_5.

(b) Velocity profile at the fluid/solid interface for h_5.

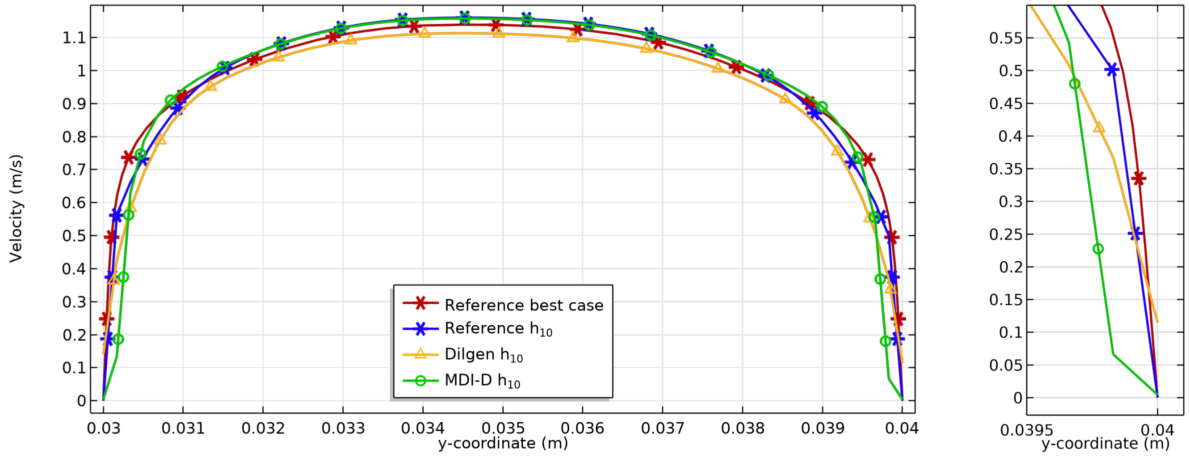

(c) Velocity profile for h_{10}.

(d) Velocity profile at the fluid/solid interface for h_{10}.

Figure 5.11: Velocity profiles in the upper channel with the MDI-D method for h_5 and h_{10}.

Table 5.17: Leaked flow overview for the MDI-D method and the Dilgen method added for comparison.

h_x	**MDI-D leaked flow**	**Dilgen leaked flow**
h_5	0.59 %	6.57 %
h_{10}	1.13 %	7.78 %

Table 5.18: RRMSE of the velocity on the cut lines in the upper and lower channel with the MDI-D method.

		MDI-D method		**Dilgen method**	
Location	**w.r.t.**	h_5	h_{10}	h_5	h_{10}
Upper channel	Reference best case	4.37 %	9.06 %	4.62 %	6.33 %
	Reference h_x case	4.07 %	8.81 %	4.48 %	4.77 %
Lower channel	Reference best case	8.31 %	20.82 %	11.13 %	14.34 %
	Reference h_x case	7.46 %	19.76 %	10.12 %	9.50 %

Specific dissipation rate (ω)

The specific dissipation rate is discussed in this section, where the specific dissipation rate in the upper channel can be found in Figure 5.12. In contrary to the MDI method (Section 5.2) and Dilgen method (Section 4.2), specific dissipation rate with the MDI-D method reaches significant higher values at the wall. In the h_5 case this can be seen in Figure 5.12a where again the gap between the specific dissipation rate at the fluid/solid interface and the ω_b target is negligible for the MDI-D method. The same can be observed in Figure 5.12c. Due to the dilation the specific dissipation rate does not match the reference completely which is caused by the gray elements where the penalty is still active, this is even worse in the h_{10} case. The specific dissipation rate for the MDI-D method in the lower channel can be found in Appendix C.4.

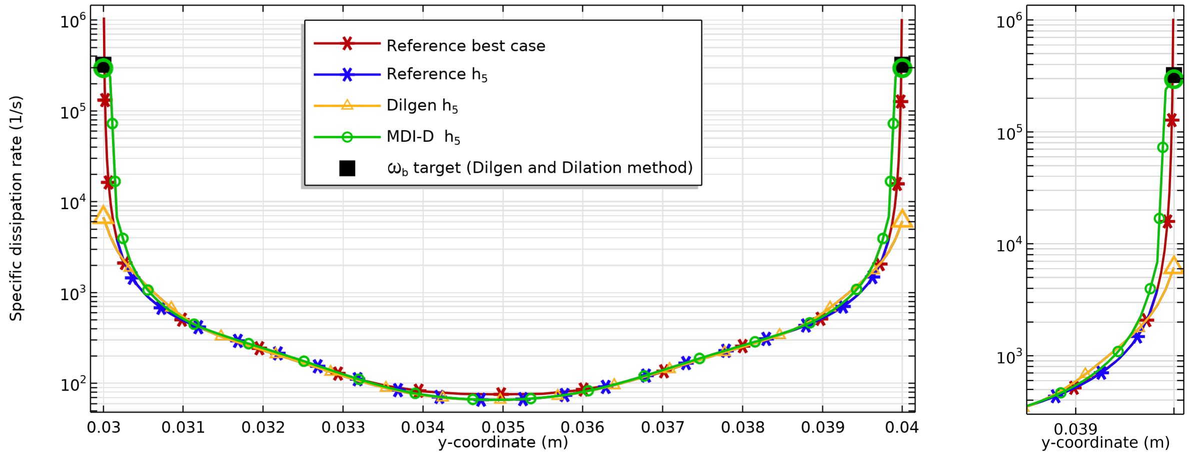

(a) Specific dissipation rate for h_5.

(b) Specific dissipation rate at the fluid/solid interface for h_5

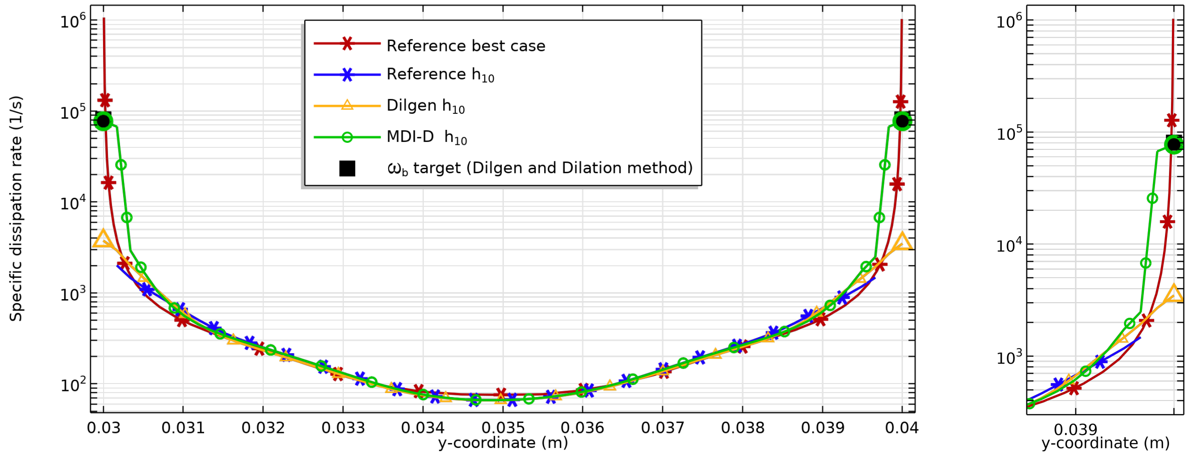

(c) Specific dissipation rate for h_{10}.

(d) Specific dissipation rate at the fluid/solid interface for h_{10}

Figure 5.12: Specific dissipation rate in the upper channel with the MDI-D method.

The RRMSE regarding the specific dissipation rate for the MDI-D method can be found in Table 5.19. The errors are again relatively high which means that the specific dissipation rate at the wall for this method is still too low. However, it can be seen that there is an improvement of at least 10% when comparing the MDI-D method with the Dilgen method with respect to the reference best case.

Table 5.19: RRMSE of the specific dissipation rate on the cut lines in the upper and lower channel with the MDI-D method.

		MDI-D method		**Dilgen method**	
Location	**w.r.t.**	h_5	h_{10}	h_5	h_{10}
Upper channel	Reference best case	86.68 %	92.58 %	98.99 %	99.39 %
	Reference h_x case	97.40 %	91.30 %	98.51 %	99.11 %
Lower channel	Reference best case	86.55 %	92.60 %	99.03 %	99.49 %
	Reference h_x case	97.44 %	91.36 %	98.56 %	99.26 %

Turbulent kinetic energy (k)

When analyzing the specific dissipation rate it is found that the value at the wall increased which should also influence the turbulent kinetic energy at the wall. This is indeed the case as can be seen in Figure 5.13. Especially for the h_5 case a great improvement is found where the turbulent kinetic energy almost shows the same behavior as the reference simulations (Fig. 5.13a). In the h_{10} case it can be seen that the gray area is larger since the elements are larger which results in a stronger penalization and thus a lower turbulent kinetic energy in the near wall region. The turbulent kinetic energy figures for the MDI-D method in the lower channel can be found in Appendix C.4.

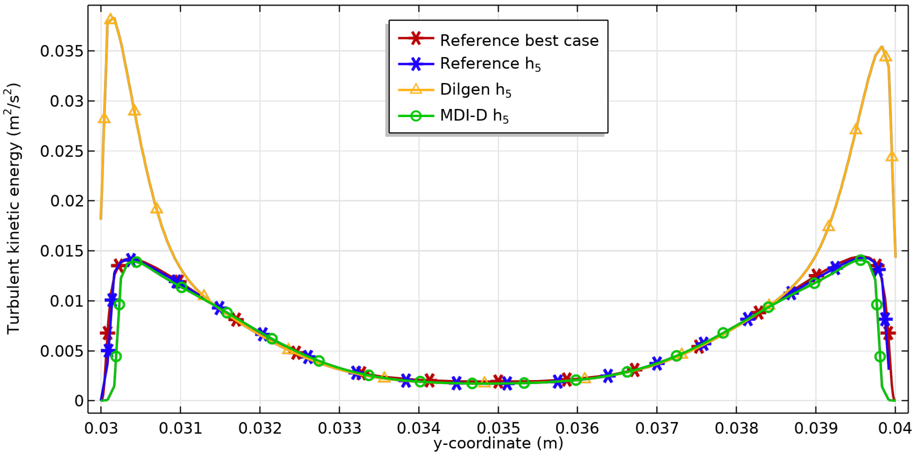

(a) Turbulent kinetic energy for h_5.

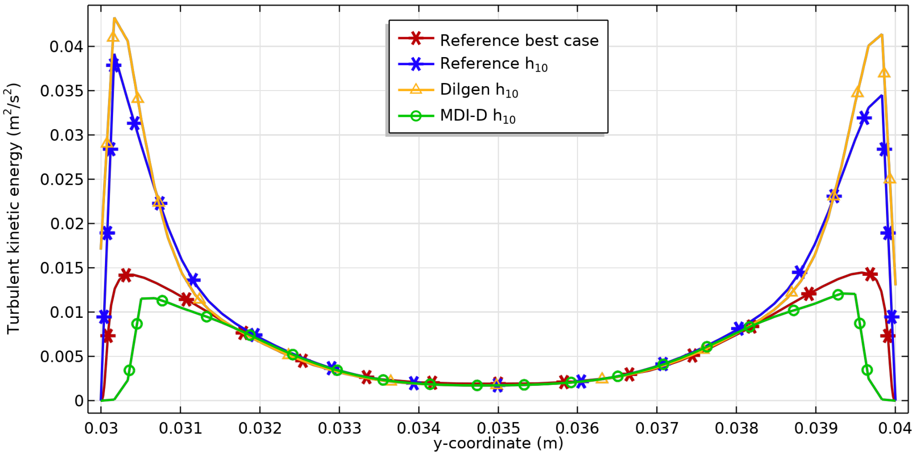

(b) Turbulent kinetic energy for h_{10}.

Figure 5.13: Turbulent kinetic energy in the upper channel with the MDI-D method.

The results of the turbulent kinetic energy RRMSE of this method can be found in Table 5.20. The error of the h_5 model with respect to the reference h_5 case for the MDI-D method is reduced to 18.08% while the Dilgen method shows here an error of 95.07%. This could be quantified as a significant improvement on the Dilgen method since all errors are reduced significantly, except for the MDI-D h_{10} mesh with respect to the reference h_{10} case the errors are increased.

Table 5.20: RRMSE of the turbulent kinetic energy on the cut lines in the upper and lower channel with the MDI-D method.

		MDI-D method		**Dilgen method**	
Location	**w.r.t.**	h_5	h_{10}	h_5	h_{10}
Upper channel	Reference best case	20.42 %	39.94 %	91.92 %	111.65 %
	Reference h_x case	18.13 %	38.83 %	95.07 %	18.82 %
Lower channel	Reference best case	30.23 %	59.68 %	43.89 %	67.11 %
	Reference h_x case	24.45 %	52.94 %	36.40 %	22.32 %

5.3.2. Analyzing the influence of the Heaviside projection slope

The Heaviside projection slope is an important parameter in Topology Optimization, higher slopes result in sharper designs. However, if the slope becomes too steep this can influence the stability of the simulation in a negative manner causing physics related convergence errors. In this chapter a test case has been used where the geometry is not changing, which allows higher projection slopes to be used before convergence errors occur. In Topology Optimization, geometries do change, so it is important to see how the newly developed MDI-D method reacts when using different projection slopes. Therefore an additional simulation on a fixed geometry is performed where several projection slopes β are used, with the following values: $6, 10, 14, 20, 80$. In the Topology Optimization cases the projection slopes for the *Darcy-* and *k-penalization* are increased as well and thus this is also the case in this comparison section. Finally, this test is performed on the bent channel geometry with the h_{10} fixed mesh size.

First, in Figure 5.14 the impermeability for the ω penalization α_ω is shown on the extended upper channel cut line. The impermeability is shown for both the Dilgen and the MDI-D method and is computed using the same $\beta = 14$. The fluid/solid interface is indicated by the dashed line while one elemental distance of this interface is indicated with dotted lines. This clearly shows that with the dilation, the penalization is shifted one element, thus increasing the impermeability at the fluid/solid interface. The close up in Figure 5.14b shows a several orders difference between α_ω for both methods at the fluid/solid interface.

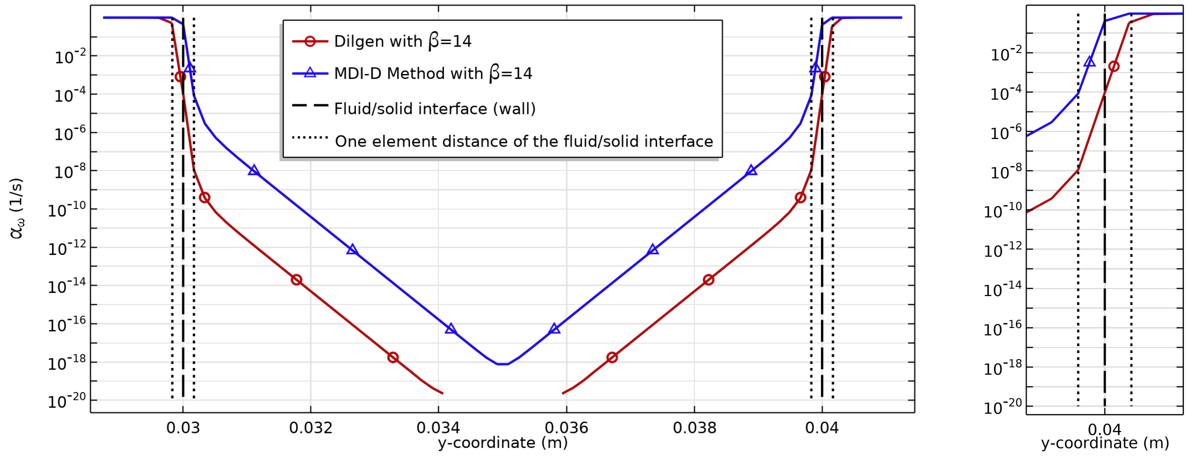

(a) Full overview on the extended cut line.

(b) Close up on the fluid/solid interface.

Figure 5.14: α_ω shown on the extended upper channel for both the Dilgen and MDI-D method with a projection slope of $\beta = 14$. The fluid/solid interface is indicated as well one elemental distance from the fluid/solid interface.

Secondly, the influence of the different projection slopes is shown on the specific dissipation rate distribution in Figure 5.15 for the Dilgen and MDI-D methods. In this figure it is shown that the specific dissipation rate at the fluid/solid interface increases when the projection slope increases as well. A higher projection slope thus contributes to a better approximation of the ω_b target, the $\beta = 20$ almost reaches the ω_b target in the MDI-D case. In the Dilgen method it is shown that the values at the fluid/solid interface are significantly lower and even with the highest projection slope $\beta = 80$ a relatively bigger difference to the ω_b target can be observed.

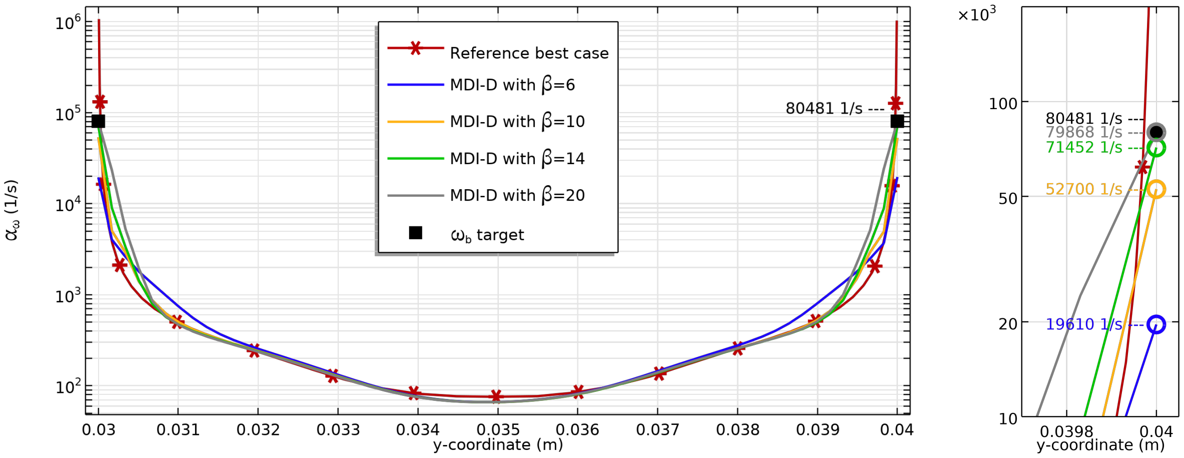

(a) Specific dissipation rate in the upper channel for different Heaviside projection slopes for the MDI-D method.

(b) Close up at the fluid/solid interface with MDI-D method

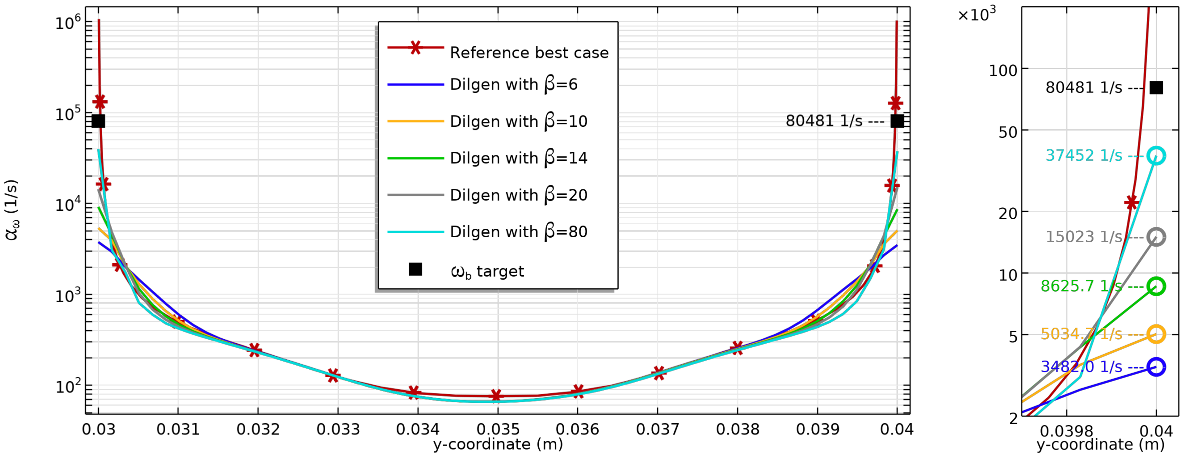

(c) Specific dissipation rate in the upper channel for different Heaviside projection slopes for the Dilgen method.

(d) Close up at the fluid/solid interface with the Dilgen method

Figure 5.15: Specific dissipation rate in the upper channel for the MDI-D and Dilgen method. Be aware that 5.15b and 5.15d are shown using different scales. Therefore the actual values at the fluid/solid interface in the close up figures are presented as well.

The actual ω values at the solid/fluid interface are compared to the ω_b target value which is 80 481 1/s, according to Equation 4.9. The relative error between the actual value and the ω_b target value is determined and presented in Table 5.21. In this case the *Darcy-* and *k-penalization* have higher projection slopes as well, this is resulting in convergence errors for the MDI-D method for $\beta = 80$ as can be seen in Table 5.21. In the previous sections where only the ω penalization has a high projection slope we did not face any convergence errors. However, this shows that higher projection slopes indeed cause instabilities in the simulation. It can be seen that even the highest projection slope $\beta = 80$ for the Dilgen method has a significant error and it only performs better than the MDI-D method with $\beta = 6$. Focusing on the ω value at the solid/fluid interface, the MDI-D method clearly outperforms the Dilgen method. This is due to both the Dilation and the newly determined maximum impermeability. First, by increasing the maximum impermeability, higher ω values can be reached. Secondly, it is shown that increasing the projection slope contributes to the higher ω at the solid/fluid interface. The ω at the solid/fluid interface with a projection slope of 20 is around 4 times higher than with a slope of 6. This results in a significant decrease in error, from 75.6% to 0.8%.

Table 5.21: ω values at the solid/fluid interface at the presented cut lines and there relative errors to the ω_b target of $80\,481\ 1/\mathrm{s}$

	MDI-D method		**Dilgen method**	
β	**ω at solid/fluid interface**	**Error w.r.t ω_b target**	**ω at solid/fluid interface**	**Error w.r.t ω_b target**
6	$19\,610\ 1/\mathrm{s}$	75.6 %	$3482\ 1/\mathrm{s}$	95.7 %
10	$52\,700\ 1/\mathrm{s}$	34.5 %	$5035\ 1/\mathrm{s}$	93.7 %
14	$71\,452\ 1/\mathrm{s}$	11.2 %	$8626\ 1/\mathrm{s}$	89.3 %
20	$79\,868\ 1/\mathrm{s}$	0.8 %	$15\,023\ 1/\mathrm{s}$	81.3 %
80	-	-	$37\,452\ 1/\mathrm{s}$	53.5 %

5.3.3. Discussion on the Mesh dependent impermeability with dilation method

In this section MDI-D method is presented which is a combination of the Dilation method presented in Section 5.1 and the MDI method presented in 5.2. The Dilation method showed that the behavior of the specific dissipation rate at the wall could be improved and the MDI method showed that the behavior of the turbulent kinetic energy and the velocity could be improved at the wall. Thus a combination of those two should improve the model even more which is indeed the case when evaluating the overall RRMSE as presented in Table 5.22. All RRMSE's regarding the h_5 case are improved when compared to the Dilgen method. The h_{10} results shows an inconsistent behavior where the velocity errors are increased for the reference best case and reference h_x case. However, the specific dissipation rate errors for the h_{10} case are both reduced compared to the Dilgen method.

Table 5.22: RRMSE of the MDI-D method with respect to reference best case and reference h_x case.

		MDI-D method			**Dilgen method**		
w.r.t.	h_x	**RRMSE U**	**RRMSE k**	**RRMSE ω**	**RRMSE U**	**RRMSE k**	**RRMSE ω**
reference best case	h_5	8.36 %	25.82 %	88.01 %	10.39 %	48.22 %	99.24 %
	h_{10}	18.22 %	49.25 %	89.50 %	13.26 %	75.91 %	98.78 %
reference h_x case	h_5	7.34 %	21.33 %	87.94 %	9.62 %	43.57 %	99.31 %
	h_{10}	14.09 %	45.76 %	90.30 %	8.63 %	30.88 %	98.57 %

5.4. Conclusions on the improved methods

In this chapter we investigated several methods to improve on the state-of-the-art Dilgen method for turbulent flow Topology Optimization. First, the Dilation method is proposed where the specific dissipation rate penalty is shifted into the fluid domain. Due this shift the ω_b target is better approached, and consequently the boundary targets for the velocity and turbulent kinetic energy improved as well. A second method is presented, the MDI method, where the maximum impermeability is dependent on the mesh size. Introducing this method resulted in an impermeability adjusted to the given design problem and boundary conditions. Therefore, the flow penalization is more accurate than in the Dilgen method. The final method presented, the MDI-D method, is a combination of the previous mentioned methods. Since the first two methods showed improvements in different aspects of the simulation problem, a combination of those two seemed promising. The Dilation method places the penalizations in the correct region and the MDI method adjusted the penalties to the correct order of magnitude. The MDI-D method indeed showed the overall best results. The RRMSE of the MDI-D and Dilation method on the full domain, as discussed in Section 5.3.3, are summarized in Table 5.23. This table shows the results regarding the h_5 model with respect to the reference best case and reference h_x models. The results on the MDI-D method gave the best improvements and results when compared to the Dilgen method. Therefore, this method is used in the Topology Optimization cases in the following chapter.

Table 5.23: RRMSE of the MDI-D method versus the Dilgen method.

		MDI-D method			**Dilgen method**		
w.r.t.	h_x	**RRMSE U**	**RRMSE k**	**RRMSE ω**	**RRMSE U**	**RRMSE k**	**RRMSE ω**
Reference best case	h_5	8.36 %	25.82 %	88.01 %	10.39 %	48.22 %	99.24 %
Reference h_x case	h_5	7.34 %	21.33 %	87.94 %	9.62 %	43.57 %	99.31 %

6

Topology optimization comparison of the improved method versus the Dilgen method

In this chapter two Topology Optimization approaches are investigated and compared. First, in Section 6.1 the Dilgen method and the MDI-D method are tested on a simple case where only the pressure drop is optimized. This first case is mainly used to test the functionality of the methods in a TO case. Secondly, in Section 6.2 an optimization problem of a flow around an internal wall is evaluated. Additionally to the TO cases in this Chapter, a TO case including heat transfer is presented in Appendix B.3.

6.1. Pressure drop minimization

First the optimization set up and boundary conditions are described. The problem under consideration must show the improvements of the MDI-D method in a Topology Optimization case. We therefore optimize a simple problem for pressure drop such that we can easily investigate errors in the simple optimum. The geometry for this problem can be found in Figure 6.1. As can be seen there is an optimization domain (Ω_d) of 3 times the characteristic length H ($3H$ by $3H$). Furthermore to save computation time, the inlet length is reduced to $3H$ instead of $10H$ (which is a rule of thumb in CFD simulation) and the outlet length is set to H. At the in- and outlet the design variable is fixed to $\gamma = 1$ which corresponds to fully fluid, also a no slip boundary condition is implemented at the wall in the inlet and outlet. It is undesired that the fluid in the optimization domain is influenced by boundary conditions at the wall, therefore a buffer zone is placed around the optimization domain. This buffer zone should correspond to solid material and is thus fixed at $\gamma = 0$. This region has a thickness equal to the size of four elements and will thus vary in size if different mesh sizes (h_{mesh}) are used, this prevents that an excessive amount of elements are generated in this region and thus saving computation time. To prevent the fluid from leaking out of the domain, a slip wall boundary condition is implemented at the outer edge of this buffer region, ideally this would be a no slip wall, however this is not possible since the active penalties in this region (due to the fixed $\gamma = 0$) clashes with the physics COMSOL implies at no slip walls. Finally, to save more computation time a symmetry boundary condition is applied to the top boundary of the inlet, optimization and outlet domains. The material properties used in this case are the same as in previous chapters and can be found in Table 4.1.

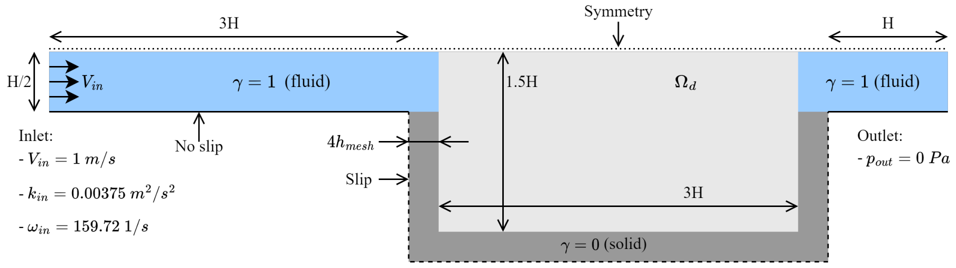

Figure 6.1: Geometry of the pressure drop minimization optimization.

We optimize for the turbulent Reynolds number of $Re = 10^4$ and the characteristic length is $H = 0.01\ m$. The maximum inlet velocity is computed as $V_{in} = 1\ m/s$ using the material parameters in Table 4.1 and Equation 4.1. Finally, a certain amount of turbulence is specified at the inlet in terms of the inlet turbulent kinetic energy (k_{in}) and inlet specific dissipation rate (ω_{in}), which are based on default equations and parameters inside the COMSOL module.

The inlet turbulent kinetic energy k_{in} is determined by using Equation 4.2 and the inlet specific dissipation ratio ω_{in} by Equation 4.3.

The turbulence model used is based on the Low Reynolds model and therefore the first element at the wall must be in the viscous sublayer which is for values $y^+ \leq 11.25$. In this case the element size is set to $h = 10y^+$ which results in a mesh size for which we can optimize within a reasonable time frame. At the start of the optimization the final geometry is unknown and thus no mesh refinements can be created near a wall, therefore a uniform distributed grid is used. The mesh size of the elements is determined by the desired $y^+ = 10$ and obtained with the following formula,

$$h_{mesh} = \frac{y^+\mu}{u_\tau \rho_f}, \tag{6.1}$$

where the friction velocity (u_τ) is determined according Equation 3.18. The objective function (H) for this optimization case is minimizing the pressure drop in the channel. A pressure drop can be formulated as the difference between the pressure at the inlet and at the outlet. The pressure drop in equation form can thus be written as:

$$\Delta p = \overline{p}_{in} - \overline{p}_{out}, \tag{6.2}$$

where $\overline{p}_{in}$ is the average pressure at the inlet in Pa and $\overline{p}_{out}$ is the average pressure at the outlet in Pa. Furthermore, we apply a constraint on the fluid volume and the optimization problem can thus be formulated as:

$$\boxed{\begin{array}{ll} \underset{\gamma(\vec{x})}{\text{minimize}} & H = \dfrac{\overline{p}_{in} - \overline{p}_{out}}{p_{ref}} \\ \text{subject to} & R\,(u(\vec{x}), \gamma(\vec{x})) = 0, \quad \vec{x} \in \Omega, \\ & \overline{\gamma}_\Omega \leq 0.34, \end{array}} \tag{6.3}$$

where R are the PDE constraints which are in this case the $k - \omega$ equations, so the RANS Equation 3.26, the kinetic energy Equation 3.27 and the specific dissipation rate Equation 3.28. The reference pressure (p_{ref}) is based on an initial simulation of the fluid through the open domain as specified in Figure 6.1, where the reference pressure is equal to the average pressure at the inlet minus the average pressure at the outlet. The first constraint is a volume constraint, where the average value of all design variables in the domain ($\overline{\gamma}_\Omega$) is not allowed to be larger then 0.34. Thus the maximum amount of fluid in the domain can be 34%. The second constraint states that the design variable only can have values between zero (solid) and one (fluid). In Topology Optimization the physics in the intermediate density areas where $\gamma \approx 0.5$ can be considered less accurate, therefore a discrete $0/1$ design with a sharp solid/fluid interface is desired as explained in Section 3.3 . To obtain a sharp design a high projection slope can be used in the Heaviside projection filter as defined in Equation 3.31 in Section 3.3. However if a high projection slope β is used from the start of the optimization, the optimization might become restricted and converge to an inferior local optimum. To prevent the optimization from converging to an inferior local optimum the projection slope has to be set at a low value (around $\beta = 1 - 2$) at the beginning of the optimization. Therefore, the projection slope is set to a low value at the start of the optimization but increases during the optimization process. In the continuation scheme we increase the projection slope if the design is converged for the current slope and does not change more than 0.1, or if a maximum of 50 design iterations are performed with the current projection slope. In COMSOL this continuation scheme is performed by using a parametric sweep of the projection slope, where the start design for each projection slope is the last design from the previous projection slope optimization. The projection slope starts at a value of 2 and increases with 2 after every step, when a projection slope 10 is reached the projection slope increases with steps of 4 until 22 is reached. In the first projection slope step an empty initial design is used where $\gamma_\Omega = 1$. In contrast to Sections 5.1 and 5.3 the maximum projection slopes is 22 instead of 80. Since in this TO case the geometry changes it is not desired to have a projection slope as high as 80. There is no distinction made between different projection slopes, thus all β are increasing equally. All important parameters discussed are summed up in Table 6.1.

Table 6.1: Parameter overview for all the optimization cases in this chapter.

Parameter	Symbol	Value	Unit
Characteristic length	H	0.01	m
Reynolds number	Re_H	10^4	-
Darcy number	Da	10^{-6}	-
Darcy penalization	q_{Da}	0.1	-
Darcy curvature penalty for k	q_k	0.1	-
Darcy curvature penalty for ω	q_ω	10^{-4}	-
Penalty on the maximum impermeability	q	1	-
Penalty factor convective heat transfer	n	3	-
Projection point	η	0.5	-
Projection slope	β	2, 4, 6, 8, 10, 14, 18, 22	-
Projection point ω	η_ω	0.7	-
Mesh size used for $y^+ = 10$	h_{10}	1.6933×10^{-4}	m
Blurring filter radius	R_{min}	3.3867×10^{-4}	m
Reference pressure	p_{ref}	263	Pa

Parameter difference for both methods in the Topology Optimization case

The two approaches which are tested on the optimization cases are the Dilgen method and the MDI-D method . In Section 6.1 all the boundary conditions and parameters are presented which are equal for both methods. There are two important differences between the Dilgen method and the MDI-D method. The first major difference is the impermeability value which represents the porosity of the solid and intermediate domains. For the Dilgen method the maximum impermeability is a fixed value based on the Darcy number and fluid material properties, calculated by the equation,

$$\overline{\alpha} = \frac{\nu}{DaH^2}. \tag{6.4}$$

In the MDI-D method, the maximum impermeability can be calculated with the following equation,

$$\overline{\alpha}^h = 10^q \frac{V_{in}}{h_{mesh}}, \tag{6.5}$$

where the penalty factor q is set to be 1. Secondly, for the MDI-D method, the design variable used in the ω penalization is shifted into the fluid domain as explained in Section 5.1. In this situation the specific dissipation rate penalization is shifted one element in the fluid domain and a blurring filter radius of twice the element size is used ($R = 2h$). Again equation 5.3 is used to determine the ω heaviside projection threshold. In this case with the given blurring filter radius and shifting distance the equation can be simplified to,

$$\gamma_f(x) = \gamma_c(x) + \frac{e^{\frac{1}{2}}}{2}(1 - \gamma_c(x)) - \frac{e^{-\frac{1}{2}}}{2}\gamma_c(x). \tag{6.6}$$

Here $\gamma_c(x)$ correspond to the control design variable. Assuming that the control design variable has a value 1 at the fluid/solid interface the γ_f is estimated to be 0.70. This means that the η_ω has to be equal to 0.70 to shift the specific dissipation rate one element in this problem. This threshold is different as in Sections 5.1 and 5.3 since we use a different blurring filter size $R = 2h$ instead of $R = h$. The maximum impermeability and ω projection threshold for the Dilgen method and the MDI-D method are summarized in Table 6.2.

Table 6.2: Variable settings for the Dilgen method and the MDI-D method.

Variable	Dilgen method	MDI-D method
$\overline{\alpha}$	10 000 1/s	59 055 1/s
η_ω	0.50	0.70

6.1.1. Topology Optimization results: Pressure drop minimization

First, the optimized geometries for both methods are shown in Figure 6.2. It can be seen that both methods are successful in generating a fairly straight channel which should minimize the pressure drop. The MDI-D method generated a channel which could be considered as perfectly straight, while the Dilgen design narrows at the beginning of the channel and widens near the end. As a consequence the Dilgen design shows small velocity fluctuations through the channel whereas in the MDI-D design the velocity distribution is more constant along the channel length, as can be seen in Figure 6.3.

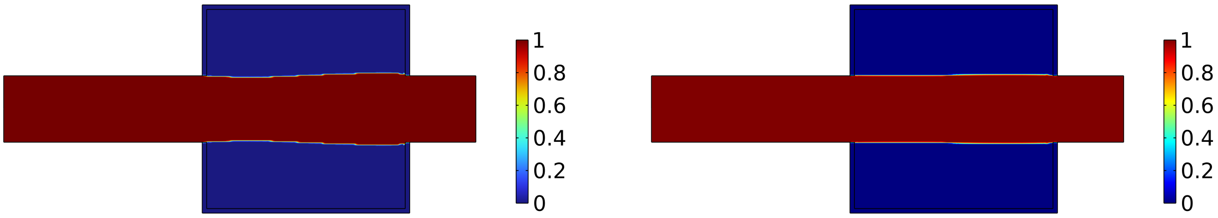

(a) Density distribution with the Dilgen method. $C = 0.468$.

(b) Density distribution with the MDI-D method $C = 0.350$.

Figure 6.2: Density distribution of the optimized designs.

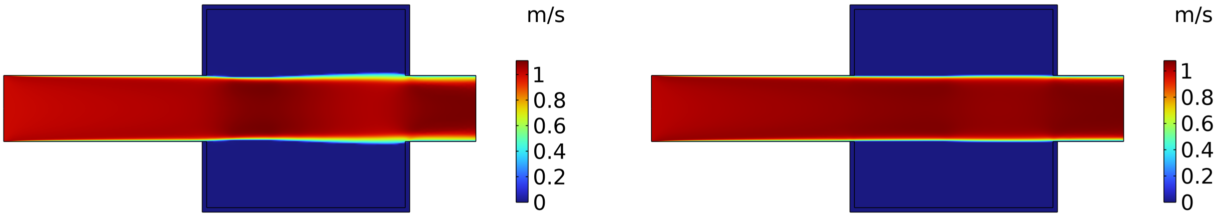

(a) Velocity magnitude with the Dilgen method.

(b) Velocity magnitude with the MDI-D method.

Figure 6.3: Velocity magnitude of the optimized designs.

6.1.2. Post-processing of the Topology Optimization results

Important for TO is the post-processing step in which the density distribution output is used to define a discrete geometry with distinct solid and fluid domains, such that the optimized design can be verified in a verification model. In this case the threshold for the design variable (γ) is set to 0.5 which means that the solid and fluid domains are equally split, the result of this is shown in Figure 6.4. In the verification model a so called 'body fitted' mesh is used, this means that the mesh is refined towards the wall. The velocity magnitudes in the verification models are shown in Figure 6.5, where the same behavior is shown as in the density based model.

(a) Geometry for the verification of the Dilgen method.

(b) Geometry for verification of the MDI-D method.

Figure 6.4: Post-processed geometries for the verification simulation.

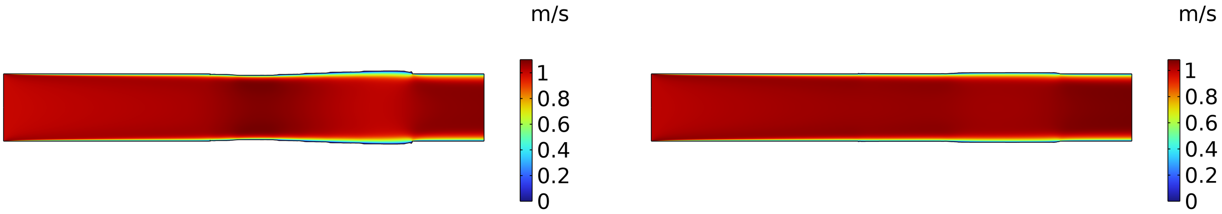

(a) Velocity magnitude with the Dilgen method.

(b) Velocity magnitude with the MDI-D method.

Figure 6.5: Velocity magnitude of the optimized designs.

The pressure drop objective for both the density-based designs as well as the post processed designs can be found in Table 6.3. The objective value given by the Dilgen method in the density model is higher than the actual pressure drop in the verification model. The Dilgen method has an error of 21.9% with respect to the verification model. The MDI-D method is significant more accurate when determining the objective value, as it only has an error of 6.2% with respect to the verification model. Finally, when comparing the objective values of both verification models, it is shown that the MDI-D method has found a geometry with a lower objective value. It can thus be concluded that in this case the MDI-D method outperforms the Dilgen method.

Table 6.3: Objective values for both methods with the Topology Optimization and verification case

	Dilgen method	**MDI-D method**
Density-based study	0.468	0.350
Verification study	0.384	0.373
Error	21.9%	6.2%

6.2. Pressure drop minimization around an internal wall

It is shown in the pressure drop minimization case that the Dilgen method and MDI-D method are both capable of generating a simple channel design. However, by adjusting the geometry we can investigate what the limits of the Dilgen method are. In Section 5.3 we have shown that the flow leakage with the MDI-D method can be reduced compared to the Dilgen method. Therefore we place an obstacle, in this case a wall, inside the optimization domain. The wall is placed orthogonal to the inlet so that the velocity is maximal when colliding with the wall, this should push the optimization to its limits. The geometry can be seen in Figure 6.6. Similar parameters and boundary conditions are applied as in Section 6.1, unless stated otherwise.

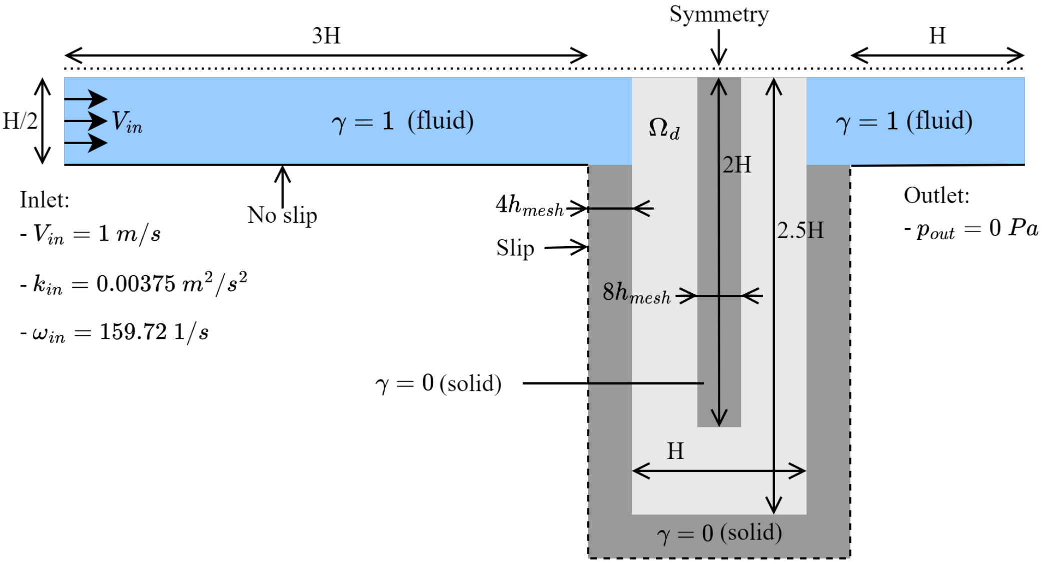

Figure 6.6: Geometry of the pressure drop minimization around an internal wall optimization.

A similar optimization problem as in Section 6.1 is evaluated, where the pressure drop over the channel is minimized:

$$\boxed{\begin{array}{lll} \underset{\gamma(\vec{x})}{\text{minimize}} & H = \dfrac{\overline{p}_{in} - \overline{p}_{out}}{p_{ref}} & \\ \text{subject to} & R\,(u(\vec{x}), \gamma(\vec{x})) = 0, & \vec{x} \in \Omega, \\ & \overline{\gamma}_{\Omega} \leq 0.8, & \end{array}} \tag{6.7}$$

The geometry in this optimization problem is changed and therefore a different p_{ref} is determined, again based on an initial simulation of the fluid through the open domain. This results in a reference pressure of $p_{ref} = 413.90\ Pa$ for the Dilgen method and $p_{ref} = 7372.04\ Pa$ for the MDI-D method. Secondly, penalization factor q in Equation 6.5 for the MDI-D method is increased to 2. This means the maximum impermeability is changed to $\overline{\alpha} = 590550\ 1/s$, which results in a significant difference between the impermeability for the Dilgen method and MDI-D method. This is also the reason why there is such a significant difference between the reference pressures. We found that the continuation scheme as presented in Section 6.1 is not suitable for this TO case. Therefore the continuation scheme in this case starts at $\beta = 2$ and increases to $\beta = 14$ with intermediate steps of 2. In Table 6.4 the parameters which are different to the previous optimization can be found.

Table 6.4: Pressure drop minimization around an internal wall specific variables for the Dilgen method and the MDI-D method. The Dilgen settings are chosen within the range presented by Dilgen et al. [2] and are chosen such that the most optimal settings for this case are used.

Variable	**Dilgen method**	**MDI-D method**
p_{ref}	413.90 Pa	7372.04 Pa
Da/q (respectively)	10^{-6}	2
$\overline{\alpha}$	$10\,000$ 1/s	$590\,550$ 1/s
β	2, 4, 6, 8, 10, 12, 14	

6.2.1. Topology Optimization results: Pressure drop minimization around an internal wall

In Figure 6.7 the optimal density distribution of the design variable γ is shown. The Dilgen design in Figure 6.7a shows that it is not able to generate a channel which connects the in- and outlet with each other. In Figure 6.7b the MDI-D design is shown, this design shows a generated channel around the inner wall. The obtained objective values for the Dilgen and MDI-D design are $H = 0.320$ and $H = 0.210$ respectively. The MDI-D method showed some instabilities when β is increased and did not converge for β values higher than 10, where the Dilgen method solved up to a β of 14. As presented in Section 5.3.2 this is already expected. However, even for lower projection slopes the MDI-D method is more accurate than the Dilgen method.

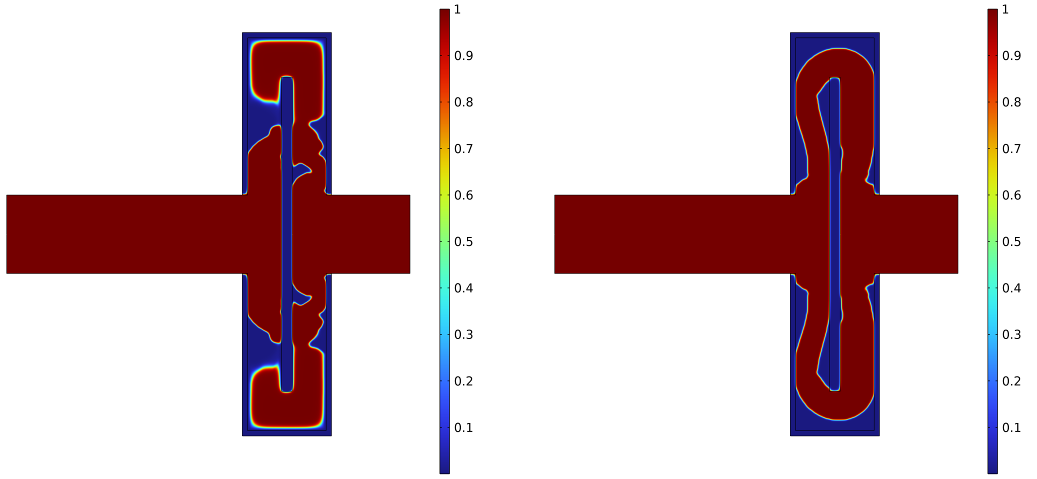

(a) Density distribution with the Dilgen method. $\beta = 14$ and $H = 0.320$.

(b) Density distribution with the MDI-D method. $\beta = 10$ and $H = 0.210$.

Figure 6.7: Density distribution of the optimized designs

In Figure 6.8 the velocity magnitudes of the Dilgen and MDI-D designs can be found. Since the Dilgen method did not generate a design where the in- and outlet are connected, the velocity had to find a way to come from in- to outlet. In the Dilgen design in Figure 6.8a it can been seen that the velocity goes straight through the inner wall. Apparently, the Dilgen method is not capable of penalizing the fluid enough to stop it from penetrating the wall. In Figure 6.8b the velocity magnitude in the MDI-D design is guided through the developed channel. However, inside the inner wall on the right side some light blue highlighted areas can be seen. So even though the MDI-D method generated a channel around the inner wall, some fluid still passes through the wall.

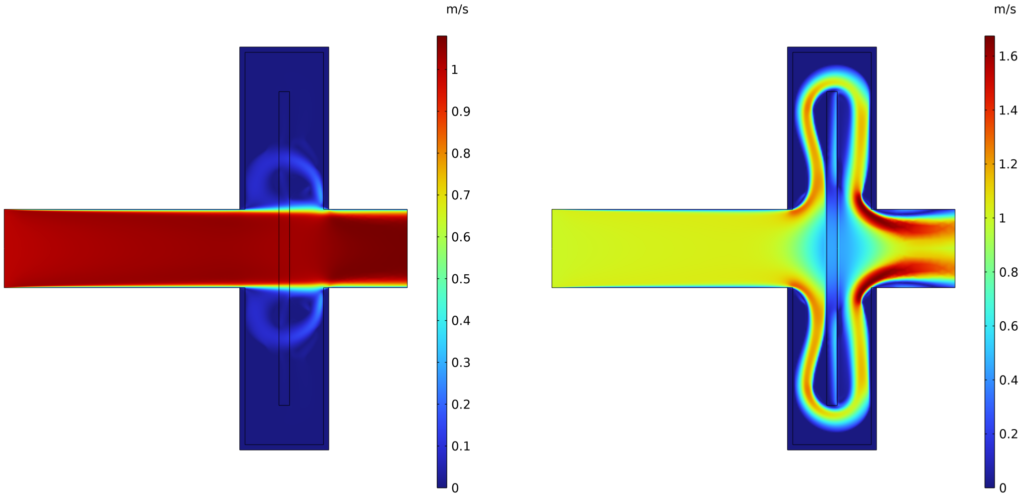

(a) Velocity magnitude with the Dilgen method (b) Velocity magnitude with the MDI-D method

Figure 6.8: Velocity magnitude of the optimized designs of the pressure drop minimization around an internal wall.

To gain more insight in the fluid passing through the inner wall, we first look at the flow leakage percentage as shown in Section 4.2. Here the amount of flow through the solid domain is divided by the total inlet flow. However, in this case we are interested in the flow passing through the internal wall. Therefore we use the amount of flow entering the internal wall on first contact, so at the left side of the internal wall. The flow entering the internal wall at the left side divided by the total inlet flow gives a percentage of how much flow is leaking through the wall relative to the amount of flow in the domain. The flow leakage through the internal wall is shown in Table 6.5 for both methods. As expected the flow leakage for the Dilgen method is around 100% since there is no channel generated in the Dilgen design and all flow is forced through the wall. In the MDI-D method the flow leakage is 50.7%, which is also too large and thus indicating the solid is not impermeably enough.

Table 6.5: Flow leakage through the internal wall for the Dilgen and MDI-D method.

	Dilgen method	**MDI-D method**
Flow leakage internal wall	99.9 %	50.7 %

Secondly, we are looking at the velocity magnitude on the cut line along the inner wall, as shown in Figure 6.9.

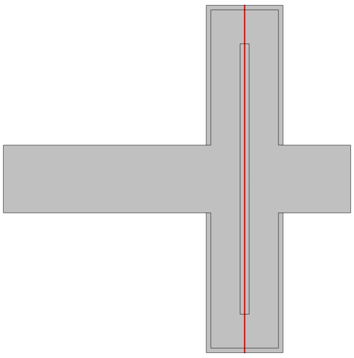

Figure 6.9: Location of the cut line through the design domain

The velocity magnitudes on the cut line are shown in Figure 6.10. We analyze the velocity on this cut line so that the fluid penetrating the inner wall can be investigated. First, the Dilgen design in Figure 6.10a shows that all the fluid is passing through the middle of the channel, which is as expected after evaluating the velocity magnitude on the full domain and the flow leakage. Some small peaks are shown on both sides of the large peak which is due to flow bounced off the outer wall and going back into the inner wall. The MDI-D design in Figure 6.8b shows that the highest velocities are reached in the upper and lower channel where $\gamma = 1$. However, just as in the Dilgen design, fluid is flowing through the inner wall, which is shown by the smaller peaks in the solid domain where $\gamma = 0$. This is also in accordance to our observations of the velocity magnitude in the full domain, where some velocity magnitudes are shown in the solid domain.

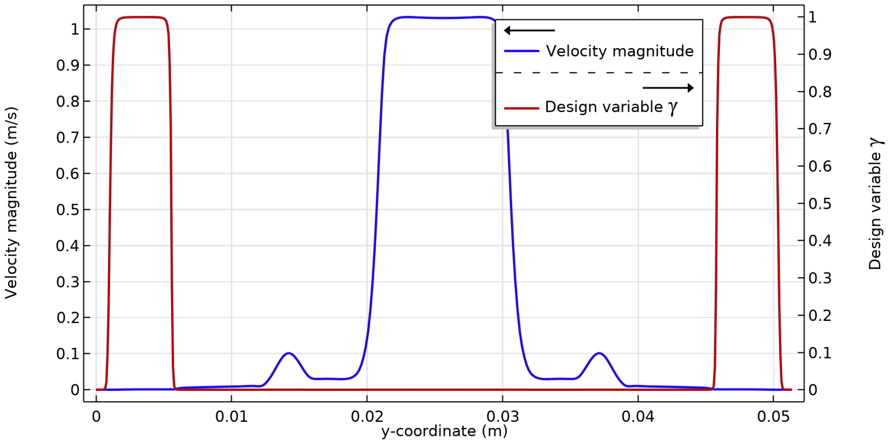

(a) Velocity magnitude on the cut line with the Dilgen method

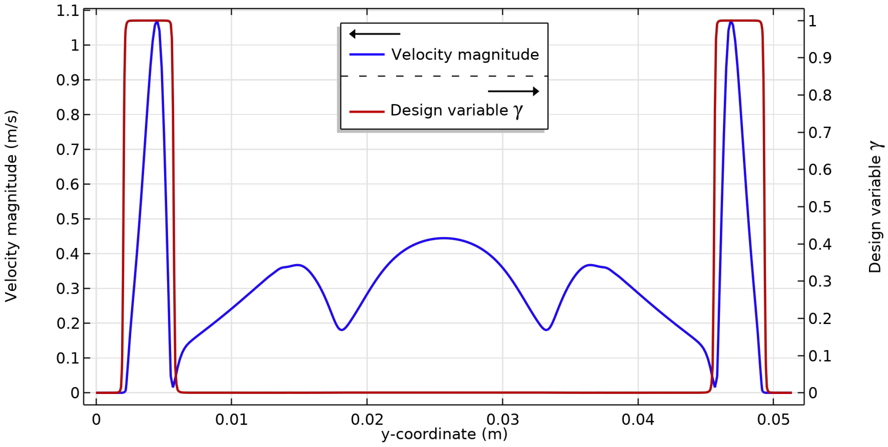

(b) Velocity magnitude on the cut line with the MDI-D method

Figure 6.10: Velocity magnitude on the cut line of the optimized designs of the pressure drop minimization around an internal wall case.

Convergence study

The Dilgen method is not capable of handling the high velocities passing through the thin wall. However, the Dilgen method shows a much more stable behavior when investigating the convergence of the model. The Dilgen method is able to converge up to a β of 14 within a reasonable timespan (1 to 2 hours for each continuation step), however the result is unusable since the flow in- and outlet are disconnected. The MDI-D method had more trouble converging. The first projection slope steps were no problem at all up to and including projection slope 8, where the computation times are still in the range of a few hours as shown in Table 6.6. After that, on projection slope 10, the model start to face issues. The computation time for $\beta = 10$ increased to 16 hours. The projection slopes of 12 and 14 did not even converge anymore for the MDI-D method, which indicates that this model is unstable for higher projection slopes in combination with the high penalizations. The Dilgen method is thus capable of reaching higher projection slopes. However in Section 5.3.2 is shown that even with lower projection slopes the MDI-D method is more accurate in reaching the ω_b target. The flow leakage for every projection slope is also given in Table 6.6. However, the flow leakage tends not to decrease with a higher projection slope. This is due the fact that the solid is modeled with a maximum impermeability which is not changing for different projection slopes. Both simulations have been performed on a cluster computer using all 192 available cores. In Appendix F the intermediate designs and the convergence plots can be found in respectively Section F.1 and Section F.2.

Table 6.6: Convergence data of the Dilgen topology optimization study

	Computation times (hh:mm:ss)		**Number of iterations**		**Objective values**		**Flow leakage**	
β	Dilgen	MDI-D	Dilgen	MDI-D	Dilgen	MDI-D	Dilgen	MDI-D
2	01:54:53	02:10:06	43	50	0.9859	1.0430	99.7 %	54.5 %
4	00:42:04	01:55:23	23	50	0.6795	0.6242	99.7 %	49.9 %
6	01:02:56	02:56:57	37	50	0.5086	0.4026	99.7 %	50.1 %
8	01:28:14	01:34:30	50	26	0.4219	0.2702	99.7 %	49.9 %
10	01:31:00	16:28:40	50	50	0.3732	0.2098	99.8 %	50.7 %
12	01:42:37	-	50	-	0.3423	-	99.8 %	-
14	01:50:48	-	50	-	0.3202	-	99.9 %	-

6.2.2. Post-processing of the Topology Optimization results

The post-processed designs can be found in Figure 6.11. Similar to the post-processing step in the pressure drop minimization optimization in Section 6.1, a threshold of 0.5 is used on the density design variable to split the solid and fluid domain. As can be seen in Figure 6.11a, the Dilgen design did not generate a design in which the in- and outlet are connected. In a verification study the in- and outlet must be connected and therefore no verification study could be performed on the Dilgen design.

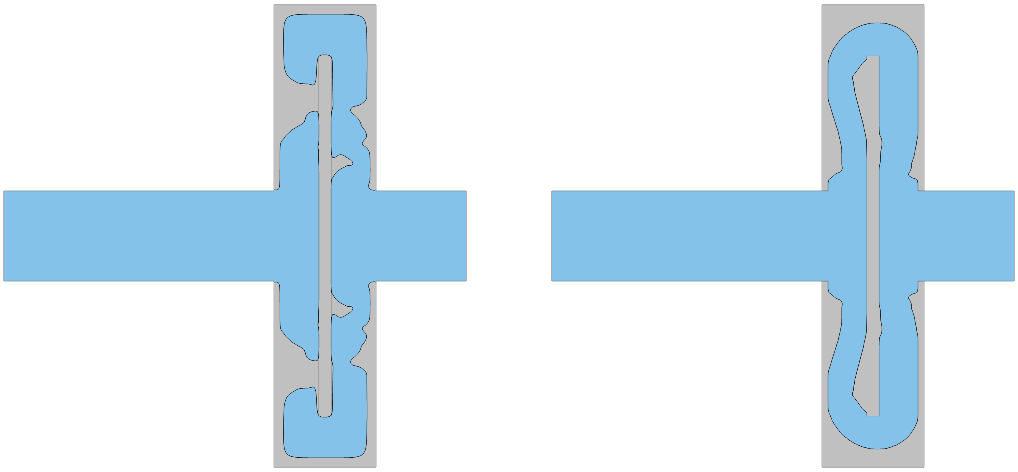

(a) Post-processed geometry of the Dilgen method

(b) Post-processed geometry of the MDI-D method

Figure 6.11: Post-processed geometries for the verification studies

The velocity magnitude in the verification study of the MDI-D design is shown in Figure 6.12. Here it is shown that maximum velocities are higher than in the density-based models, where it is 1.6 m/s for both the density-based study in Figure 6.8b and 2.5 m/s in the verification study. This is confirmed by analyzing the cut line in Figure 6.13, here the velocity magnitude for the density-based study as for the verification study are shown. The velocity magnitude in the fluid domain where $\gamma = 1$, is more than twice as high in the verification study compared to the density-based study. Due to the flow leakage through the inner wall in the density-based study, the velocity magnitude is reduced in the fluid domain.

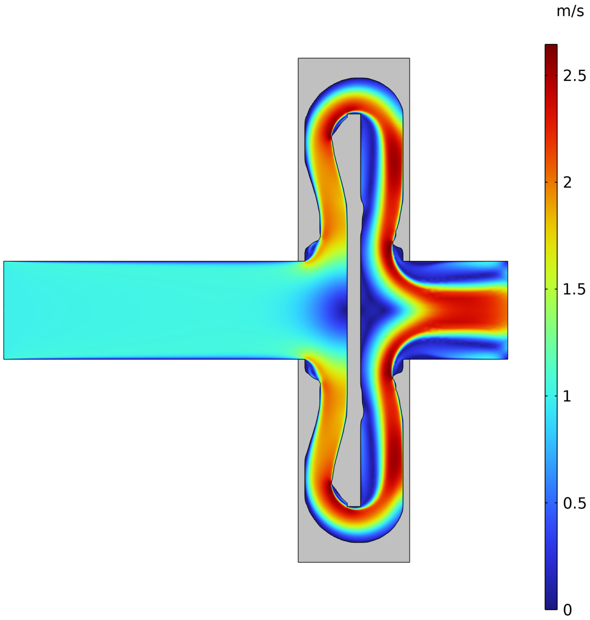

Figure 6.12: Velocity magnitude of the MDI-D design in the verification study.

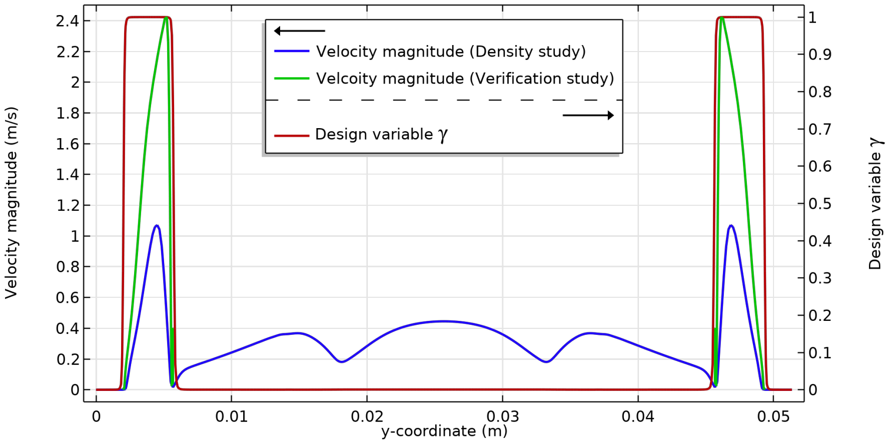

Figure 6.13: Velocity magnitude of the MDI-D method with the density-based study and the verification study, the design variable γ is included as well.

Finally, the objective values are shown in Table 6.7. Since no verification study of the Dilgen design was possible, the objective values are logically not available for this case. The objective values for the MDI-D design are shown for both the density-based study as for the verification study. The density-based study shows a lower objective value compared to the verification model. This is likely due to the flow leakage through the inner wall in the density-based study. If the fluid flows through the inner wall, the pressure build up in the domain is lower and therefore the pressure drop is reduced as well.

Table 6.7: Objective values for both the Dilgen and MDI-D method with the Topology Optimization and verification case

	Dilgen method	**MDI-D method**
Density-based study	0.320	0.210
Verification study	-	0.473
Error	-	55.60%

6.2.3. Discussion on the pressure drop minimization around an internal wall optimization

The MDI-D method shows a significant improvement when compared to the Dilgen method in this optimization problem. The Dilgen method is not capable of generating a design in which the fluid is guided around the inner wall, instead the fluid flows straight through the inner wall. On the contrary, the MDI-D method does develop a channel around the inner wall. The difference between both results is caused by the higher impermeability in the MDI-D method which results in a higher penalization in the solid domains where $\gamma = 0$. The higher penalization causes the fluid to stop in the solid domains. However, as shown on the cut lines of the MDI-D design in Figure 6.10b, there is still too much flow leakage through the inner wall. It can thus be concluded that the solid domain, where $\gamma = 0$, is still not impermeable enough to stop the fluid from flowing through the wall. This can also be seen in the large difference in objective values in Table 6.7. Therefore, a simple solution could be increasing the maximum impermeability by increasing q in Equation 6.5. However, a simulation performed with $q = 3$ resulted in a highly unstable model. After 74 hours the simulation was forced to stop since it was still in the first projection slope step of $\beta = 2$. This indicates that the MDI-D method performs at its maximum capability before it becomes real unstable.

7

Conclusion and recommendations

First in Section 7.1 a discussion regarding the developed method is presented. Secondly, in Section 7.2 some recommendations for further research are given.

7.1. Conclusion

This research is focused on answering the question: ***'Can an accurate method for density-based Topology Optimization of turbulent flows be constructed, which uses the $k - \omega$ turbulence model?'***. Before a new method regarding the Topology Optimization of turbulent flows is developed, the state-of-the-art is investigated in Chapter 4. In this chapter weaknesses regarding the Dilgen method are exposed. An important point of attention in the Dilgen method is that the boundary conditions which are imposed at the wall are not accomplished. In Chapter 5, improvements on the Dilgen method regarding the Topology Optimization of turbulent flows are developed. One of the boundary conditions at a wall, which is not met using the Dilgen approach, is the infinite amount of specific dissipation rate. Although an infinite amount of specific dissipation rate is not achievable, the Dilgen method tries to force it as high as possible. In the investigation of the Dilgen method it is found that the specific dissipation rate is still increasing when already beyond the wall and in the solid region. Therefore, it is decided to shift the specific dissipation rate penalty of the Dilgen method into the fluid domain, which is the first improvement resulting in the dilation method in Section 5.1. Shifting the penalty of the specific dissipation rate into the fluid domain results in the ω penalty already being active before reaching the wall. Now the specific dissipation rate penalty is active before reaching the wall, higher values for the specific dissipation rate are reached when approaching the wall. The dilation of the specific dissipation rate also influences the velocities at the wall, which tend to zero quicker, allowing the velocity to meet the boundary condition for zero velocity at the wall. However, the Dilation method introduces some unwanted behavior of the velocity on a short distance from the solid/fluid interface in the fluid domain. This is caused by the specific dissipation rate penalties being active inside the fluid domain. Also the turbulent kinetic energy is influenced by the specific dissipation rate and is therefore too low in the fluid domain close to the wall. Concluding, the Dilation method provides some improvements on achieving the boundary conditions but it can not be labeled as perfect yet.

The Dilation method is extended with the so called MDI method. In this method the impermeability, which is a value for the porosity of the solids, is dependent on the mesh size. This MDI method accounts for the solid regions to be porous enough and penalize the fluid velocity as desired, so that it forces the fluid to stop. The combination of the Dilation and MDI method, the MDI-D method, shows great improvements on the density model in Section 5.3. Here the boundary conditions at the wall are still achieved, the flow properties like velocity and turbulent kinetic energy are less influenced further away from the wall as is the case in the Dilation method. However, to be able to conclude that this method is an improvement for the Topology Optimization of turbulent flows, a TO case is performed.

In Chapter 6 several cases regarding the TO of turbulent flows are presented. The first TO case is a simple pressure drop channel, proving the functionality of the MDI-D method. The functionality of the MDI-D method is proven and besides that the results of the MDI-D design are even better than the Dilgen design. The MDI-D design generated a channel with less pressure drop compared to the Dilgen design. Secondly, the objective error between the density based model and the verification model is only 6.2% using the MDI-D method which is significantly better compared to the Dilgen design with an error of 21.9%.

After the functionality test the Dilgen and MDI-D method are exposed to a more extreme case. In Section 6.2 both methods are pushed to its limits where an optimization problem is evaluated with a flow around an internal wall. The improvements of the MDI-D method are really shown in this optimization problem. The MDI-D method generates a design which guides the flow around the internal wall, where the Dilgen method pushes the fluid through the internal wall. However, even though the MDI-D method found a feasible design, there is still a significant amount of fluid forced through te inner wall, meaning the impermeability of the solid domains is not high enough. Increasing the penalty factor

q in the MDI-D method is tested but did not give the desired result as the model became instable and did not solve. So it can be concluded that a weakness of the MDI-D method is the stability of the model, especially when using higher penalty factors or higher projection slopes as shown in the convergence data (Table 6.6).

Finally, answering the proposed research question ***'Can an accurate method for density-based Topology Optimization of turbulent flows be constructed, which uses the $k - \omega$ turbulence model?'***. The MDI-D method shows improvements and has a better performance regarding the accuracy when compared to the Dilgen method. Especially in the second optimization case a significant improvement is shown with the MDI-D method, since it developed a feasible design. However, the accuracy between the density-based and verification model is still quite low for the MDI-D method with an objective error of 55.60%, mainly caused by the flow leakage through the inner wall. Secondly, regarding the stability of the MDI-D method, it shows worse results when compared to the Dilgen method. Considering this, the MDI-D method could still be valuable in the research area of the Topology Optimization of turbulent flows. However, a user must take into consideration if the stability or the accuracy of the model is more important. If the accuracy and a more optimized model is the most important, then the MDI-D method could be beneficial.

7.2. Recommendations

Although the research shows promising results, there are still some improvements that can be made. Therefore in this final section some recommendations for further research are proposed.

- **Decrease flow leakage:** One of the major remaining issues of the MDI-D method is the flow leakage through the solid domains. Although it is already reduced compared to the Dilgen method it is still not completely solved. Increasing the impermeability is limited since the simulation becomes unstable. Therefore, it is important to accurately determine the maximum allowable impermeability so that the simulation can be pushed to its limit.

- **Improve the stability of the MDI-D method:** In the second TO case it is shown that the MDI-D method is unstable for higher projection slopes and higher impermeabilities. However, in Section 5.3 is shown that the MDI-D method did run for a projection slope $\beta = 80$ for the specific dissipation rate only. At the moment the projection slopes for all the turbulent fields was increased the MDI-D method became unstable as shown in Section 5.3.2. Apparently, the high projection slopes for the *Darcy-* and *k-penalization* introduce more instabilities. Therefore, it might be interesting to research different continuation schemes where the projection slopes for the velocity and turbulent kinetic energy are limited to a certain value.

- **Improve heat transfer accuracy:** In Appendix B.3 a step towards the TO of turbulent flow cooling devices is made. However, one of the main issues in the Topology Optimization cases is the accuracy of the heat transfer in the density model when compared to the verification model. Both, the Dilgen method as the MDI-D method showed significant errors in the density-based models after verification. A more elaborated research on a fixed geometry has to be performed so that the weaknesses in the thermo-fluid case can be discovered. Since the MDI-D method still showed some flow leakage through the solid domains the convective heat transport is likely to be overestimated. Therefore, it might be interesting to research the possibilities for new penalty methods to reduce the convective heat transfer. Penalty methods are already applied to the convective heat transfer part of the equation. However, these are clearly not strong enough to stop the convective heat transfer in the solid domains.

- **Extending the MDI-D method to different turbulence models:** In this work the MDI-D method is only restricted to the $k - \omega$ model. However, a similar method might be used in other turbulence models as well, for example the $k - \varepsilon$ model. Other turbulence models might be even more powerful when combined with the developed MDI-D method.

- **Three-dimensional Topology Optimization:** The Topology Optimization of turbulent-flow in this work is limited to two-dimensional flows only. Research focused on the development of three-dimensional cooling devices could be interesting. However, the computation time is the restricting factor in optimizing three-dimensional models. Therefore, the computation time must be reduced first before an extension to three-dimensional flows can be performed.

Acronyms

AC alternating current. 2
AD Automatic Differentiation. 5, 6

CFD Computational Fluid Dynamics. 5, 8–11, 15, 49, 74

DC direct current. 2
Dilgen WD Dilgen wall distance approach. 28, 90–94
DNS Direct Numerical Simulation. 8

F-D Forchheimer with dilation. 98–102
FEM Finite Element Method. ii, 7

HJ Hamilton-Jacobi. 4

LSF Level-Set Function. 4

MDI Mesh dependent impermeability. 28, 35–41, 43, 48, 60, 81–84, 89
MDI-D Mesh dependent impermeability with dilation. 28, 41–49, 51–61, 70–76, 84–87, 89, 103, 105, 106
MMA Method of Moving Asymptotes. 4, 5

N-S Navier-Stokes. 8, 12

PDE Partial Differential Equation. 7, 9, 14, 22, 24, 50
PT Prodrive Technologies. 1–3, 5, 64

RANS Reynolds-averaged Navier-Stokes. 7, 8, 13, 35, 50
RRMSE Relative Root Mean Square Error. 21, 23, 25, 26, 31–36, 39–42, 48, 70, 88, 93

Si Silicon. 1, 2
SiC Silicon Carbide. 1–3
SiC MOSFETs Silicon Carbide metal-oxide-semicondutor field-effect transistors. 1, 2

TO Topology Optimization. 1, 3–7, 12–17, 24, 27, 46, 48–53, 58, 60, 61, 68, 69, 74, 76, 103, 106

Appendices

A

Previous performed research at Prodrive Technologies

Unfortunately this appendix contains confidential information which belongs to Prodrive Technologies and can therefore not be made public.

B

Topology optimization of a turbulent-flow cooling device

In this appendix the Topology Optimization of a turbulent-flow cooling device is discussed. In Section B.1 the required background information for thermal convection-diffusion in TO is presented. Secondly, in Section B.2 the heat transfer physics are applied to the fixed bent channel geometry. Finally, in Section B.3 a first step is made in direction of the Topology Optimization of a turbulent-flow cooling device.

B.1. Thermal convection-diffusion for Topology optimization

The heat transfer in situations where fluids and solids are combined is known as conjugate heat transfer, which is described by two different types of heat transfer. First the convective heat transfer, this type of heat transfer is due to the transportation of heat by movement of the fluid. Secondly, conductive heat transfer which is the transfer of heat from the hotter region to the colder region through the interaction of the molecules. In the solid region only conductive heat transfer should be present since there is no movement of any fluid. In fluid domains both the convective heat transfer and conductive heat transfer is active. Combining the convective and conductive heat transfer results in the conjugate heat equation [42],

$$\underbrace{\rho C_p \vec{u} \cdot \nabla T}_{\text{Convective heat transfer}} - \underbrace{\nabla \cdot \kappa \nabla T}_{\text{Conductive heat transfer}} = Q, \tag{B.1}$$

where ρ is the density in $\mathrm{kg/m^3}$, C_p is the thermal capacity of the material in $\mathrm{J/(kg\,K)}$, $\vec{u}$ the velocity field in $\mathrm{m/s}$, T the temperature in K, κ the thermal conductivity in $\mathrm{W/(m\,K)}$ and Q the heat source in $\mathrm{W/m^3}$. In a turbulent regime, the flow properties are affected by the turbulence, this means that the thermal conductivity is different in the turbulent regime. Therefore the thermal conductivity in the conductive heat transfer part of the conjugate heat transfer is replaced by the effective thermal conductivity. The thermal conductivity is a combination of the material thermal conductivity (κ) and the turbulent thermal conductivity (κ_T), as shown below,

$$\kappa_{\text{eff}} = \kappa + \kappa_T, \tag{B.2}$$

where the turbulent thermal conductivity κ_T is:

$$\kappa_T = \frac{\mu_T C_p}{Pr_T}, \tag{B.3}$$

here Pr_T is the turbulent Prandtl number which is dependent on the chosen heat transport turbulence model in COMSOL Multiphysics [12]. If the default *Kays-Crawford* approximation is used the turbulent Prandtl number is defined as:

$$Pr_T = \left(\frac{1}{2Pr_{T\infty}} + \frac{0.3}{\sqrt{Pr_{T\infty}}} \frac{C_p \mu_T}{\lambda} - \left(0.3 \frac{C_p \mu_T}{\lambda} \right)^2 \left(1 - e^{-\lambda / \left(0.3 C_p \mu_T \sqrt{Pr_{T\infty}} \right)} \right) \right)^{-1}, \tag{B.4}$$

where $Pr_{T\infty} = 0.85$ is the turbulent Prandtl number at infinity and λ is the conductivity. The thermal conductivity thus increases by the turbulent thermal conductivity, in that case the conductive heat transfer is increased as well resulting in a higher cooling performance. Since the turbulent thermal conductivity κ_T is dependent on the turbulent dynamic viscosity μ_T the conductive heat transfer thus increases in regions where a lot of turbulent kinetic energy is present according to Equation 3.11.

Adapting the heat transfer model for the topology optimization of turbulent-flow cooling systems

As explained the density variable vary throughout the domain from 0 to 1 and thus the thermal material properties have to be interpolated as well, so that the intermediate values have the corresponding material properties. The material properties used in the heat transfer equations are interpolated using a SIMP interpolation [43]. The material properties regarding the solid material are denoted by a subscript s and the material properties of the fluid material are denoted with a subscript f. The interpolations for the thermal conductivity κ, the specific heat capacities C_p and the density ρ are:

$$\kappa(\gamma) = \kappa_f + (\kappa_s - \kappa_f)\gamma^n, \tag{B.5}$$

$$C_p(\gamma) = C_f + (C_s - C_f)\gamma^n, \tag{B.6}$$

$$\rho(\gamma) = \rho_f + (\rho_s - \rho_f)\gamma^n, \tag{B.7}$$

with n as penalization factor with normally small integer values as 1, 2, 3 and 4. Again, the penalty factor can be used to develop a sharper interpolation function as shown in Figure B.1.

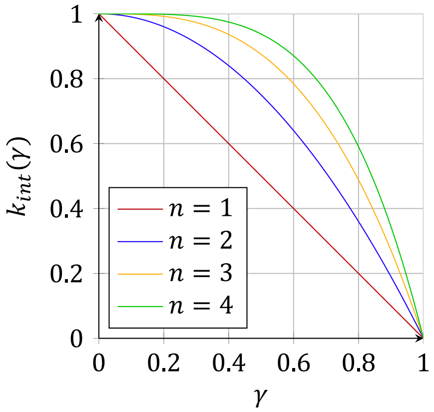

Figure B.1: SIMP interpolation with different penalization factors, where $k_{int}(\gamma)$ represents the interpolated variable.

In the work by Dilgen et al. [10] it is noticed that the convective heat transfer remains large in the solid regions. Therefore, they introduced an additional penalty on the convective heat transfer in the conjugate heat transfer equation. The penalty is dependent on the design variable and pushes the convective heat transfer towards zero in the solid domain. Combining all the related heat transfer aspects in TO leads to the final equation,

$$\underbrace{\chi(\gamma)\rho(\gamma)C_p(\gamma)\vec{u}\cdot\nabla T}_{\text{Convective heat transfer}} - \underbrace{\nabla\cdot\kappa_{\text{eff}}(\gamma)\nabla T}_{\text{Conductive heat transfer}} = Q, \tag{B.8}$$

where $\chi(\gamma)$ is the additional penalty for the convective heat transfer defined as,

$$\chi(\gamma) = \gamma(\gamma)^n. \tag{B.9}$$

B.2. Applying heat transfer on the bendchannel geometry with the MDI-D method

In this section the bent channel problem is evaluated again, however in this case a heat source is introduced. In Figure B.2 the geometry including the heat source Q can be seen. The heat source has a power of 1000 W.

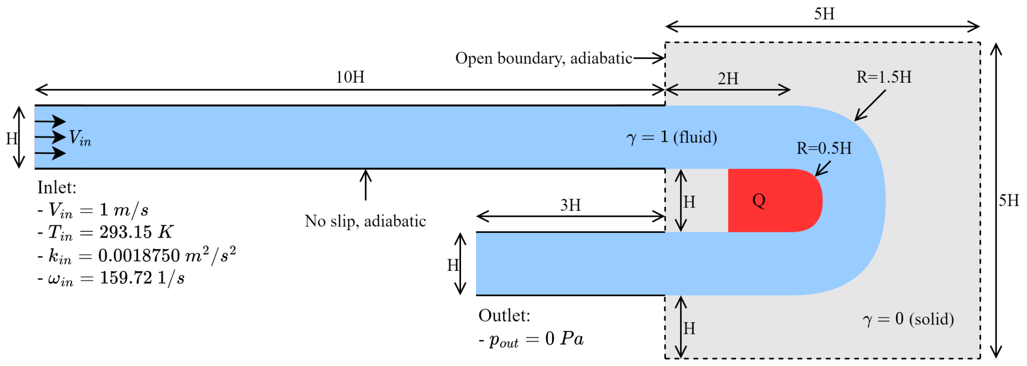

Figure B.2: Geometry bendchannel case with heat transfer

The temperature difference RRMSE is defined as:

$$\text{RRMSE}\Delta T = \sqrt{\frac{\frac{1}{n}\sum_{i=1}^{n}((T_i - T_{in}) - (\hat{T}_i - T_{in}))^2}{\sum_{i=1}^{n}(\hat{T}_i - T_{in})^2}} \cdot 100 = \sqrt{\frac{\frac{1}{n}\sum_{i=1}^{n}(T_i - \hat{T}_i)^2}{\sum_{i=1}^{n}(\hat{T}_i - T_{in})^2}} \cdot 100 \tag{B.10}$$

In Table B.1 the temperature difference RRMSE are shown. The MDI-D method showed overall the largest errors with an error difference of around 20% compared to the Dilgen method. Only the Dilgen with reference h_{10} case has a lower error. The lower errors for the MDI-D case are a result of the higher impermeability in the MDI-D method. Due to the higher impermeability the fluid velocity in the solid domain is reduced and thus also the convectional heat transfer. However, the errors are still significant and thus more research is required for obtaining accurate fluid flow in heat transfer in the density-based method.

Table B.1: RRMSE of the average temperature distribution with the MDI-D method.

		MDI-D method	**Dilgen method**
w.r.t.	h_x	**RRMSE ΔT**	**RRMSE ΔT**
reference best case	h_5	65.1 %	85.0 %
	h_{10}	66.8 %	86.4 %
reference h_x case	h_5	49.0 %	77.3 %
	h_{10}	66.5 %	35.8 %

B.3. Topology optimization of a turbulent-flow cooling system with heat source

In this section the pressure drop minimization problem shown in Section 6.1 is updated to a model where heat transfer is included. A square heat source (Q) is placed inside the optimization domain, which can be seen in Figure B.3. The heat load of the heat source is 20 000 W. The heat source has a fixed $\gamma = 0$, which means that it remains solid during the optimization. Since we consider heat transfer in this case the inlet temperature is given as well which is 293.15K. All outer walls are adiabatic, thus there is no heat transfer across the outer walls.

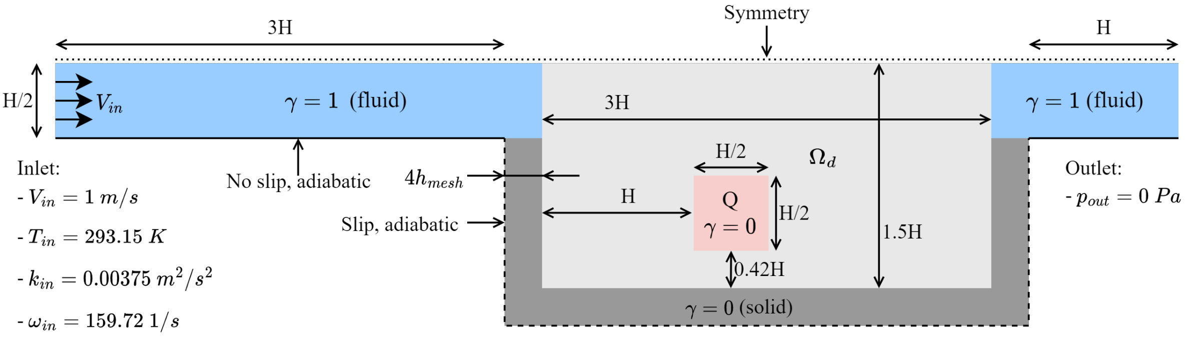

Figure B.3: Geometry topology optimization with heat transfer

The objective in this case is a combined objective with minimizing the temperature in the heat source while also maintaining a low pressure drop. The optimization problem with the corresponding constraints is defined below,

$$\boxed{\begin{aligned} &\underset{\gamma(\vec{x})}{\text{minimize}} && H = w_1 H_{pres} + w_2 H_T = w_1 \frac{\overline{p}_{in} - \overline{p}_{out}}{p_{ref}} + w_2 \frac{\overline{T}_{heatsource} - T_{in}}{T_{ref}} \\ &\text{subject to} && R\,(u(\vec{x}), \gamma(\vec{x})) = 0, \qquad \vec{x} \in \Omega, \\ & && \overline{\gamma}_{\Omega} \le 0.7, \end{aligned}} \tag{B.11}$$

The weight factors w_1 and w_2 can be used to prioritize one of the objectives. As we scale both objectives to be around 1 using p_{ref} and T_{ref} and do not intend to favor one objective over the other we set both weight factors to $w_1 = w_2 = 0.5$. To determine the correct scale factors such that both objectives are scaled to 1 an initial simulation is run on the open domain and from there the reference pressure and temperature are calculated respectively as,

$$p_{ref} = \overline{p}_{in} - \overline{p}_{out}, \tag{B.12}$$

$$T_{ref} = \overline{T}_{heatsource} - T_{in}. \tag{B.13}$$

The Dilgen method and the Mesh dependent impermeability with dilation method have different reference values. This is due to the fact that the initial simulation does include the different maximum impermeabilities and the dilation. Although there is no optimization in this initial simulation, the heat source and walls have a fixed density variable of zero which are still influencing the results. The values for the reference pressure and temperature can be found in Table B.2.

Table B.2: Reference pressure and temperature for the Dilgen and MDI-D method

Parameter	**Dilgen method**	**MDI-D method**
p_{ref} (Eq. B.12)	185.27 Pa	227.87 Pa
T_{ref} (Eq. B.13)	34.42 K	57.55 K

B.3.1. Topology optimization results: Turbulent-flow cooling system

First, the obtained geometries for both approaches are discussed. The optimized designs can be found in Figure B.4 and it can be seen that both approaches lead to distinct optimal geometries. The Dilgen method (Figure B.4a) has developed smaller channels directly around the heat source so that the fluid can transport the heat away from the heat source. The MDI-D method (Figure B.4b) creates large fluid basins near the heat source but also attaches a large solid block of material to the heat source.

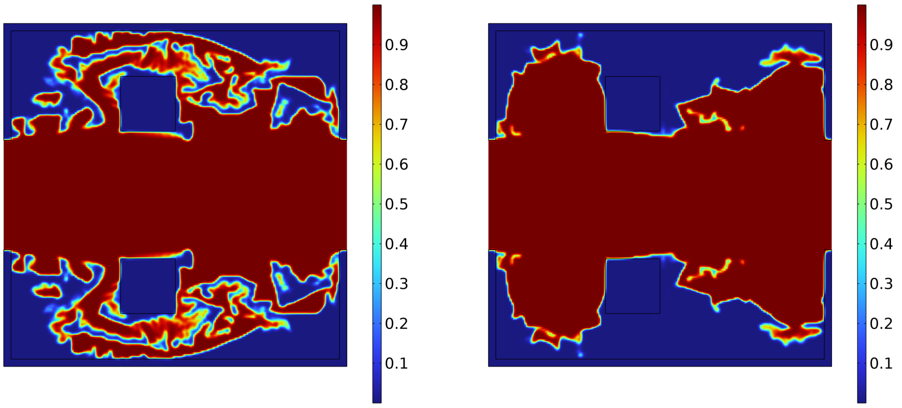

(a) Density distribution with the Dilgen method. $\beta = 14$ and $H = 0.626$.

(b) Density distribution with the MDI-D method. $\beta = 14$ and $H = 0.538$.

Figure B.4: Density distribution of the optimized designs for the Dilgen method and the MDI-D method.

The velocity magnitudes in the optimized domain are shown in Figures B.5a and B.5b for the Dilgen and MDI-D method respectively. No large velocities are present in the solid domain, especially in the heat source the flow is reduced to nearly zero. The turbulence in the domain is important to analyze since the turbulence should also increase the heat transfer, therefore we look at the turbulence intensity. The relative turbulence intensity is described by the following equation (Wilcox [44]),

$$I = 100\frac{\sqrt{\frac{2}{3}k}}{V_{in}} \tag{B.14}$$

where k is the turbulent kinetic energy in $\mathrm{m}^2/\mathrm{s}^2$ and V_{in} is the inlet velocity in $\mathrm{m/s}$. The relative turbulence intensity I is in percentages. According to [45], the turbulence intensity gives an indication about turbulence case in a flow. The scaling can be categorized as follows,

1. **High-turbulence case:** The turbulence intensity is between 5% and 20%.
2. **Medium-turbulence case:** The turbulence intensity is between 1% and 5%.
3. **Low-turbulence case:** The turbulence intensity is below 1%.

In Figures B.5c and B.5d the turbulence intensity with the Dilgen and Mesh dependent impermeability with dilation method is plotted respectively. A white contour line is plotted at a turbulent intensity of 5% to highlight transition between the Medium-turbulent and the High-turbulent region. Both methods shows a High-turbulent regime parallel to the free stream. The Dilgen method created a higher turbulent area at the beginning of the branches. The MDI-D method developed a high turbulent area in a part of the two circular flow basins.

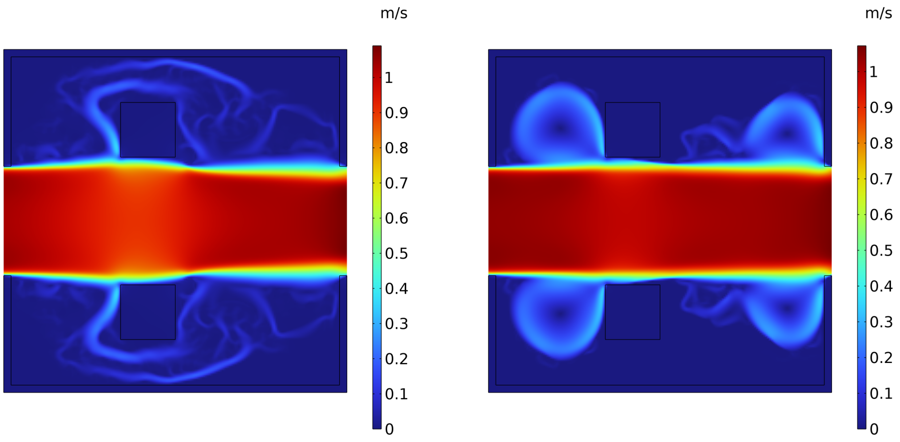

(a) Velocity magnitude with the Dilgen method

(b) Velocity magnitude with the MDI-D method

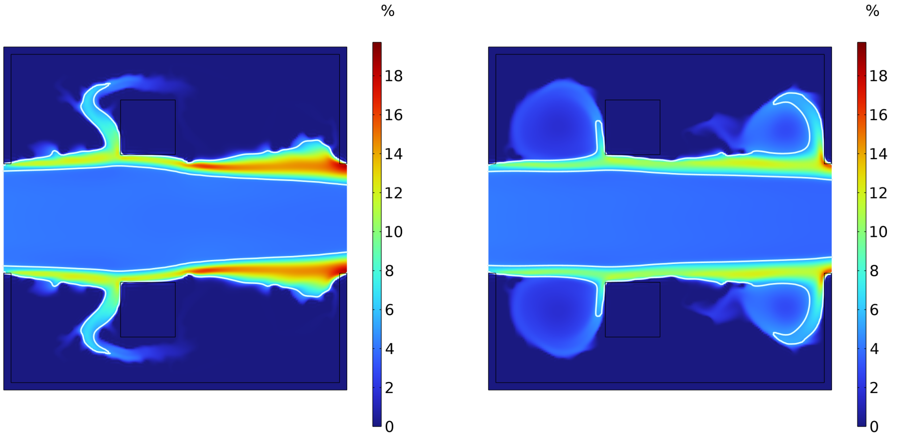

(c) Turbulence intensity with the Dilgen method. Contour is plotted in white at $I = 5\%$

(d) Turbulence intensity with the MDI-D method. Contour is plotted in white at $I = 5\%$

Figure B.5: Flow properties of the optimized designs

The temperature distribution of both models is presented in Figure B.6. Due to the identical temperature scale it can be seen in Figure B.6a that the temperature in the heat source of the Dilgen design is lower compared to the temperature in the MDI-D design as shown in Figure B.6b. Within the density-based framework, this indicates that the Dilgen method generated a better geometry when considering the cooling performance. In Figures B.6c and B.6d the convective heat flux:

$$q_{conv}(\gamma) = \chi(\gamma)\rho(\gamma)C_p(\gamma)\vec{u}\nabla T, \tag{B.15}$$

for the Dilgen method and MDI-D method are shown respectively. It can be seen that some convective heat flux remains in parts of the solid domain where the design variable is lower than 0.5. In the Dilgen method, convective heat flux in the solid domain remains significant, especially in the solid parts between the small channels. The average of the convective heat flux in the solid domain is $2351.7\mathrm{W}^2/\mathrm{m}$ and $343.14\mathrm{W}^2/\mathrm{m}$ for the Dilgen method and MDI-D method respectively. The convective heat flux should be zero in these domains and this indicates that both models overestimate the conductive heat flux in the solid domain. However, the Dilgen method overestimates the convective heat flux in the solid domain an order higher than the MDI-D method, which could be an explanation for the lower temperature inside the heat source for the Dilgen method. The lower overestimation of the convective heat flux in the MDI-D design could explain the solid domain generated around the heat source which is used to increase conductive heat flux out of the heat source.

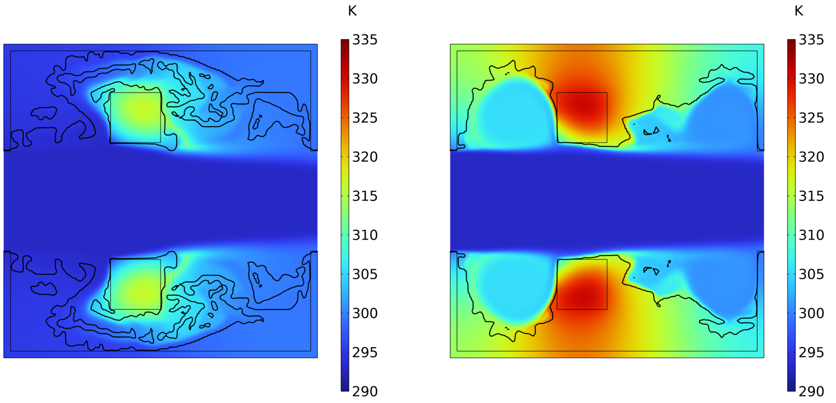

(a) Temperature distribution with the Dilgen method

(b) Temperature distribution with the MDI-D method

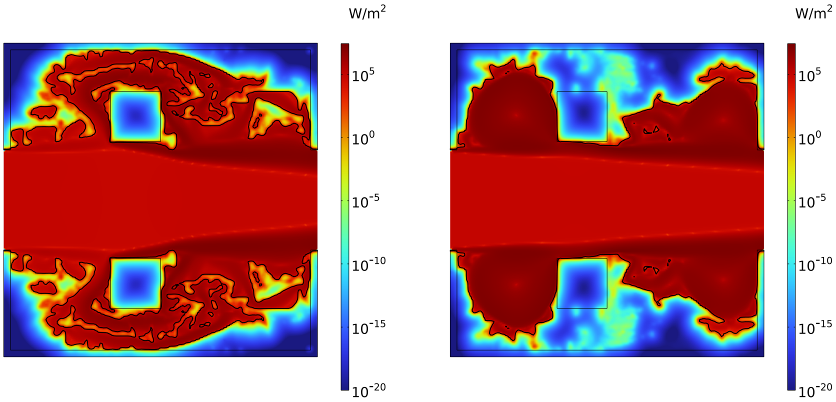

(c) Convective heat flux with the Dilgen method

(d) Convective heat flux with the MDI-D method

Figure B.6: Heat transfer related variables in the optimized designs. A design variable contour is plotted in black at a value of 0.5 which is at the fluid/solid interface.

Convergence study

Stability and convergence of the simulations is an important part of the optimization process. Indicators for this are the computation times, number of iterations and the convergence of the objective values, all these parameters are given in Table B.3. First of all, both methods had issues with converging and it can be seen that all β steps needed the maximum amount of 50 iterations. Secondly, the MDI-D method requires more time to solve for every β step. The Dilgen method had a total calculation time of $12h31m24s$ while the mesh dependent inverse impermeability method has a computation time of $15h02m30s$ which is a few hours longer. Finally, evaluating the objective values it can be seen that the models are probably not converged yet, since the objective values are still decreasing in the final step going from β is 12 to 14. However, to minimize the computation time we decided to limit the maximum amount of iterations to 50 and the last step for the heaviside projection slope to be 14.

Table B.3: Convergence data of the Dilgen and MDI-D topology optimization study

	Computation times (hh:mm:ss)		**Number of iterations**		**Objective values**	
β	Dilgen	MDI-D	Dilgen	MDI-D	Dilgen	MDI-D
2	01:56:06	02:39:20	50	50	0.91164	0.84972
4	01:54:15	02:04:27	50	50	0.85536	0.71679
6	01:52:02	02:31:31	50	50	0.76340	0.62446
8	01:58:04	02:10:26	50	50	0.72202	0.60836
10	02:02:09	02:16:16	50	50	0.69768	0.58060
12	02:04:15	02:44:46	50	50	0.65039	0.55417
14	02:01:42	02:33:19	50	50	0.62621	0.53803

B.3.2. Post processing of the optimization results: Turbulent-flow cooling system

To verify the results of the optimized designs, the geometries are post-processed and a CFD analysis is performed using a body-fitted mesh. To obtain a final geometry for this verification, the fluid and solid interface is defined at a threshold value of $\gamma = 0.5$. This means all elements with a density variable lower than 0.5 are solid and the elements with density variables higher than the threshold are fluid. Furthermore, fluid regions which are not connected to the main stream are removed. In Figures B.7a and B.7b the post-processed geometries can be found which are used in the CFD analyses.

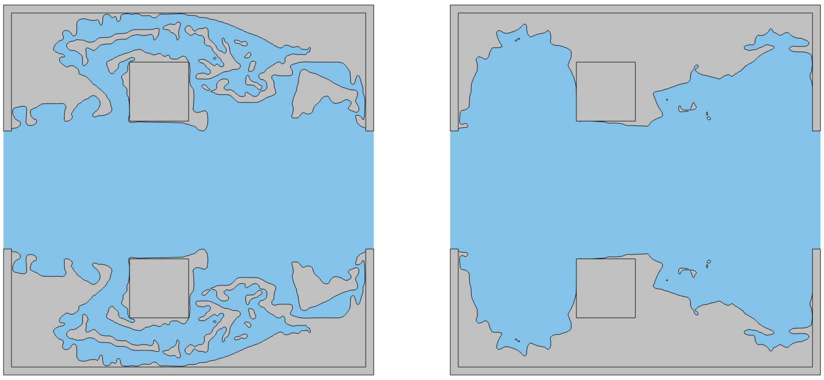

(a) Geometry of the post-processed Topology Optimization with the Dilgen method. Blue is fluid, gray is solid

(b) Geometry of the post-processed Topology Optimization with the MDI-D method. Blue is fluid, gray is solid

Figure B.7: Geometry of the optimized designs post-processed using a threshold value of $\gamma = 0.5$

The velocity magnitudes for the Dilgen verification model are shown in Figure B.8a and for the MDI-D method in Figure B.8b. The velocity magnitudes are showing the same behavior as in the density based model. However in the verification model the velocities are slightly higher, which can be seen in the large circular basins in Figure B.8b. The turbulence intensities in the verification models are plotted in Figures B.9a and B.9b for the Dilgen and MDI-D method respectively. The High-turbulent regimes (with $I \geq 5\%$) are more or less the same as in the Density based models, however for the MDI-D method in the right basin the high turbulent intensity region is smaller. In the high-turbulent region, the turbulent intensities are lower in the verification models compared to the density models. The overestimation of turbulence in the density based models could be an explanation why the heat transfer in the density based models is higher. In turbulent regimes, the heat transfer is increased due to the additional turbulent thermal conductivity which is created in these areas. The total effective thermal conductivity in the flow is a combination of the turbulent thermal conductivity and the thermal conductivity related to the material properties.

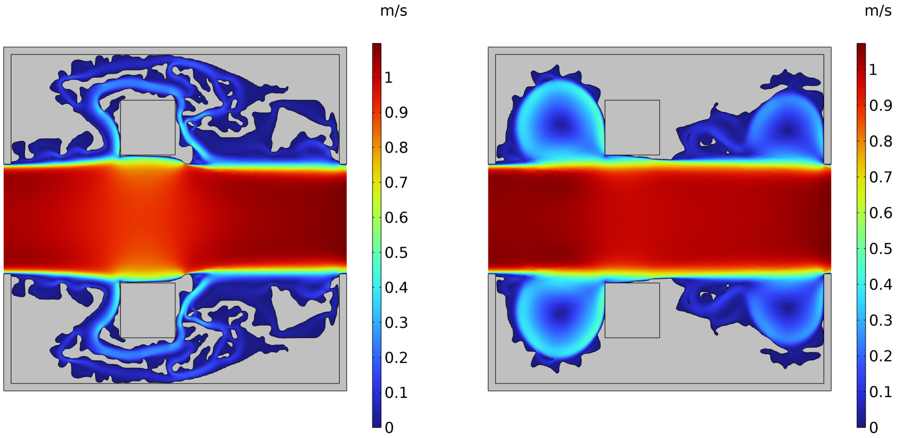

(a) Velocity magnitude with the Dilgen method

(b) Velocity magnitude with the MDI-D method

Figure B.8: Velocity magnitudes of the optimized designs

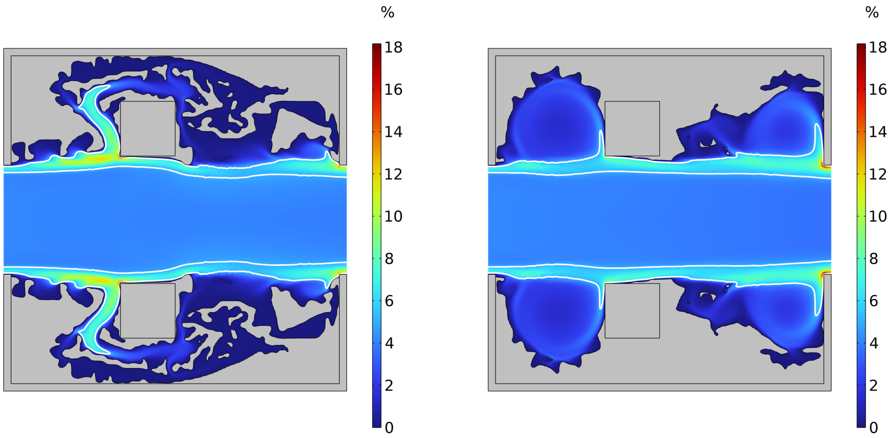

(a) Turbulence intensity with the Dilgen method. Contour is plotted in white at $I = 5\%$

(b) Turbulence intensity with the MDI-D method. Contour is plotted in white at $I = 5\%$

Figure B.9: Turbulent intensities of the optimized designs

Finally the temperature distribution is verified, the temperature distributions can be found in Figure B.10. In the verification results of the Dilgen method (Figure B.10a) it can be seen that the temperature is sort of trapped inside the heat source and the small solid domain around it. This means that the flow around the heat source is not capable of cooling the heat source enough. Moreover, the temperature difference between the density based models and the verification models is also large, which means that the density based models overestimate the amount of heat transfer, this holds for the Dilgen design as well for the MDI-D design. The overestimation of heat transfer is likely caused by a large amount of convective heat transfer in the solid domain and the overestimation of turbulence in the density based model. The MDI-D method temperature distribution (Figure. B.10b) shows a similar behavior, as the verification model still shows higher temperatures in the heat source. In the MDI-D method the heat transfer due to conduction is larger compared to the Dilgen design. The heat transfer is increased by first spreading the heat over a larger solid area and after that the fluid has a larger interface area with the solid where it is capable of absorbing the heat into the fluid. Finally, in the circular basins the heat in the fluid is transfered by convective heat transfer towards the large main channel where it is taken out of the domain. During optimization, the Dilgen approach resulted in a better optimum than the MDI-D approach. The average heat source temperature was 311.62K for the Dilgen method while for the MDI-D method the average heat source temperature was 325.16K using the density based model. However, when comparing the verification models, the temperature for the Dilgen method is 433.85K which is larger then the temperature for the MDI-D method which is 415.13K. The average heat source temperatures minus the inlet temperature ($\Delta\overline{T}$) are also shown in Table B.4. First, it can thus be said that the MDI-D method is more accurate considering the temperature distribution, although the density based model and verification model still deviate. Secondly, the MDI-D method also generated a design with a higher cooling performance compared to the Dilgen method, according to the verification models.

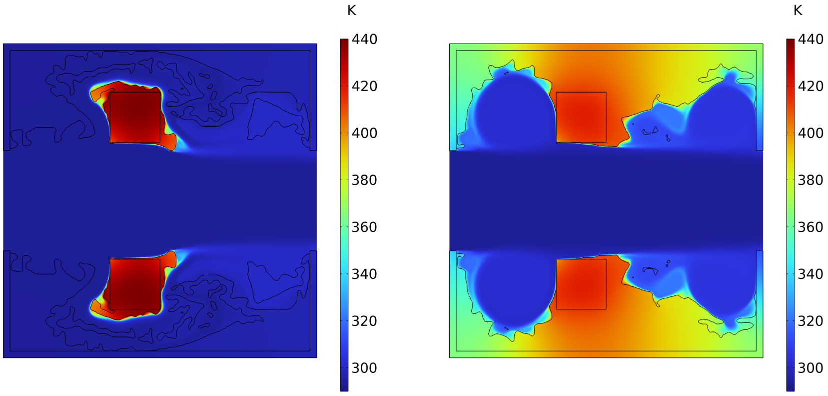

(a) Temperature with the Dilgen method

(b) Temperature with the MDI-D method

Figure B.10: Temperature distribution of the optimized designs

Table B.4: Average ΔT in the heat source, with $\Delta\overline{T}_{Heatsource} = \overline{T}_{Heatsource} - T_{in}$

	Dilgen method	**MDI-D method**
Density model $\Delta\overline{T}_{Heatsource}$	18.47 K	32.01 K
Verification model $\Delta\overline{T}_{Heatsource}$	140.70 K	121.98 K
Error density model w.r.t. verification model	86.9%	73.8%

The objective values for each situation are given in Table B.5, the total objective (H), the pressure objective (H_{pres}) and the temperature objective (H_T) are shown. The objective values are computed for the density based topology optimization as well as the verification model, this can give more information about the accuracy of the model. It can be seen that the error on the total objective for both, the Dilgen as the MDI-D method, is large. The Dilgen method has an error of 73.9% of the total objective with respect to the verification model. The MDI-D method has a better performance with an error of 59.1%. The large difference in the objective values between the density based model and the verification model is mainly caused by the temperature objective since the pressure objectives are almost perfect for both models. The temperature objectives have an error of 86.9% and 73.8% for the Dilgen and MDI-D method respectively. The large error is probably caused by the intermediate density variables, here the convective heat flux is still quite high, while some of these regions will be completely solid in the verification model and thus have no convective heat transfer at these locations.

Table B.5: Objective values for both methods with the Topology optimization and verification case

	Dilgen method			**MDI-D method**		
	H	H_{pres}	H_T	H	H_{pres}	H_T
Density-based study	0.626	0.358	0.268	0.538	0.260	0.278
Verification study	2.403	0.359	2.044	1.316	0.256	1.060
Error	73.9%	0.3%	86.9%	59.1%	1.6%	73.8%

B.3.3. Conclusions on the heat transfer optimization problem

The MDI-D method shows promising results for Topology Optimization. It proves that the optimization results can be improved compared to the Dilgen method. Probably the largest difference is due to the higher impermeability value in the MDI-D method, this results in lower velocities through the solid domain. Therefore the convective heat flux through the solid domain is reduced and the optimization accounts for this by increasing the solid domain and the conductive heat flux. Although the Dilgen method uses a penalization on the convective heat flux this does not seem strong enough to limit the convective heat flux in the solid domain. As said, the MDI-D method shows great results but it must be noted that this method influences the stability of the models. The computation times are increased from $12h31m24s$ to $15h02m30s$ which is an increase of 20% computation time, which shows that the solver has more issues with converging and solving the physics. Also in this test problem several time saving settings are implemented which influences the results of the final solution. This was required since the computation times became too large otherwise.

C

Overview of the flow properties in the lower channel

In this appendix the evaluated flow properties are given for the lower channel.

C.1. Dilgen method

In this section the flow properties in the lower channel are presented with the Dilgen method. In Figure C.1 the velocity can be found, in Figure C.2 the specific dissipation rate and in Figure C.3 the turbulent kinetic energy.

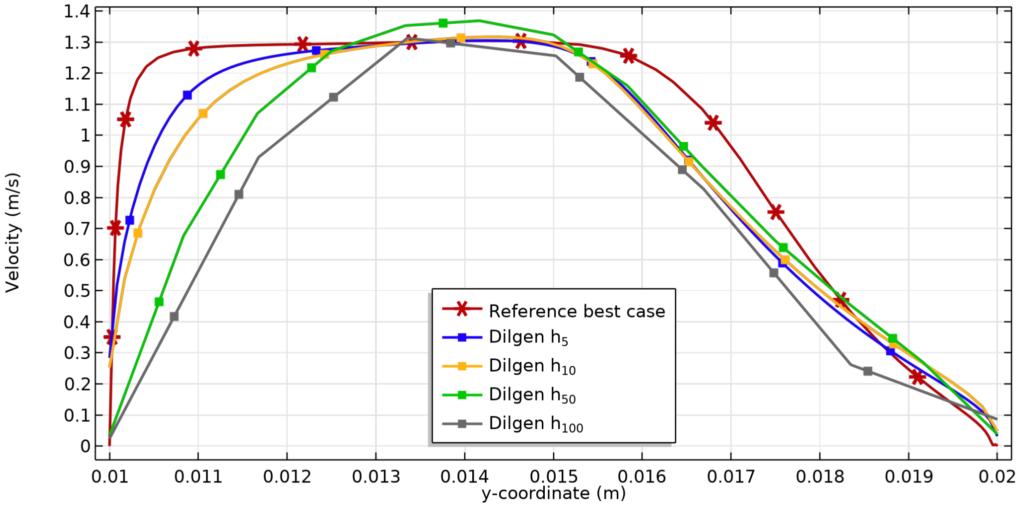

(a) Velocity profiles in the Lower channel for the Dilgen method.

Figure C.1: Velocity in the lower channel for the Dilgen method

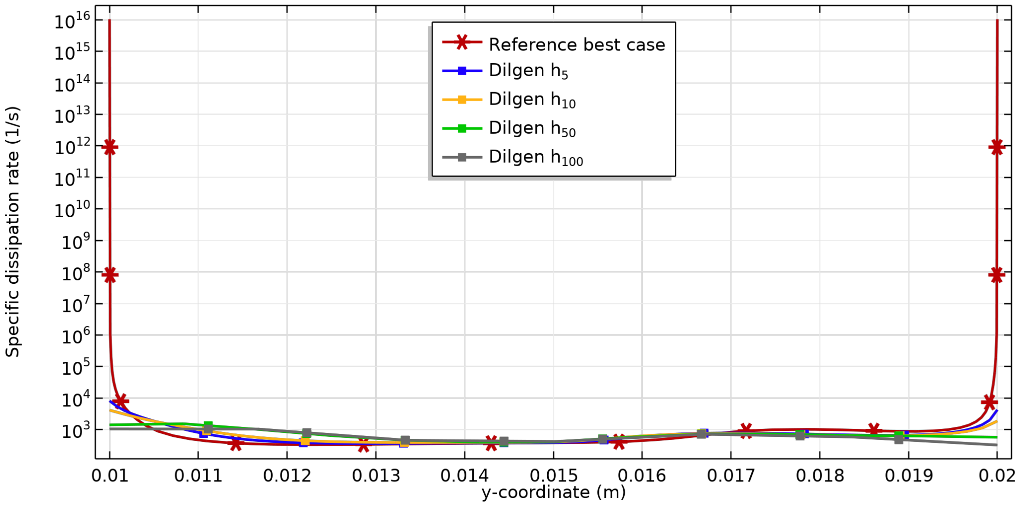

(a) Specific dissipation rate for the Dilgen method.

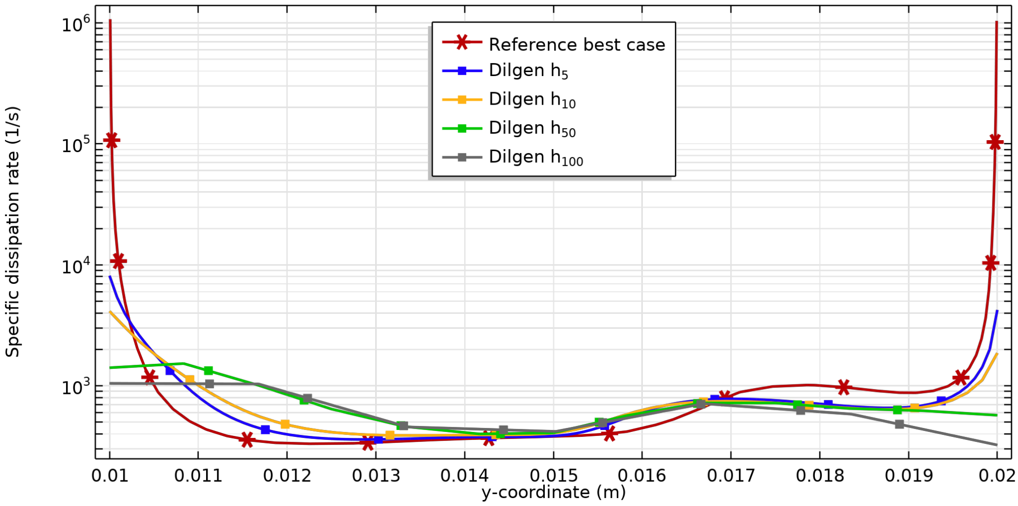

(b) Specific dissipation rate cutoff in the Lower channel for the Dilgen method.

Figure C.2: Specific dissipation rate in the lower channel for the Dilgen method

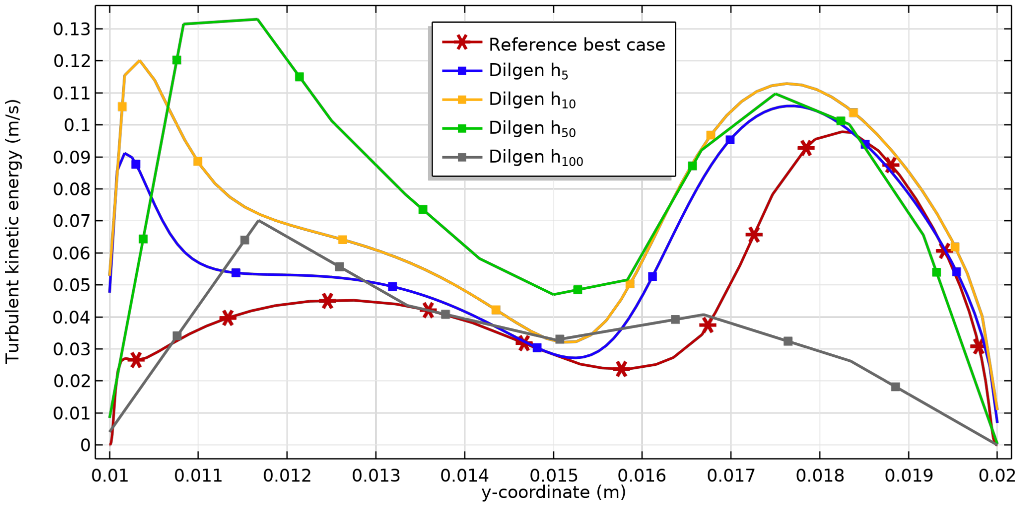

(a) Turbulent kinetic energy for the Dilgen method.

Figure C.3: Turbulent kinetic energy in the lower channel for the Dilgen method

C.2. Dilation method

In this section the flow properties in the lower channel are presented with the Dilation method. In Figure C.4 the velocity can be found, in Figure C.5 the specific dissipation rate and in Figure C.6 the turbulent kinetic energy.

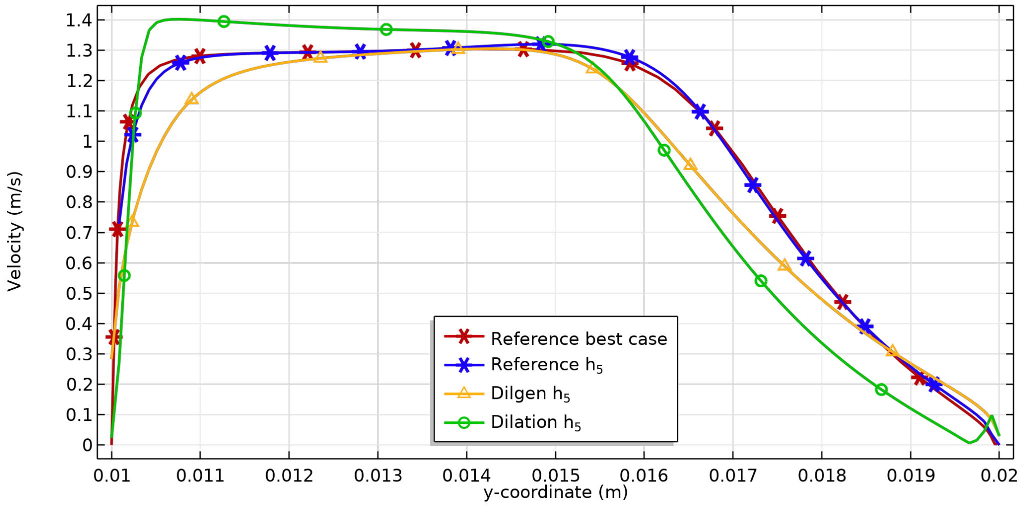

(a) Velocity for h_5

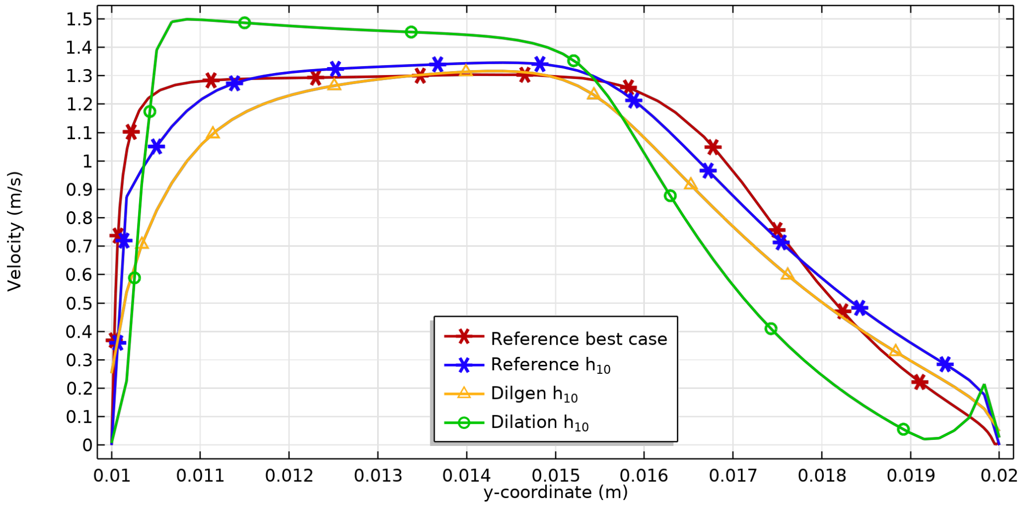

(b) Velocity for h_{10}

Figure C.4: Velocity in the lower channel for the Dilation method

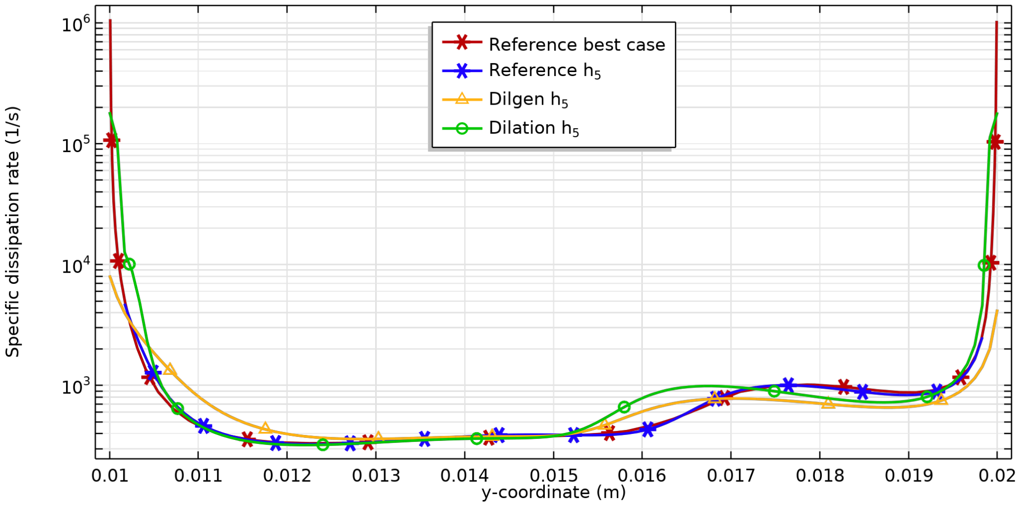

(a) Specific dissipation rate for h_5

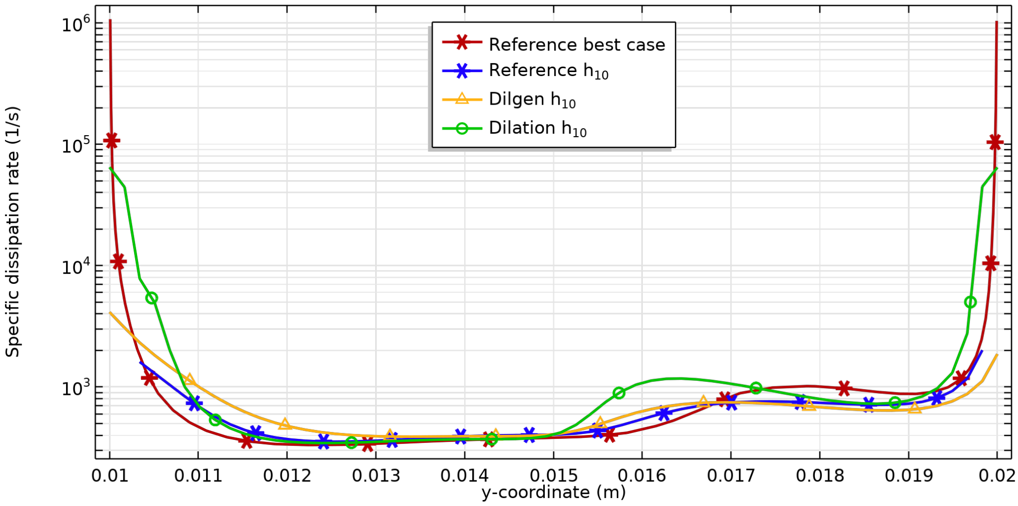

(b) Specific dissipation rate for h_{10}

Figure C.5: Specific dissipation rate in the lower channel for the Dilation method

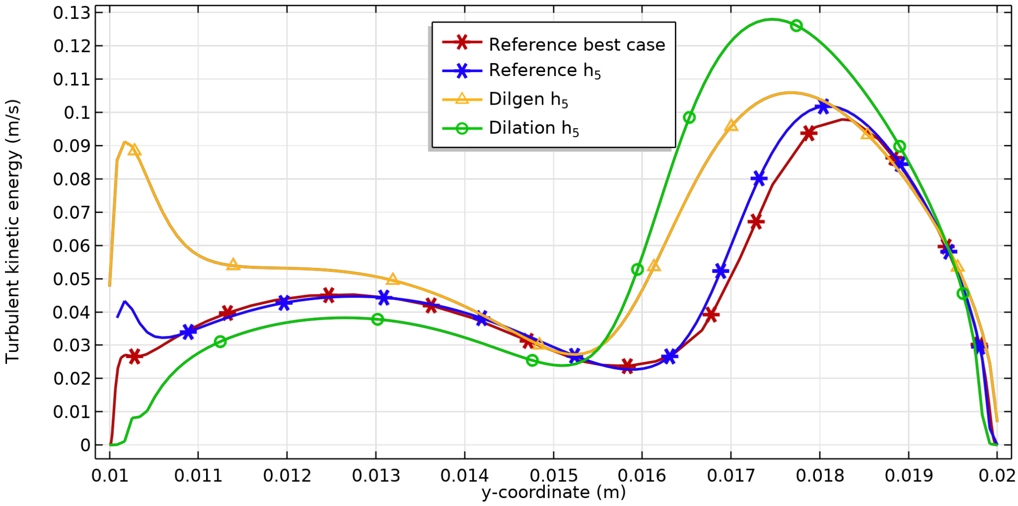

(a) Turbulent kinetic energy for h_5

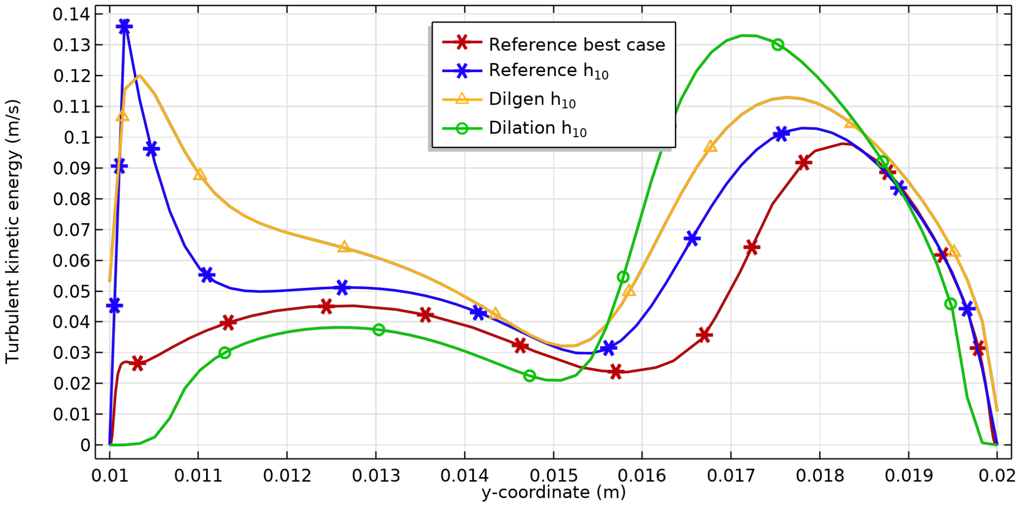

(b) Turbulent kinetic energy for h_{10}

Figure C.6: Turbulent kinetic energy in the lower channel for the Dilation method

C.3. Mesh dependent impermeability method

In this section the flow properties in the lower channel are presented with the MDI method. In Figure C.7 the velocity can be found, in Figure C.8 the specific dissipation rate and in Figure C.9 the turbulent kinetic energy.

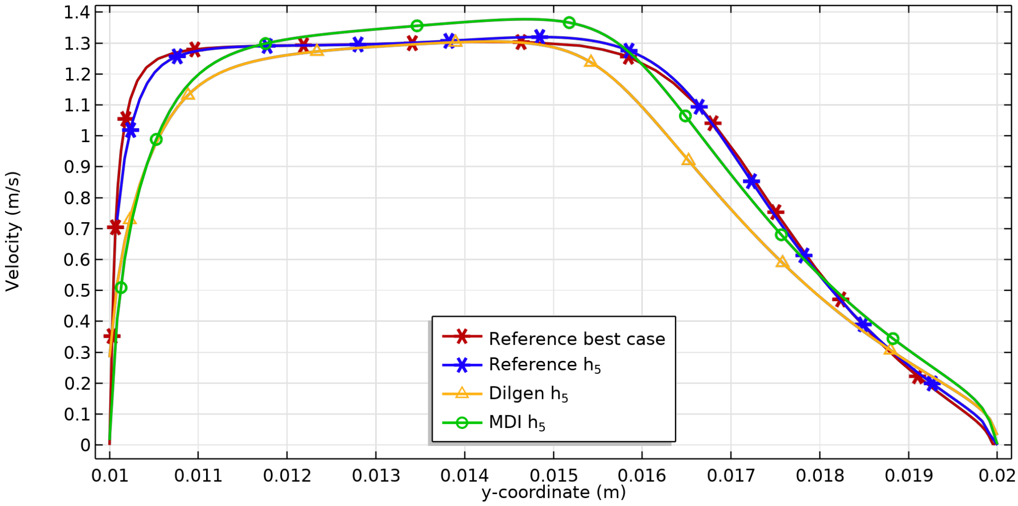

(a) Velocity for h_5

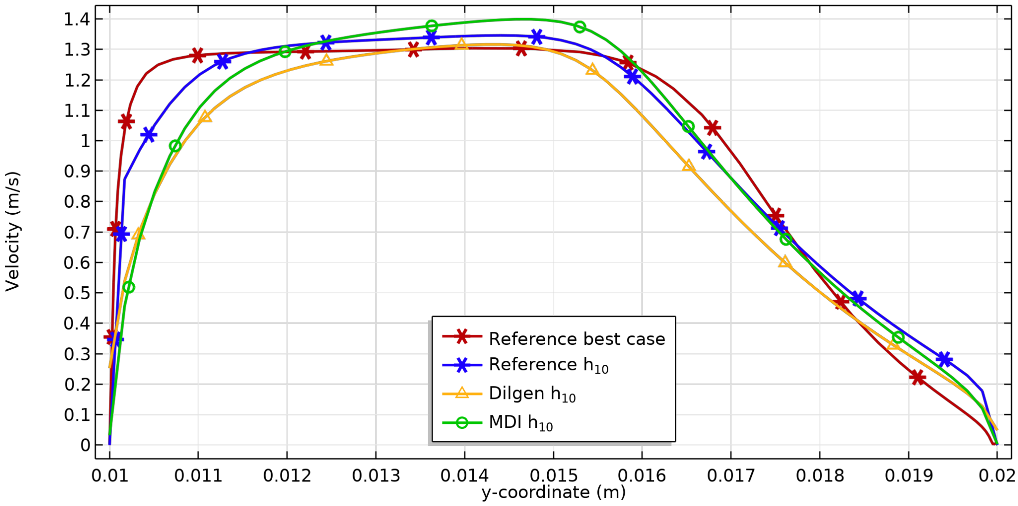

(b) Velocity for h_{10}

Figure C.7: Velocity in the lower channel for the MDI method

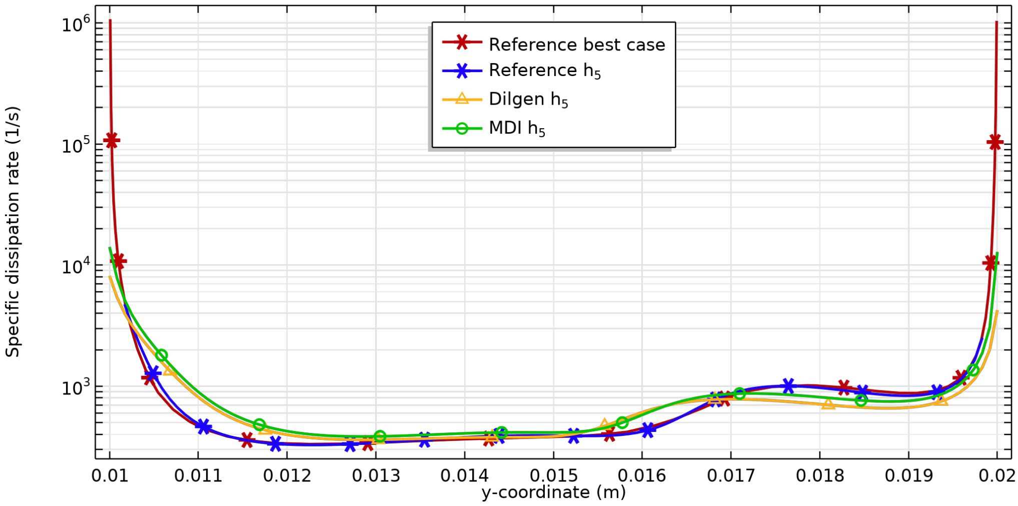

(a) Specific dissipation rate for h_5

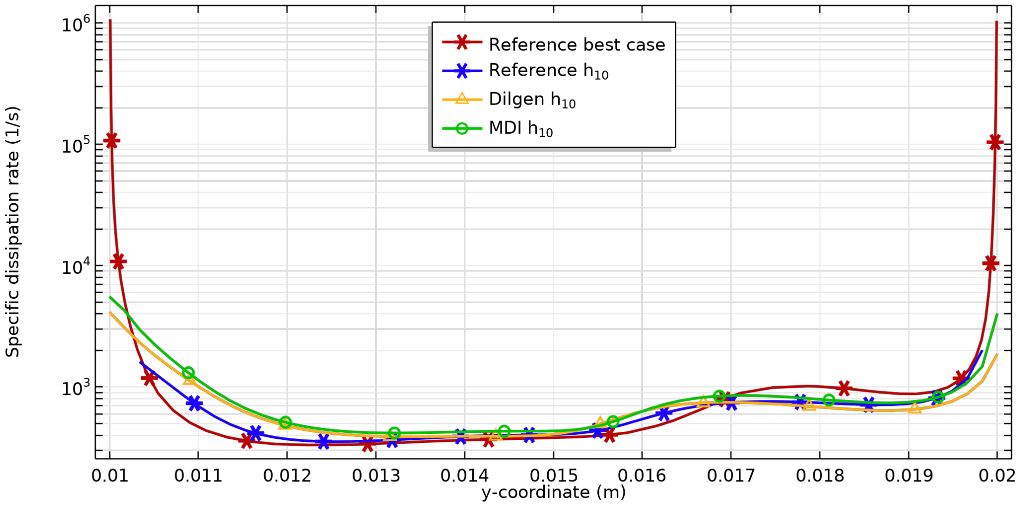

(b) Specific dissipation rate for h_{10}

Figure C.8: Specific dissipation rate in the lower channel for the MDI method

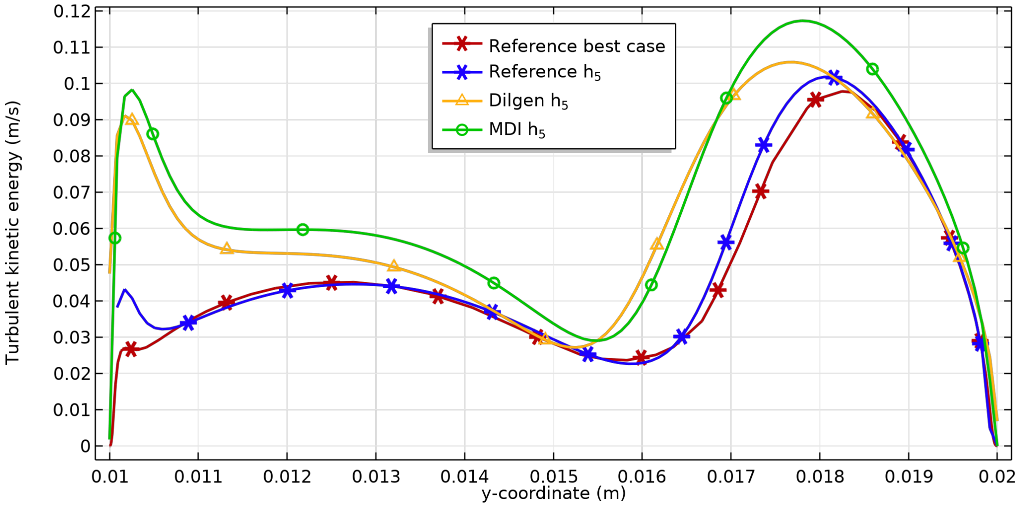

(a) Turbulent kinetic energy for h_5

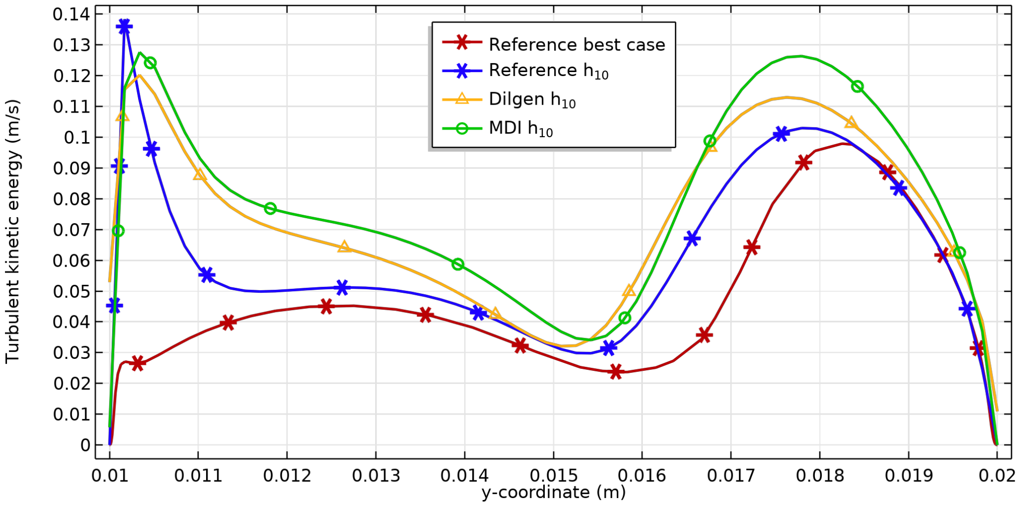

(b) Turbulent kinetic energy for h_{10}

Figure C.9: Turbulent kinetic energy in the lower channel for the MDI method

C.4. Mesh dependent impermeability with dilation method

In this section the flow properties in the lower channel are presented with the MDI-D method. In Figure C.10 the velocity can be found, in Figure C.11 the specific dissipation rate and in Figure C.12 the turbulent kinetic energy.

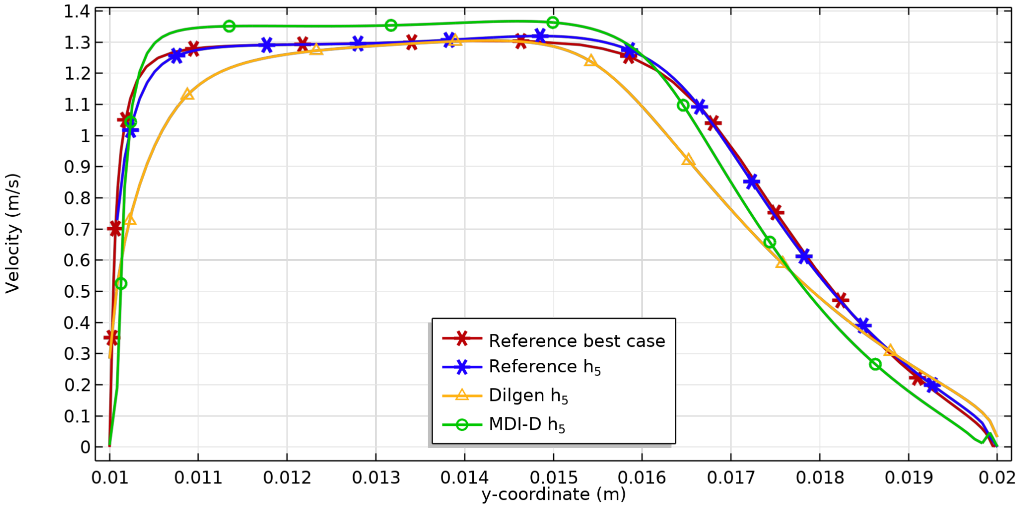

(a) Velocity for h_5

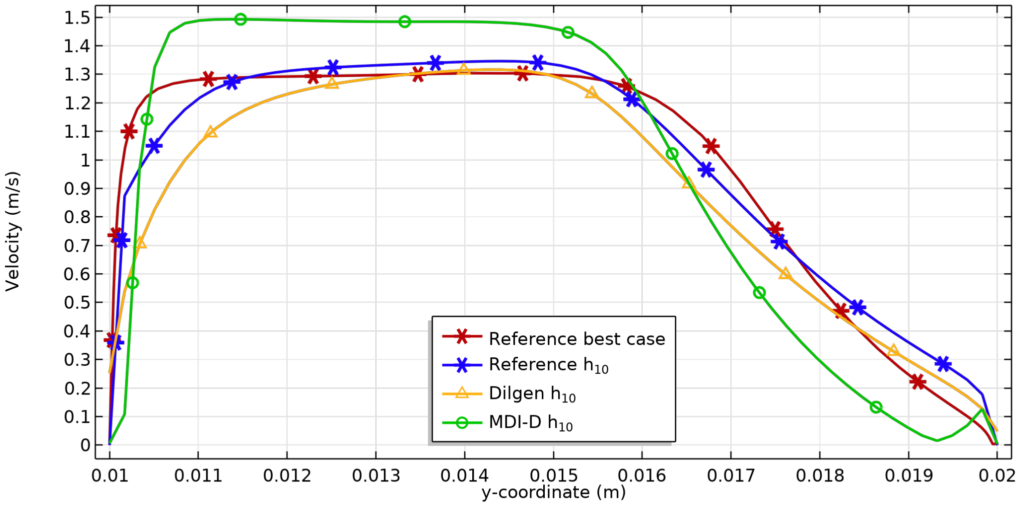

(b) Velocity for h_{10}

Figure C.10: Velocity in the lower channel for the MDI-D method

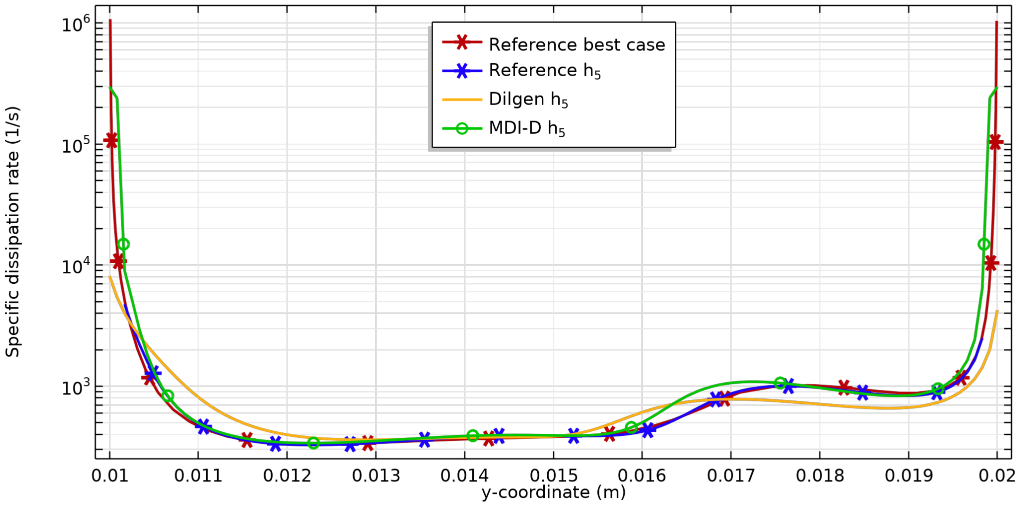

(a) Specific dissipation rate for h_5

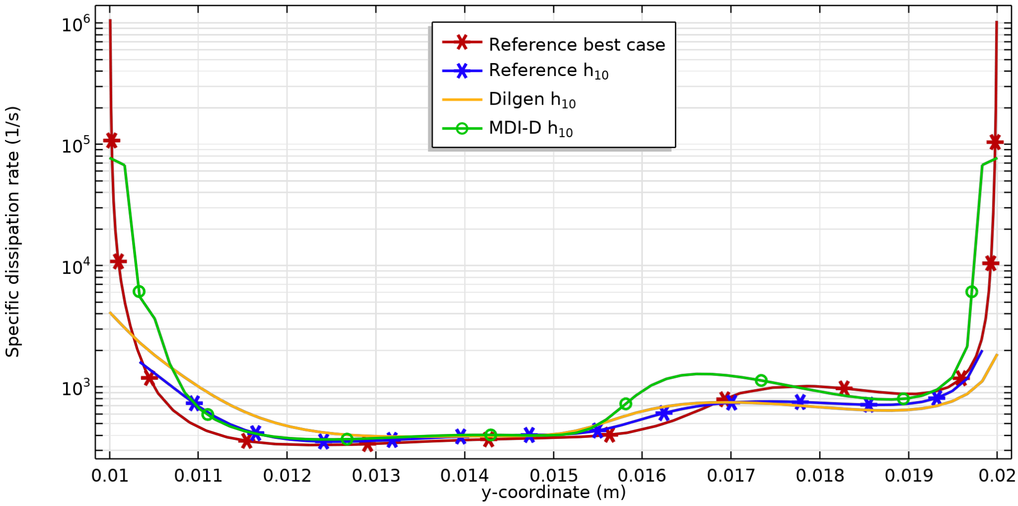

(b) Specific dissipation rate for h_{10}

Figure C.11: Specific dissipation rate in the lower channel for the MDI-D method

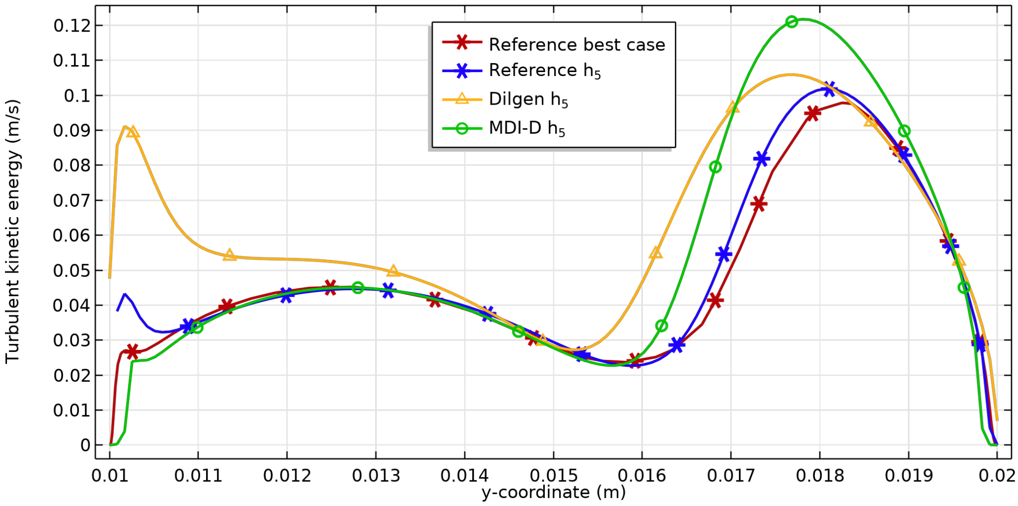

(a) Turbulent kinetic energy for h_5

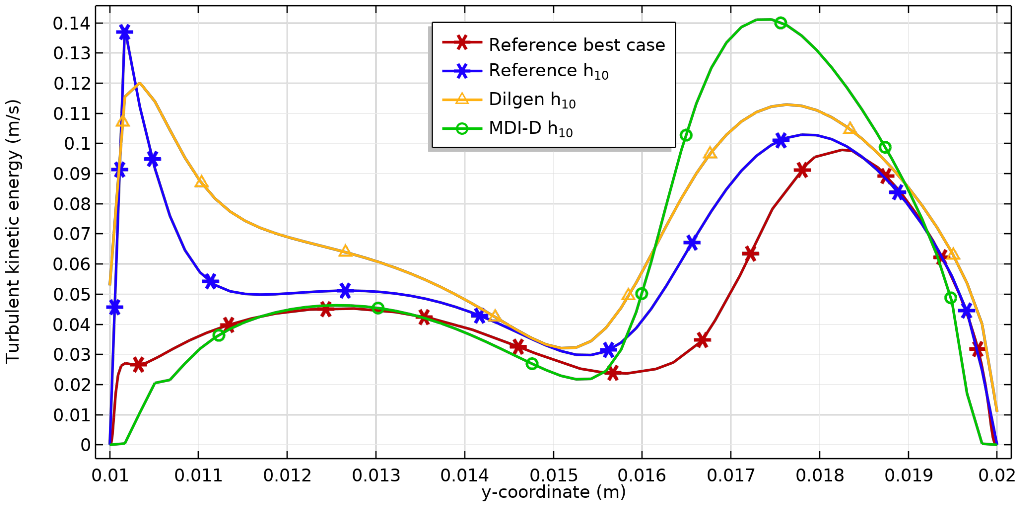

(b) Turbulent kinetic energy for h_{10}

Figure C.12: Turbulent kinetic energy in the lower channel for the MDI-D method

D

Full overview domain errors

In this appendix all the RRMSE on the full domain are presented including the errors on the larger h_x meshes which were not given in their specific chapter.

Table D.1: Overview of all RRMSE of the published methods part 1

Method	h_x	**RRMSE** U	**RRMSE** p	**RRMSE** k	**RRMSE** ω	**RRMSE** μ_T	**RRMSE** ΔT
Dilgen w.r.t. reference best case	5	10.39 %	23.41 %	48.22 %	99.24 %	26.27 %	84.69 %
	10	13.26 %	42.36 %	75.91 %	98.78 %	39.91 %	86.14 %
	50	26.51 %	108.93 %	103.98 %	89.83 %	51.05 %	86.22 %
	100	34.26 %	217.11 %	62.41 %	89.38 %	32.24 %	87.14 %
Dilgen w.r.t. reference h_x case	5	9.62 %	21.47 %	43.57 %	99.31 %	22.62 %	76.87 %
	10	8.63 %	13.10 %	30.88 %	98.57 %	17.03 %	34.57 %
	50	23.55 %	64.68 %	80.91 %	92.68 %	95.54 %	52.76 %
	100	30.00 %	61.31 %	92.42 %	99.12 %	98.39 %	80.30 %
Dilgen WD w.r.t. reference best case	5	9.50 %	18.25 %	39.89 %	98.96 %	21.26 %	83.22 %
	10	8.54 %	8.78 %	26.22 %	96.56 %	15.91 %	81.20 %
	50	28.67 %	65.07 %	56.59 %	150.46 %	53.82 %	82.32 %
	100	33.27 %	124.25 %	87.59 %	399.63 %	88.64 %	89.97 %
Dilgen WD w.r.t. reference h_x case	5	8.68 %	16.42 %	34.94 %	99.03 %	17.49 %	74.67 %
	10	6.11 %	19.60 %	28.12 %	95.90 %	17.13 %	16.29 %
	50	30.31 %	78.15 %	94.66 %	223.33 %	98.48 %	97.93 %
	100	27.48 %	75.95 %	98.96 %	939.98 %	99.75 %	57.00 %
Dilation w.r.t. reference best case	5	14.91 %	30.07 %	47.44 %	84.53 %	31.74 %	66.34 %
	10	20.95 %	47.04 %	55.40 %	85.73 %	38.06 %	70.27 %
	50	39.06 %	107.45 %	80.19 %	87.01 %	85.84 %	78.25 %
	100	35.40 %	214.88 %	73.84 %	89.27 %	68.11 %	87.03 %
Dilation w.r.t. reference h_x case	5	14.19 %	29.35 %	43.27 %	85.28 %	28.83 %	52.15 %
	10	16.99 %	41.37 %	52.78 %	84.34 %	36.21 %	73.56 %
	50	37.82 %	70.84 %	97.69 %	104.78 %	99.57 %	168.91 %
	100	31.82 %	62.34 %	95.97 %	104.39 %	99.39 %	93.04 %

Table D.2: Overview of all RRMSE of the published methods part 2

Method	h_x	**RRMSE U**	**RRMSE p**	**RRMSE k**	**RRMSE ω**	**RRMSE μ_T**	**RRMSE ΔT**
MDI w.r.t. reference best case	5	9.14 %	30.80 %	54.87 %	98.46 %	26.34 %	83.35 %
	10	12.90 %	49.62 %	84.57 %	98.17 %	39.32 %	85.20 %
	50	26.41 %	118.53 %	112.99 %	89.81 %	55.81 %	86.30 %
	100	34.08 %	149.12 %	50.93 %	89.41 %	32.90 %	86.86 %
MDI w.r.t. reference h_x case	5	8.01 %	28.64 %	50.06 %	98.55 %	22.89 %	74.84 %
	10	7.16 %	18.55 %	37.09 %	97.84 %	17.68 %	30.40 %
	50	23.45 %	62.88 %	79.95 %	92.84 %	95.35 %	51.68 %
	100	28.70 %	70.16 %	92.94 %	96.45 %	98.42 %	74.87 %
MDI-D w.r.t. reference best case	5	8.36 %	9.01 %	25.82 %	88.01 %	9.46 %	65.83 %
	10	18.22 %	28.51 %	49.25 %	89.50 %	21.12 %	69.24 %
	50	34.74 %	98.01 %	51.86 %	79.84 %	49.45 %	81.86 %
	100	34.70 %	153.13 %	53.69 %	88.62 %	35.30 %	86.06 %
MDI-D w.r.t. reference h_x case	5	7.34 %	9.31 %	21.33 %	87.94 %	6.34 %	49.91 %
	10	14.09 %	30.46 %	45.76 %	90.30 %	22.94 %	55.48 %
	50	33.24 %	72.17 %	90.38 %	88.25 %	98.14 %	109.03 %
	100	28.89 %	69.66 %	93.40 %	96.41 %	98.59 %	89.08 %
Forchheimer w.r.t. reference best case	5	15.03 %	15.24 %	33.48 %	98.44 %	24.81 %	80.99 %
	10	24.28 %	24.53 %	45.75 %	98.02 %	38.22 %	81.87 %
	50	43.27 %	50.33 %	67.16 %	90.89 %	62.72 %	80.21 %
	100	49.56 %	61.67 %	80.56 %	91.54 %	72.87 %	80.80 %
Forchheimer w.r.t. reference h_x case	5	14.46 %	15.31 %	29.86 %	98.53 %	21.68 %	71.63 %
	10	21.31 %	32.51 %	42.15 %	97.64 %	28.44 %	31.11 %
	50	39.43 %	89.04 %	95.33 %	91.44 %	98.11 %	179.41 %
	100	44.27 %	94.24 %	98.22 %	91.60 %	99.24 %	190.27 %
Forchheimer dilated w.r.t. reference best case	5	23.88 %	29.05 %	55.95 %	95.28 %	36.79 %	65.35 %
	10	31.05 %	34.12 %	55.49 %	94.7 %	41.46 %	72.63 %
	50	46.13 %	51.43 %	95.51 %	85.75 %	93.23 %	78.94 %
	100	50.64 %	61.50 %	96.25 %	88.87 %	95.59 %	78.67 %
Forchheimer dilated w.r.t. reference h_x case	5	23.29 %	28.55 %	52.63 %	94.68 %	34.11 %	53.07 %
	10	27.64 %	36.23 %	64.79 %	97.17 %	44.68 %	107.51 %
	50	42.88 %	87.57 %	99.52 %	101.45 %	99.85 %	278.34 %
	100	45.71 %	93.87 %	99.73 %	99.67 %	99.92 %	254.63 %

E

Additional improved methods

E.1. Dilgen wall distance approach

The first method tested is an improvement on the Dilgen method as explained in Chapter 4 by using the actual wall distance in the ω penalization (Eq. 3.28) instead of the mesh size (Eq. 3.29). This Dilgen wall distance approach will henceforth be referred to as Dilgen WD. The wall distance is an important parameter in turbulent-flow simulations, since the flow is evolving in the near wall region and the development of the flow is dependent on the wall distance. By using the actual wall distance instead of an estimation, namely the mesh size, in the ω_b equation (Eq. 3.29) it is expected to obtain more accurate results. The theory is that the wall distance could approach zero when reaching porous 'solid' areas and thus creating a higher ω_b target. The equation for determining ω_b is now as follows,

$$\omega_b = \frac{60\nu}{\beta_1 y_1^2} = \frac{60\nu}{\beta_1 l_w^2} \tag{E.1}$$

where l_w is the wall distance in m and is determined using Equation 3.13.

E.1.1. Results of the Dilgen wall distance approach

In this section the velocity profiles, specific dissipation rates and the turbulent kinetic energies are investigated for the Dilgen WD method where the dissipation rate at the solid fluid interface is computed using wall distance l_w as shown in Equation E.1.

Velocity (U)

The velocity profiles for the Dilgen WD method are shown in Figure E.1. Each subfigure is focused on either the h_5 or h_{10} model. In Figure E.1a the velocity profiles for the h_5 model are shown, which for the Dilgen WD shows similar results as for the original Dilgen method. Near the wall it can be seen that the Dilgen WD performs slightly better (Fig. E.1b) since it converges closer to zero. The h_{10} model shows more difference between each result. The Dilgen WD is more accurate near the wall and matches the reference best case, which can also be seen in Figure E.1d where the velocity almost reach zero at the wall. However, in the free stream the Dilgen WD gives a similar result as the Dilgen method. Table E.1 shows that the h_{10} model has the lowest error with respect to the best case reference for the upper channel. In the lower channel the errors are increasing, this might be caused by the turbulence in the lower channel which is hard to simulate in these density simulations.

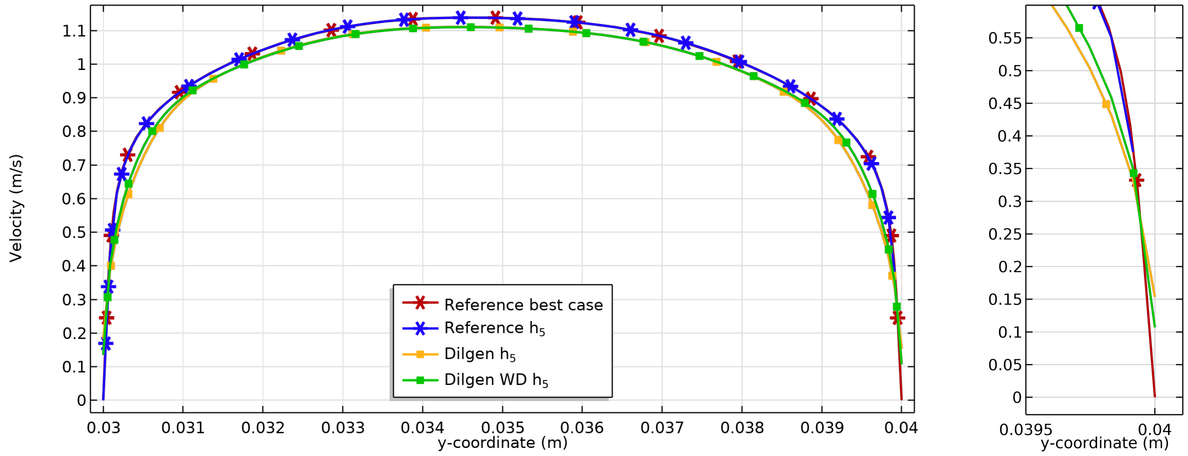

(a) Velocity profile in the upper channel for h_5

(b) Velocity profile at the wall for the Dilgen WD method and h_5

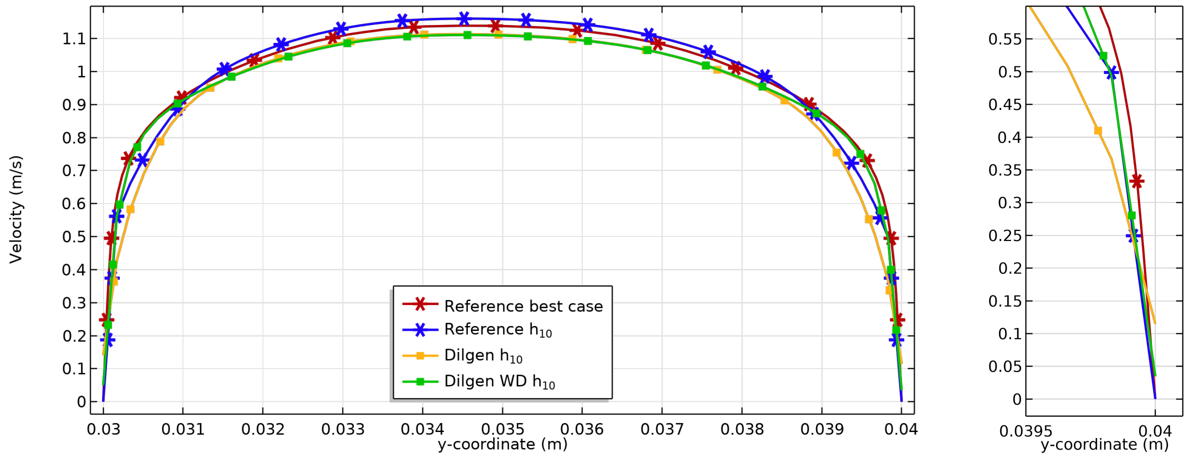

(c) Velocity profile in the upper channel for h_{10}

(d) Velocity profile at the wall for the Dilgen WD method and h_{10}

Figure E.1: Velocity profiles in the upper channel of the Dilgen WD method for h_5 and h_{10} meshes.

Table E.1: RRMSE of the velocity on the cut lines in the upper and lower channel using the Dilgen WD approach. The RRMSE of the Dilgen method are included as well for comparison.

		Dilgen WD method		**Dilgen** method	
Location	**w.r.t.**	h_5	h_{10}	h_5	h_{10}
Upper channel	Reference best case	3.67 %	2.96 %	4.62 %	6.33 %
	Reference h_x case	3.55 %	4.32 %	4.48 %	4.77 %
Lower channel	Reference best case	10.26 %	9.06 %	11.13 %	14.34 %
	Reference h_x case	9.25 %	7.46 %	10.12 %	9.50 %

Specific dissipation rate (ω)

Figure E.2 shows the results for the specific dissipation rates in the upper channel. To be able to visually inspect the figure we do not display the extremely high dissipation rates at the wall computed using the reference best case. Therefore, the reference simulations show values several orders lower than their actual value at the wall which is $\omega_b = 1.0393E16\ 1/s$. The h_5 results for the Dilgen WD approach shows similar results as the Dilgen method. Unfortunately the ω_b target is not increased and thus the actual specific dissipation rate at the wall is neither increased. However, the h_{10} results show an improvement on the specific dissipation rate in the near wall region compared to the Dilgen method. This means that the ω_b target at the wall as given in Eq. E.1 represents the specific dissipation rate better than the Dilgen method. However, the specific dissipation rate at the wall is still several order lower than it should be according to the reference best case.

Thus the introduction of the wall distance in Eq. E.1 did not solve this problem completely. It is still not clear why the h_{10} model shows better results since the ω_b target is $20\,637$ $1/s$ and $17\,289$ $1/s$ for the h_5 and h_{10} models respectively. This means that it would be logical if the h_5 model had a higher specific dissipation rate at the wall, however this is not the case.

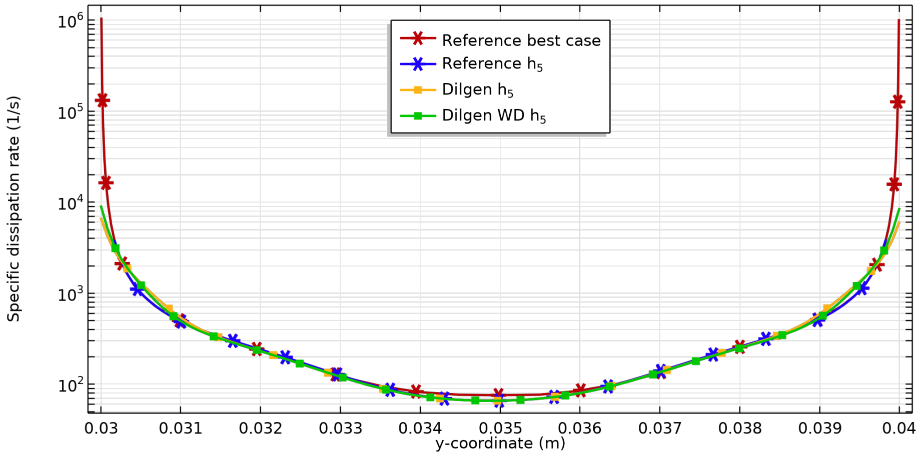

(a) Specific dissipation rate in the upper channel for h_5

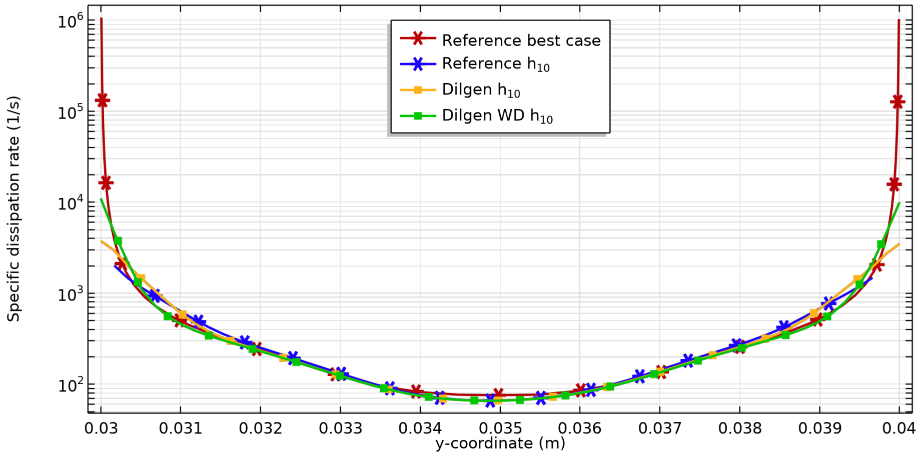

(b) Specific dissipation rate in the upper channel for h_{10}

Figure E.2: Specific dissipation rate in the upper channel with the Dilgen WD method

In Table E.2 the errors regarding the specific dissipation rate are presented. The high errors are caused by the COMSOL wall elements where the specific dissipation rate can reach values up to order 10^{16}. Compared with the Dilgen WD approach which reaches order 10^4 this causes these huge errors.

Table E.2: RRMSE of the specific dissipation rate on the cut lines in the upper and lower channel using the Dilgen WD approach. The RRMSE of the Dilgen method are included as well for comparison.

		Dilgen WD method		**Dilgen** method	
Location	**w.r.t.**	h_5	h_{10}	h_5	h_{10}
Upper channel	Reference best case	98.64 %	98.36 %	98.99 %	99.39 %
	Reference h_x case	98.00 %	97.63 %	98.51 %	99.11 %
Lower channel	Reference best case	98.65 %	98.36 %	99.03 %	99.49 %
	Reference h_x case	98.01 %	97.63 %	98.56 %	99.26 %

Turbulent kinetic energy (k)

The turbulent kinetic energy is the last flow property which is evaluated for the Dilgen WD approach. In Figure E.3 the results for the turbulent kinetic energy in the upper channel are shown. Where the Dilgen WD h_5 model again performs slightly better than the Dilgen method but still the turbulent kinetic energy overshoots the reference in the near wall region. In contrast the Dilgen WD h_{10} results are an improvement on the Dilgen method and almost reach the reference best case simulation. This might be caused due to the increasing specific dissipation rate at the wall as explained in the previous section. Due to the higher specific dissipation rate, the turbulent kinetic energy dampens out which counters the overshoot on the turbulent kinetic energy.

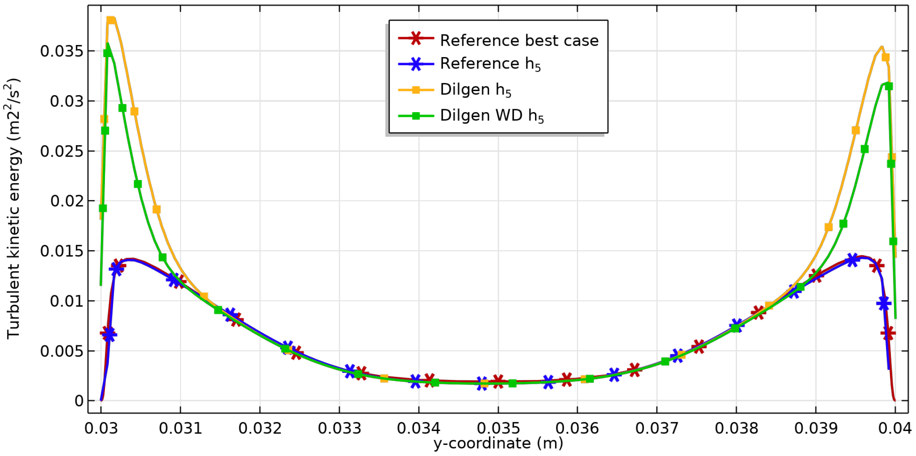

(a) Turbulent kinetic energy in the upper channel for h_5

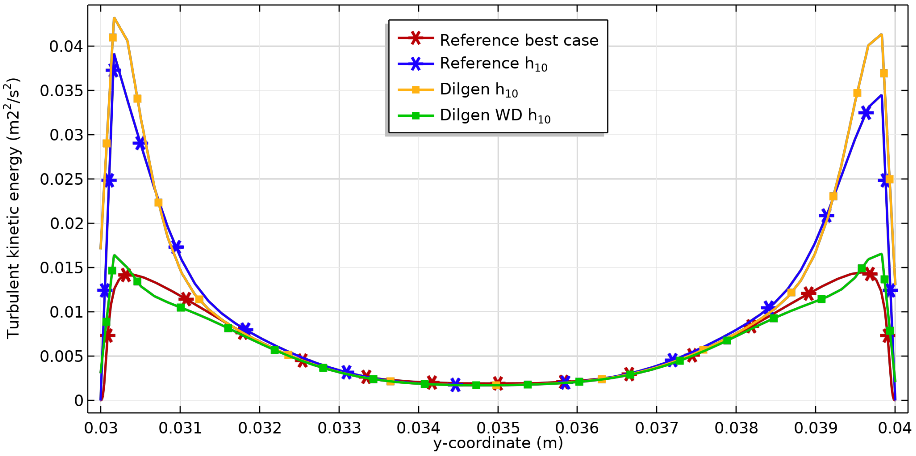

(b) Turbulent kinetic energy in the upper channel for h_{10}

Figure E.3: Turbulent kinetic energy in the upper channel with the Dilgen WD method for h_5 and h_{10} meshes

The RRMSE of the turbulent kinetic energy can be found in Table E.3. First of all, a large difference between the Dilgen WD h_5 and h_{10} model can be observed. As said in the beginning of this section this might be due to the higher specific dissipation rate in the Dilgen WD h_{10} model. Secondly, the Dilgen WD h_{10} model is greatly improved compared to the Dilgen h_{10} model, where we find an error of 13% in the upper channel compared to error of 112% for the Dilgen method in Table 4.7.

Table E.3: RRMSE of the turbulent kinetic energy on the cut lines in the upper and lower channel using the Dilgen WD approach. The RRMSE of the Dilgen method are included as well for comparison.

		Dilgen WD method		**Dilgen method**	
Location	**w.r.t.**	h_5	h_{10}	h_5	h_{10}
Upper channel	Reference best case	70.95 %	13.00 %	91.92 %	111.65 %
	Reference h_x case	74.31 %	47.74 %	95.07 %	18.82 %
Lower channel	Reference best case	37.47 %	25.10 %	43.89 %	67.11 %
	Reference h_x case	30.08 %	27.95 %	36.40 %	22.32 %

E.1.2. Discussion on the Dilgen wall distance approach

Unfortunately the Dilgen WD approach does not show great improvement on the U-bend channel test case. Just as in the Dilgen original method the velocity profiles do approach the reference solution but the velocities are slightly lower than in the reference solution due to flow leakage. The problem of not reaching the boundary condition (zero velocity at the wall) is also not completely solved by this Dilgen WD approach. The same can be said of the specific dissipation rate where the ω_b target is too low at the wall. This results in a turbulent kinetic energies which is too high in the near wall region. Only for the h_{10} model a slight improvement can be noticed but still some improvements can be made. This is supported by the overall errors given in Table E.4 which shows similar errors to the Dilgen method. The reason why this method is not improving much is due to the wall distance, which is coupled to the mesh size resolution.

Table E.4: RRMSE Dilgen WD with respect to reference best case and reference with corresponding h_x mesh

		Dilgen WD			**Dilgen**		
w.r.t.	h_x	**RRMSE** U	**RRMSE** k	**RRMSE** ω	**RRMSE** U	**RRMSE** k	**RRMSE** ω
reference best case	h_5	9.50 %	39.89 %	98.96 %	10.39 %	48.22 %	99.24 %
	h_{10}	8.54 %	26.22 %	96.56 %	13.26 %	75.91 %	98.78 %
reference h_{y^+} case	h_5	8.68 %	34.94 %	99.03 %	9.62 %	43.57 %	99.31 %
	h_{10}	6.11 %	28.12 %	95.90 %	8.63 %	30.88 %	98.57 %

E.2. Forchheimer method

In this section a method is presented based on the research of Alonso and Silva [46], where they present an additional penalty factor which accounts for the Forchheimer effect. The inertia of the particles in a porous medium also influences the flow through the porous medium and thus should this be penalized as well. The representation of the Darcy effect and Forchheimer effect can be found in Figure E.4. The Forchheimer term scales quadratically with the velocity in the fluid and thus should the flow is penalized more in inertial areas.

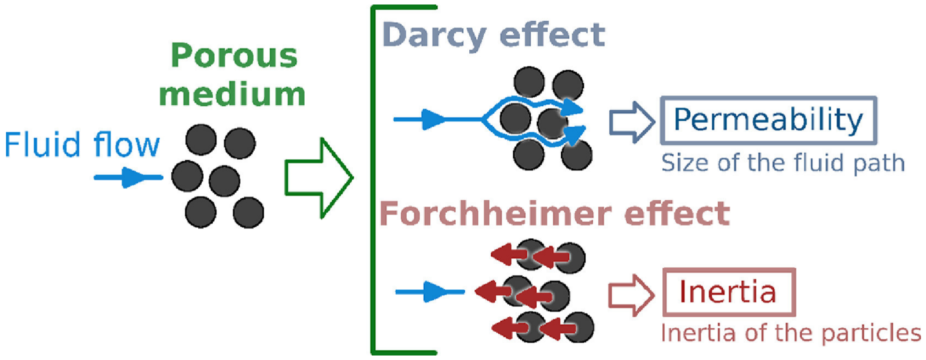

Figure E.4: Darcy and Forchheimer effects in porous medium, from [46]

The Forchheimer effect only affects the RANS equation resulting in the following equation,

$$\rho\frac{\partial\vec{U}}{\partial t} + \rho\vec{U}\cdot\nabla\vec{U} = -\nabla P + \nabla\cdot(\mu+\mu_T)\left(\nabla\vec{U} + \left(\nabla\vec{U}\right)^T\right) - \underbrace{\alpha_1\rho\vec{U}}_{\text{Darcy effect}} - \underbrace{\alpha_2\rho|\vec{U}|\vec{U}}_{\text{Forchheimer effect}} . \tag{E.2}$$

where α_1 and α_2 are dependent on their respective maximum inverse impermeability given by,

$$\overline{\alpha_1} = 10^q\frac{\nu}{h^2}, \tag{E.3}$$

and

$$\overline{\alpha_2} = 10^q\frac{1}{h}, \tag{E.4}$$

where q is a penalization factor generally of value 0, 1 or 2.

E.2.1. Results on the Forchheimer method

In this section the velocity, specific dissipation rate and the turbulent kinetic energy with the Forchheimer method will be presented.

Velocity (U)

First the velocity profile for the h_5 case will be analyzed which is plotted in Figure E.5a. The Forchheimer method should be improving on the areas where the inertial areas dominate since the added Forchheimer term scales with the quadratic of the velocity. The inertial areas are normally not at the wall interface but rather at the freestream or loglaw regime. However in the freestream the the second inverse impermeability (α_2) is not active since no gray areas are present here, this means that the Forchheimer mainly contributes to loglaw regime a bit from the wall. When analyzing this area it can be seen that the velocity profile follows the reference simulation quite accurately in this region. Unfortunately in the free stream the Forchheimer method performs worse than the Dilgen method. Thus the Forchheimer method contributes in a positive way in the inertial regime near the wall, however it has also negative influence on the velocity in the middle of the channel.

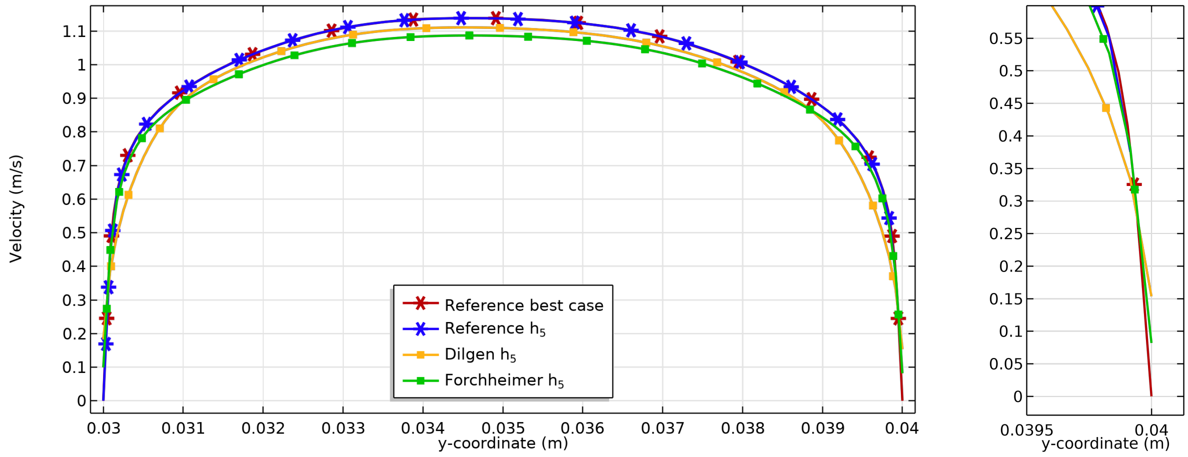

(a) Velocity profile for h_5

(b) Velocity profile at the wall for h_5

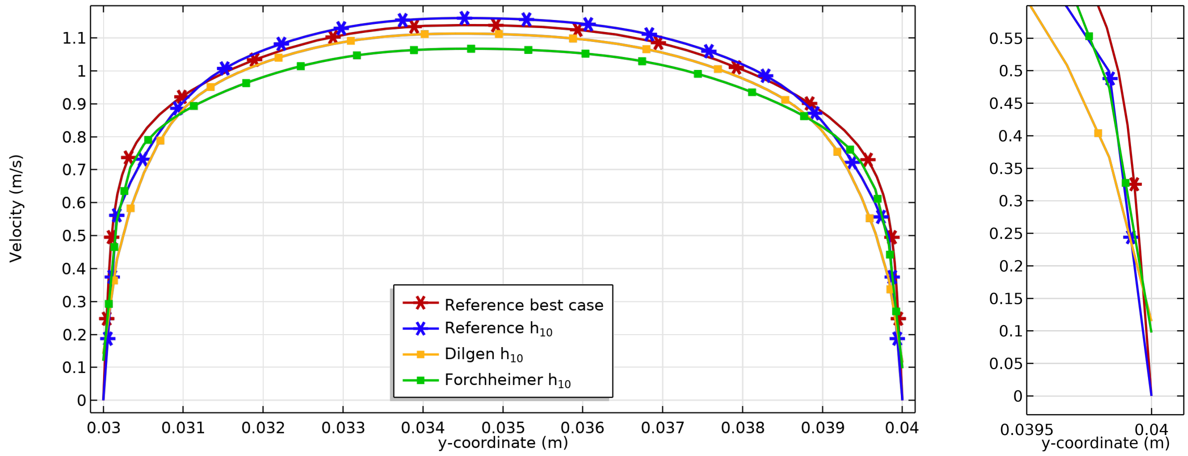

(c) Velocity profile for h_{10}

(d) Velocity profile for h_{10}

Figure E.5: Velocity profile in the upper channel with the Forchheimer method

In Table E.5 the RRMSE regarding the Forchheimer method can be obtained. The errors in the upper channel are compared to the Dilgen method and do not show a significant improvement. In the lower channel the errors for the Forchheimer method are increased, where it actually was expected to perform better in the lower channel since in the lower channel more turbulence and thus more inertial forces are present.

Table E.5: RRMSE of the velocity on the cut lines in the upper and lower channel

		Forchheimer method		**Dilgen method**	
Location	**w.r.t.**	h_5	h_{10}	h_5	h_{10}
Upper channel	Reference best case	4.31 %	6.24 %	4.62 %	6.33 %
	Reference h_x case	4.30 %	7.37 %	4.48 %	4.77 %
Lower channel	Reference best case	16.57 %	26.03 %	11.13 %	14.34 %
	Reference h_x case	16.17 %	24.11 %	10.12 %	9.50 %

Specific dissipation rate (ω)

The specific dissipation rate in this method did not improve significantly on the Dilgen method. Figure E.6 showed that the specific dissipation rate value at the wall for both h_x cases is slightly increased and it gets closer to the reference simulation slightly of the wall.

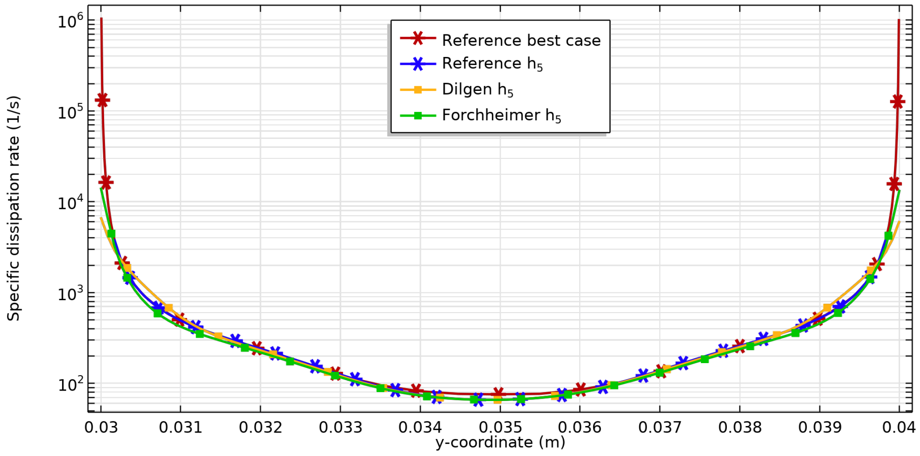

(a) Specific dissipation rate h_5

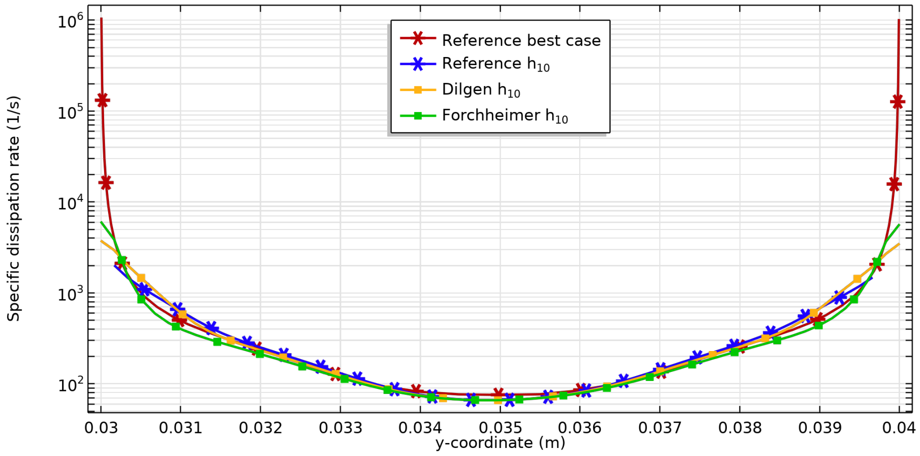

(b) Specific dissipation rate h_{10}

Figure E.6: Specific dissipation rate in the upper channel with the Forchheimer method

The RRMSE shows that this method is not an improvement when compared to the Dilgen method as can be seen in Table E.6.

Table E.6: RRMSE of the specific dissipation rate on the cut lines in the upper and lower channel

		Forchheimer method		**Dilgen method**	
Location	**w.r.t.**	h_5	h_{10}	h_5	h_{10}
Upper channel	Reference best case	97.95 %	99.04 %	98.99 %	99.39 %
	Reference h_x case	96.99 %	98.61 %	98.51 %	99.11 %
Lower channel	Reference best case	98.00 %	99.20 %	99.03 %	99.49 %
	Reference h_x case	97.07 %	98.84 %	98.56 %	99.26 %

Turbulent kinetic energy (k)

The turbulent kinetic energy with the Forchheimer did improve on the Dilgen method. Especially in the region where the inertial forces are present and where gray elements are present the turbulent kinetic energy is improved. This can be seen in Figure E.7 where the Dilgen method has large peaks in this area.

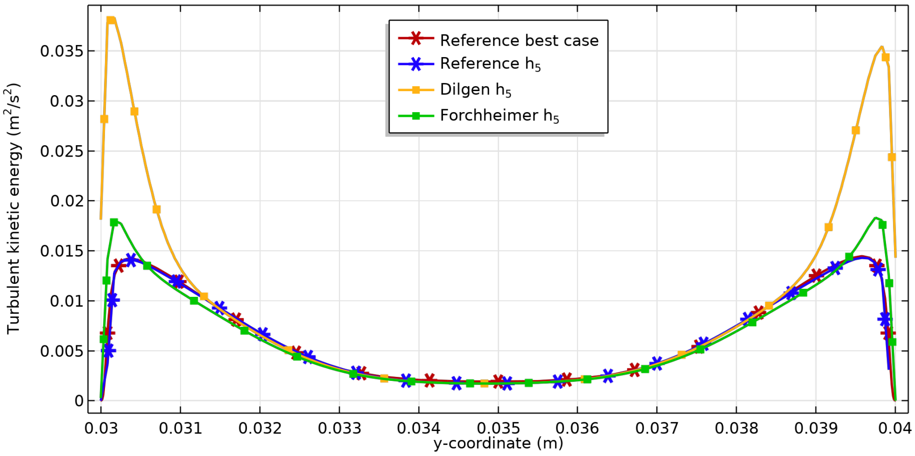

(a) Turbulent kinetic energy for h_5

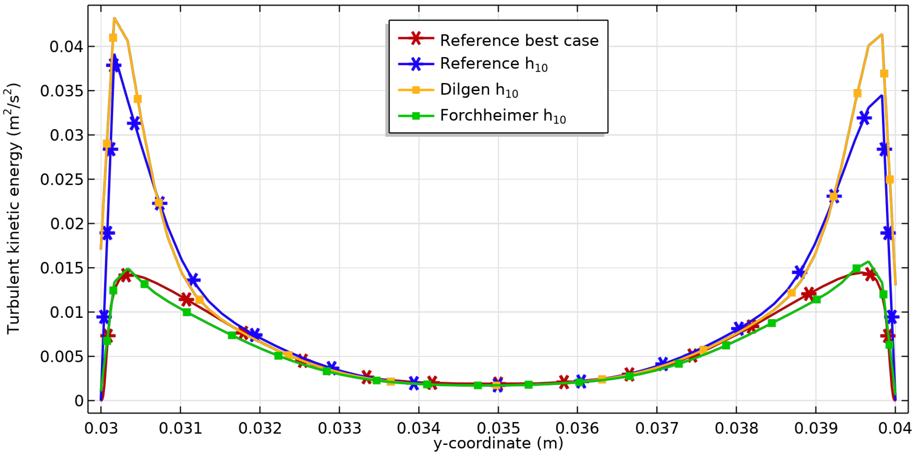

(b) Turbulent kinetic energy for h_{10}

Figure E.7: Turbulent kinetic energy in the upper channel with the Forchheimer method

Visually expecting the cut lines already showed that the turbulent kinetic energy was improved when compared to the Dilgen method, which is verified by the RRMSE of the turbulent kinetic energy in Table E.7. The error for the h_5 case is 18.08% with respect to the reference best case where in the Dilgen method this is 91.92%.

Table E.7: RRMSE of the turbulent kinetic energy on the cut lines in the upper and lower channel

		Forchheimer		**Dilgen**	
Location	**w.r.t.**	h_5	h_{10}	h_5	h_{10}
Upper channel	Reference best case	18.08 %	9.06 %	91.92 %	111.65 %
	Reference h_x case	20.90 %	49.52 %	95.07 %	18.82 %
Lower channel	Reference best case	34.89 %	48.04 %	43.89 %	67.11 %
	Reference h_x case	30.31 %	35.73 %	36.40 %	22.32 %

E.2.2. Discussion on the Forchheimer method

The Forchheimer method showed various results, the velocity profiles and specific dissipation rates did not improve significantly on the Dilgen method. On the contrary the turbulent kinetic energy improved impressively, where the peaks in turbulent kinetic energy might be caused by inertial forces and this is exactly what the Forchheimer effect counters. Unfortunately this method can not be concluded as a large improvement on the Dilgen method when considering the overall results.

Table E.8: RRMSE Forchheimer method with respect to reference best case and reference with corresponding h_x mesh

		Forchheimer			**Dilgen**		
w.r.t.	h_x	**RRMSE** U	**RRMSE** k	**RRMSE** ω	**RRMSE** U	**RRMSE** k	**RRMSE** ω
reference best case	h_5	15.03 %	33.48 %	98.44 %	10.39 %	48.22 %	99.24 %
	h_{10}	24.28 %	45.75 %	98.02 %	13.26 %	75.91 %	98.78 %
reference h_x case	h_5	14.46 %	29.86 %	98.53 %	9.62 %	43.57 %	99.31 %
	h_{10}	21.31 %	42.15 %	97.64 %	8.63 %	30.88 %	98.57 %

E.3. Forchheimer combined with dilation method

The previous method showed that the Forchheimer method is capable of increasing the performance on the turbulent kinetic energy but not on the specific dissipation rate. In this final method the Forchheimer method is combined with the dilation method, from now on referred to as the F-D method. The dilation is applied to the ω penalization and has the same conditions as presented in Section 5.1, thus the projection slope is 80 and the projection threshold is 0.9.

E.3.1. Results on the Forchheimer with dilation method

The results of the velocity, specific dissipation rate and turbulent kinetic energy for the F-D method will be discussed in this section.

Velocity (U)

The velocity profiles for this final method are shown in Figure E.8 where the velocity profile for both h_x cases did not improve. It can be seen that the velocity in the middle of the channel is lower that the reference simulations and thus does not match. Furthermore, directly after the dilation stops a undesired bend in the velocity profile can be noticed. Finally, the velocity did not reach the boundary condition of zero velocity at the wall with this method.

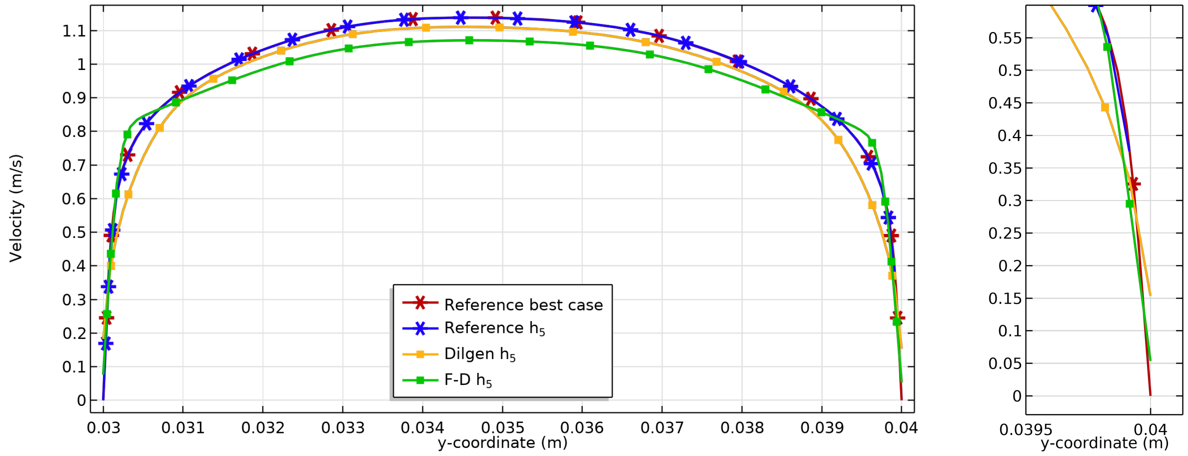

(a) Velocity profile for h_5

(b) Velocity profile at the wall for h_5

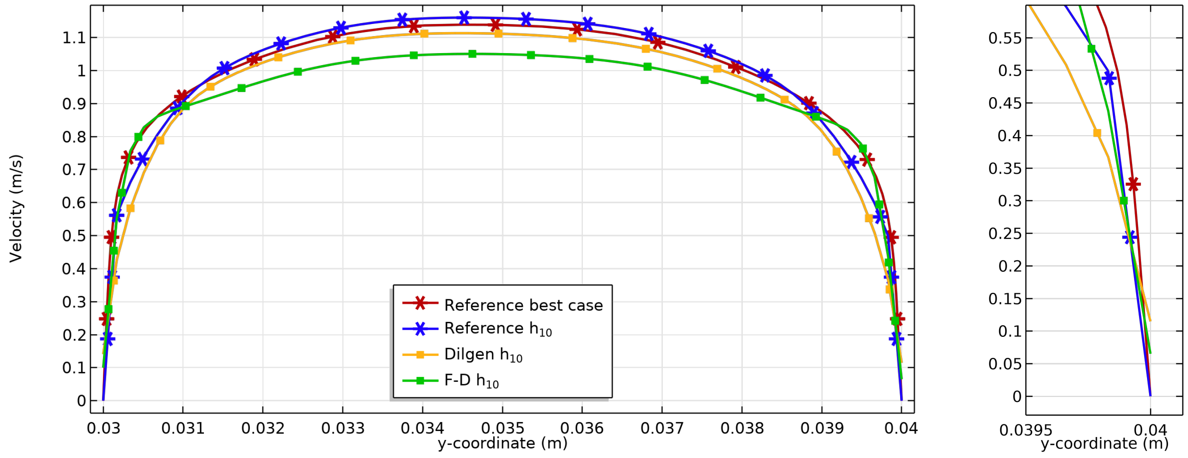

(c) Velocity profile for h_{10}

(d) Velocity profile at the wall for h_{10}

Figure E.8: Velocity profile in the upper channel with the F-D method

The RRMSE are presented in Table E.9 which shows that all errors are increased when compared to the Dilgen method. Thus can be concluded that this method is not an improvement for the velocity profile.

Table E.9: RRMSE of the velocity on the cut lines in the upper and lower channel

		F-D method		**Dilgen method**	
Location	**w.r.t.**	h_5	h_{10}	h_5	h_{10}
Upper channel	Reference best case	5.53 %	7.20 %	4.62 %	6.33 %
	Reference h_x case	5.53 %	8.81 %	4.48 %	4.77 %
Lower channel	Reference best case	24.35 %	32.36 %	11.13 %	14.34 %
	Reference h_x case	23.64 %	29.41 %	10.12 %	9.50 %

Specific dissipation rate (ω)

The specific dissipation rate in this method is capable of reaching higher values at the wall which is due to the dilation filter. However, the Forchheimer penalization is active in the region shortly after the wall which results in a different behavior than desired. It can be seen that the specific dissipation rate is to high in this region especially for the h_{10} case in Fig. E.9b.

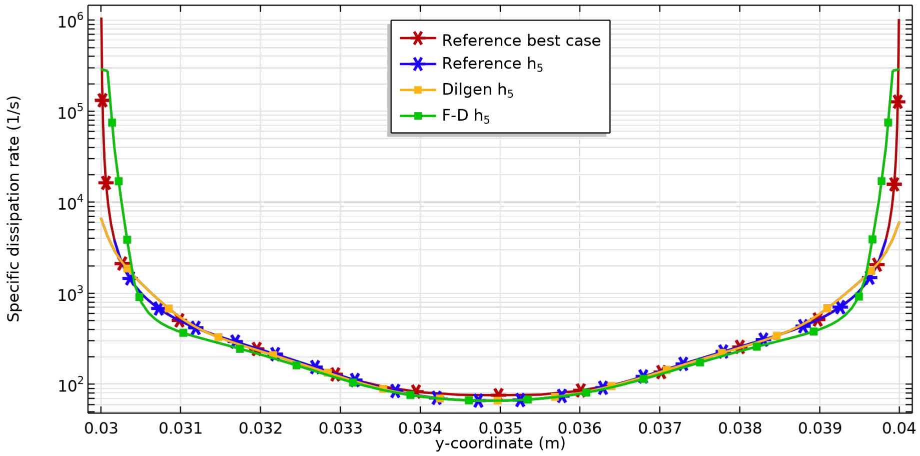

(a) Specific dissipation rate for h_5

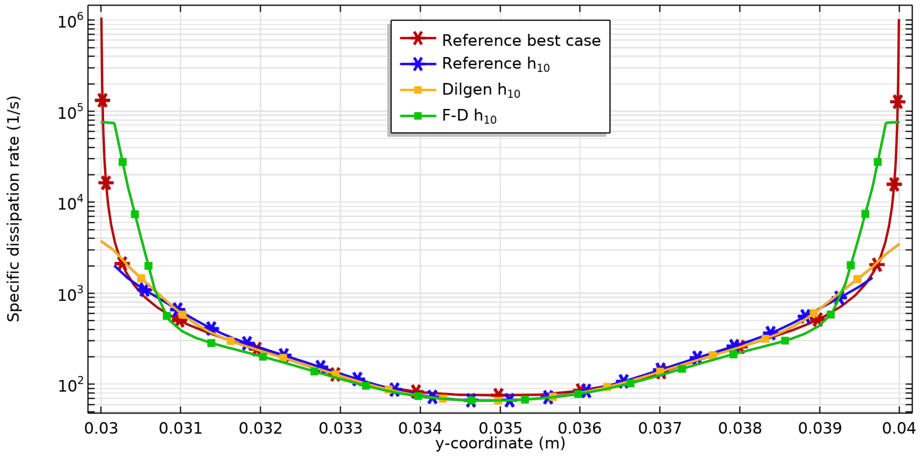

(b) Specific dissipation rate for h_{10}

Figure E.9: Specific dissipation rate in the upper channel with the F-D method for h_5

The RRMSE for the specific dissipation rate can be obtained in Table E.10 which exceed the 100% for all h_5 cases.

Table E.10: RRMSE of the specific dissipation rate on the cut lines in the upper and lower channel

Location	**w.r.t.**	h_5	h_{10}
Upper channel	Reference best case	113.83 %	95.97 %
	Reference h_x case	142.63 %	98.79 %
Lower channel	Reference best case	113.75 %	96.05 %
	Reference h_x case	143.19 %	99.03 %

Turbulent kinetic energy (k)

Finally, the turbulent kinetic energy for this method can be found in Figure E.10. Since the turbulent kinetic energy performed already quite impressive with the normal Forchheimer method it is no surprise that in combination with the dilation the turbulent kinetic energy dampens to much, this behavior is seen for both h_x cases. In the middle of the channel the turbulent kinetic energy corresponds to the reference simulations.

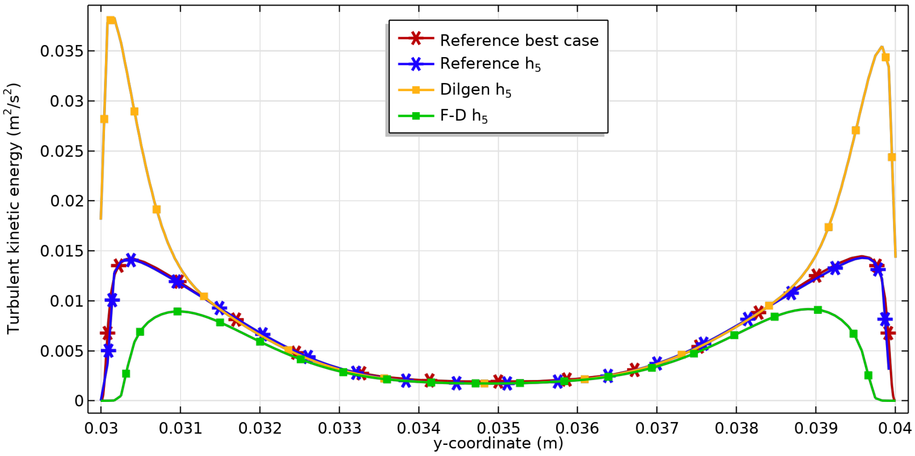

(a) Turbulent kinetic energy for h_5

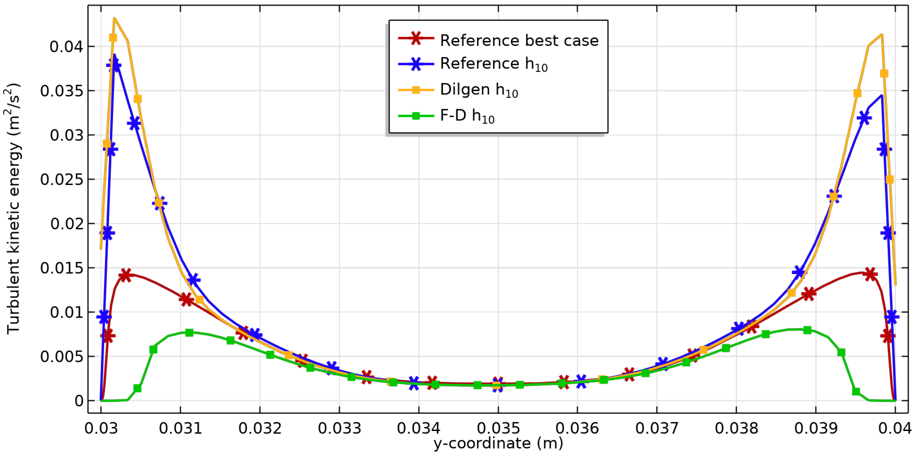

(b) Turbulent kinetic energy for h_{10}

Figure E.10: Turbulent kinetic energy in the upper channel with the F-D method for h_5 and h_{10}

The RRMSE shows indeed that the turbulent kinetic energy is dampens to much now, where the errors increased again after they decreased in the Forchheimer method, shown in Table E.11.

Table E.11: RRMSE of the turbulent kinetic energy on the cut lines in the upper and lower channel

		F-D method		**Dilgen method**	
Location	**w.r.t.**	h_5	h_{10}	h_5	h_{10}
Upper channel	Reference best case	47.67 %	60.63 %	91.92 %	111.65 %
	Reference h_x case	46.62 %	83.63 %	95.07 %	18.82 %
Lower channel	Reference best case	60.90 %	57.45 %	43.89 %	67.11 %
	Reference h_x case	56.01 %	59.95 %	36.40 %	22.32 %

E.3.2. Discussion on the Forchheimer combined dilation method

The F-D method can not be noticed as an improvement, in fact the results became worse. Especially in the turbulent kinetic energy case where the normal Forchheimer method did improve on the Dilgen method, the F-D method dampens the turbulent kinetic energy to much. The overall RRMSE table for this method, which is shown in Table E.12, shows that the errors did increase. It can thus be concluded that in this case the F-D method can not be assigned as an improvement on the Dilgen method.

Table E.12: RRMSE F-D method with respect to reference best case and reference with corresponding h_x mesh

		F-D method			Dilgen method		
w.r.t.	h_x	**RRMSE** U	**RRMSE** k	**RRMSE** ω	**RRMSE** U	**RRMSE** k	**RRMSE** ω
reference	h_5	23.88 %	55.95 %	95.28 %	10.39 %	48.22 %	99.24 %
best case	h_{10}	31.05 %	55.49 %	94.70 %	13.26 %	75.91 %	98.78 %
reference	h_5	23.29 %	52.63 %	94.68 %	9.62 %	43.57 %	99.31 %
h_x case	h_{10}	27.64 %	64.79 %	97.17 %	8.63 %	30.88 %	98.57 %

F

Additional data of the pressure drop minimization around an internal wall case

In this chapter additional information regarding the topology optimization case of the pressure drop minimization around an internal wall is presented. First in Section F.1 the intermediate designs for each projection slope are presented. Secondly, in Section F.2 the convergence plots are shown.

F.1. Intermediate designs

In this section the intermediate designs of the TO case of the pressure drop minimization around an internal wall are shown. In Figures F.1 and F.2 the intermediate designs of the Dilgen method are shown. In Figure F.3 the intermediate designs of the MDI-D method are shown.

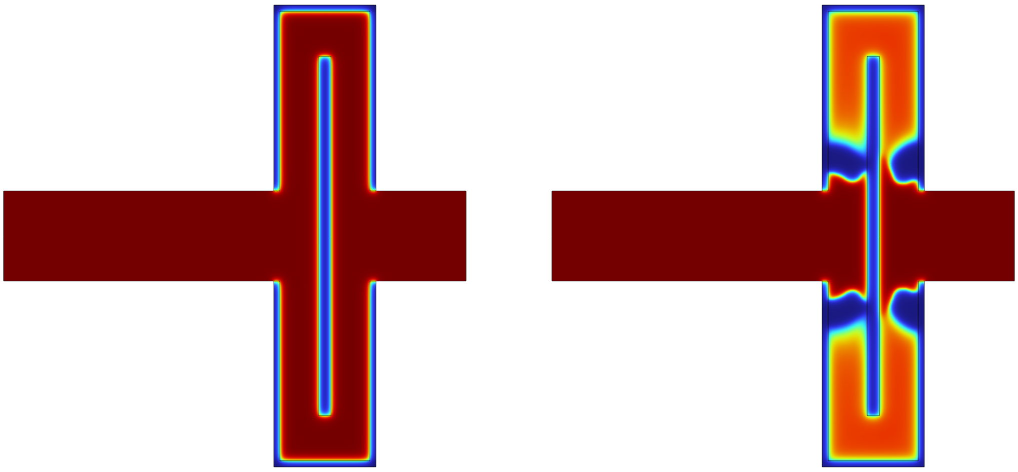

(a) Initial design.

(b) Design $\beta = 2$.

Figure F.1: Intermediate designs with the Dilgen method of the pressure drop minimization around internal wall case

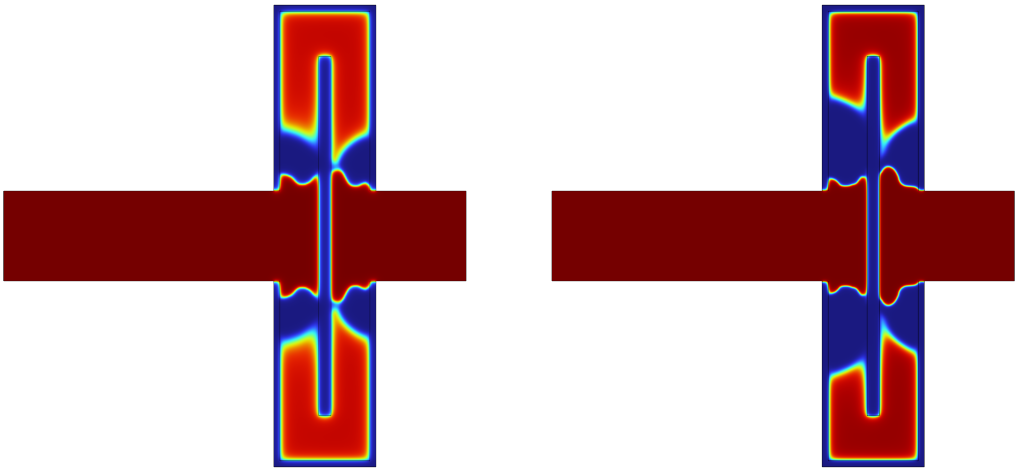

(a) Design $\beta = 4$. (b) Design $\beta = 6$.

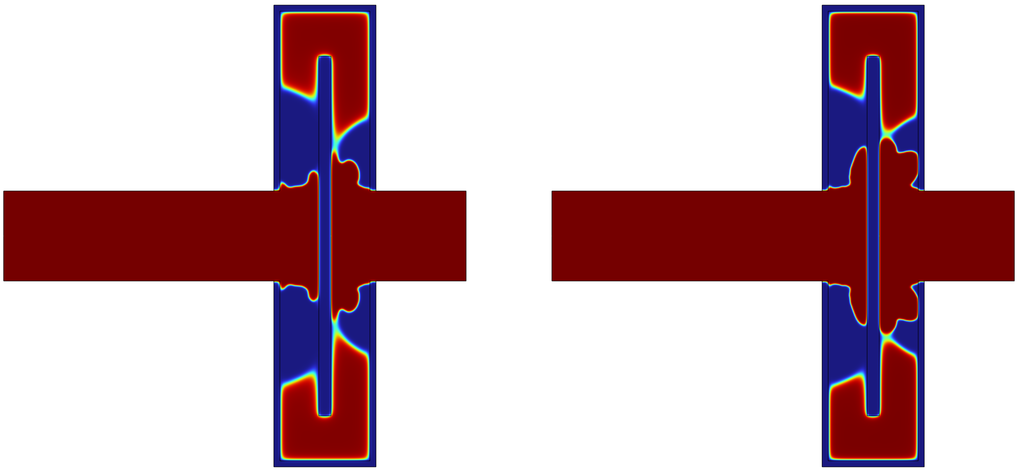

(c) Design $\beta = 8$. (d) Design $\beta = 10$.

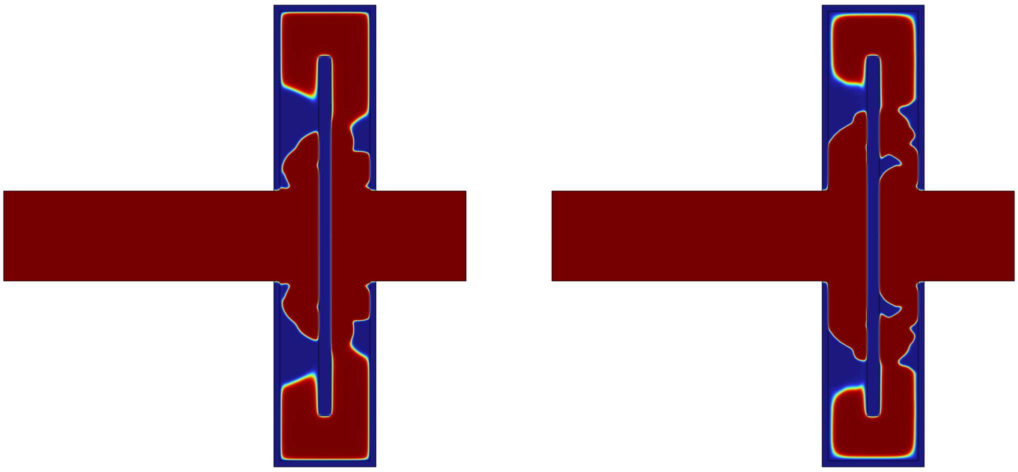

(e) Design $\beta = 12$. (f) Design $\beta = 14$.

Figure F.2: Intermediate designs with the Dilgen method of the pressure drop minimization around internal wall case

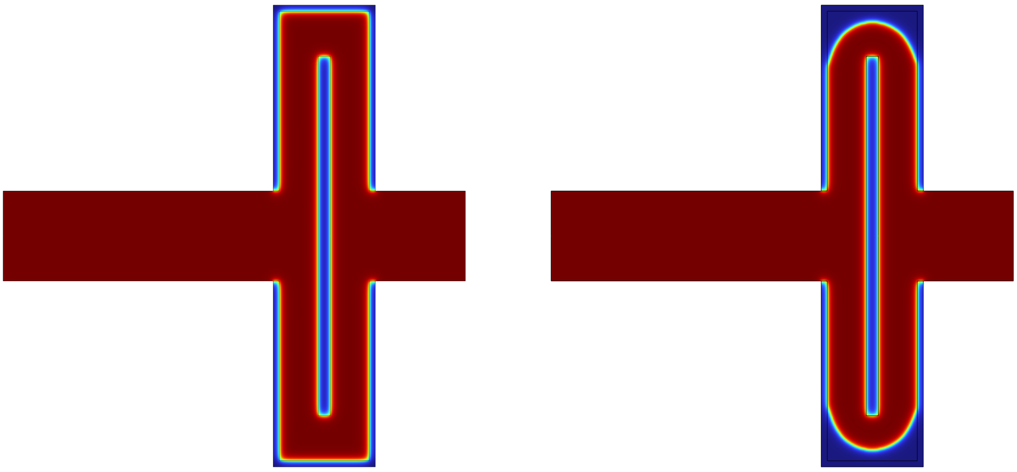

(a) Initial design. (b) Design $\beta = 2$.

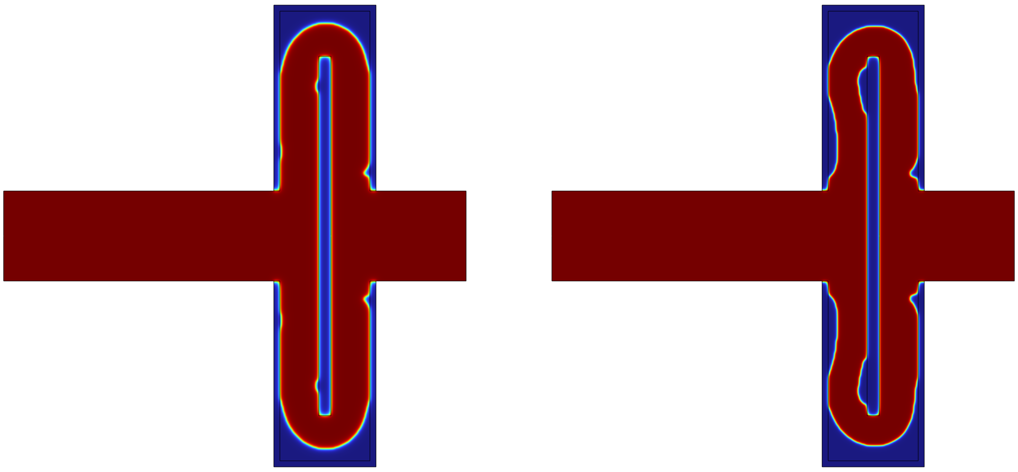

(c) Design $\beta = 4$. (d) Design $\beta = 6$.

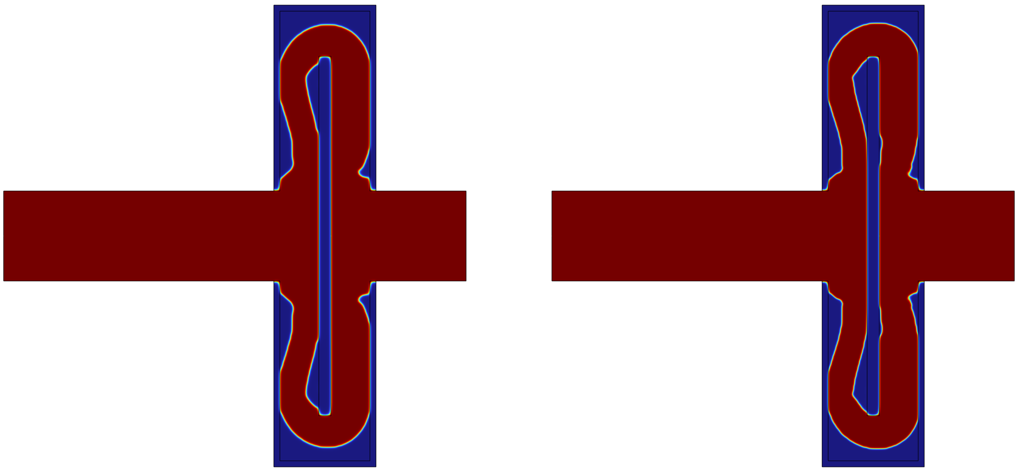

(e) Design $\beta = 8$. (f) Design $\beta = 10$.

Figure F.3: Intermediate designs with the MDI-D method of the pressure drop minimization around internal wall case

F.2. Convergence plots

In this section the convergence plots of the pressure drop minimization around an internal wall case are shown. First the convergence plot with the Dilgen method is shown in Figure F.4. Secondly, the convergence plot with the MDI-D method is shown in Figure F.5.

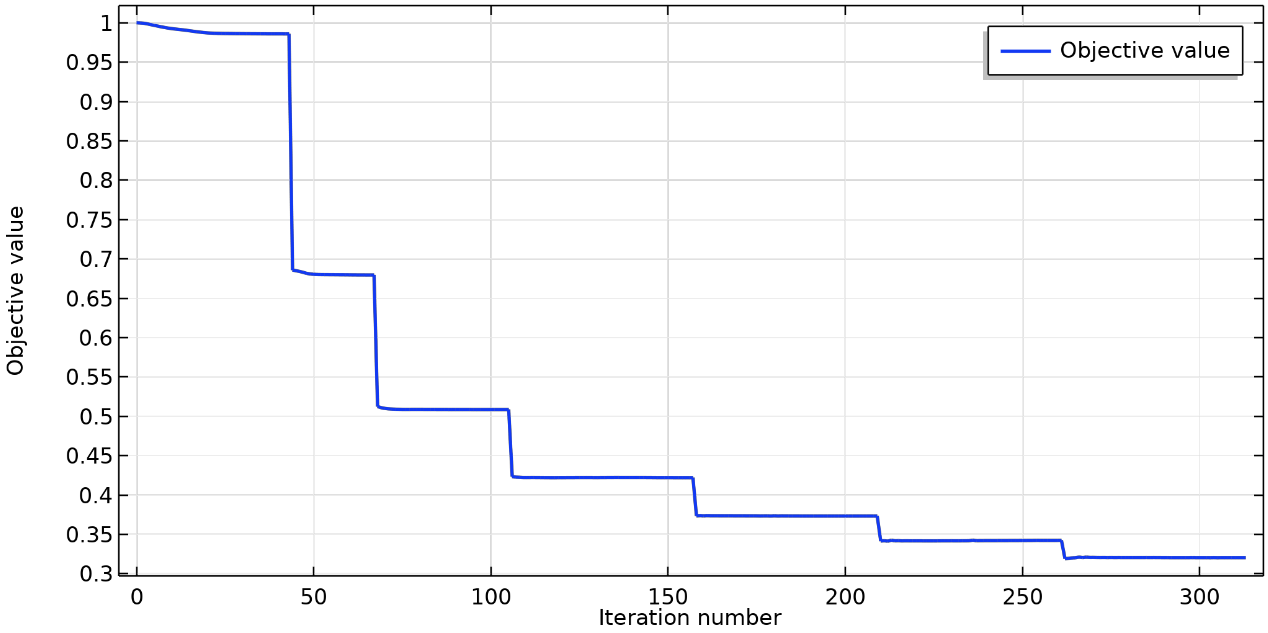

Figure F.4: Convergence plot of the Dilgen method in the TO pressure drop minimization around an internal wall case

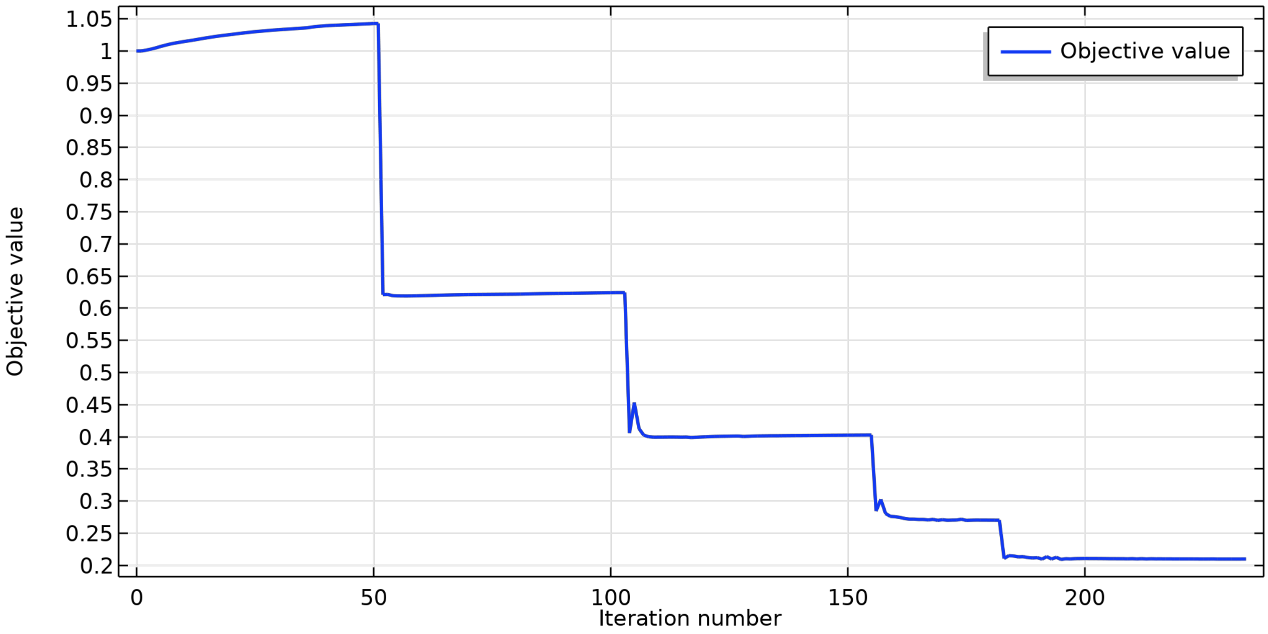

Figure F.5: Convergence plot of the MDI-D method in the TO pressure drop minimization around an internal wall case

Bibliography

[1] Thomas B. van der Hout. Mitigating weaknesses of density-based thermo-fluid topology optimization. Master's thesis, Delft University of Technology, 2021.

[2] Cetin B Dilgen, Sumer B Dilgen, David R Fuhrman, Ole Sigmund, and Boyan S Lazarov. Topology optimization of turbulent flows. *Computer Methods in Applied Mechanics and Engineering*, 331:363–393, 2018.

[3] Thomas B. van der Hout. Topology Optimization methods for cooling of a SiC transistor Power Module. Technical report, Delft University of Technology, 2019.

[4] Martin Philip Bendsøe and Ole Sigmund. *Topology Optimization: Theory, Methods and Applications*. Springer, 2003.

[5] Stanley Osher and James A Sethian. Fronts propagating with curvature-dependent speed: Algorithms based on hamilton-jacobi formulations. *Journal of computational physics*, 79(1):12–49, 1988.

[6] Nico P Van Dijk, Kurt Maute, Matthijs Langelaar, and Fred Van Keulen. Level-set methods for structural topology optimization: a review. *Structural and Multidisciplinary Optimization*, 48:437–472, 2013.

[7] Krister Svanberg. The method of moving asymptotes—a new method for structural optimization. *International journal for numerical methods in engineering*, 24(2):359–373, 1987.

[8] Martin Philip Bendsøe and Noboru Kikuchi. Generating optimal topologies in structural design using a homogenization method. *Computer methods in applied mechanics and engineering*, 71(2):197–224, 1988.

[9] Robert Krol. Topology optimization of turbulent-flow cooling systems. Technical report, Delft University of Technology, 2021.

[10] Sumer B Dilgen, Cetin B Dilgen, David R Fuhrman, Ole Sigmund, and Boyan S Lazarov. Density based topology optimization of turbulent flow heat transfer systems. *Structural and Multidisciplinary Optimization*, 57:1905–1918, 2018.

[11] Thomas van der Hout. TopOpt_Tradeoff. Technical report, 2019. [Unpublished].

[12] CFD Module User's Guide. Technical report, COMSOL, 2018.

[13] CCM USER GUIDE. Technical report, Siemens, 2006.

[14] Openfoam: User guide v2112. Technical report, OpenFOAM, 2022.

[15] Autodesk. Turbulence, 2022. URL `https://knowledge.autodesk.com/support/cfd/learn-explore/caas/CloudHelp/cloudhelp/2021/ENU/SimCFD-UsersGuide/files/The-CFD-Process/Solving-the-Simulation/Solve-Quick-Edit-dialog-Physics/GUID-E9E8ACA1-8D49-4A49-8A35-52DB1A2C3E5F-html.html`.

[16] Osman YUKSEL. An overview on topology optimization methods employed in structural engineering. *Kırklareli Üniversitesi Mühendislik ve Fen Bilimleri Dergisi*, 5(2):159–175, 2019.

[17] A Çengel Yunus. *Heat and mass transfer: fundamentals and applications*. McGraw-Hill Education, 2019.

[18] Frank M. White. *Fluid Mechanics*. McGraw Hill, 2011.

[19] Christopher I Trombley and Maria L Ekiel-Jeżewska. Basic concepts of stokes flows. *Flowing Matter*, pages 35–50, 2019.

[20] FT Nieuwstadt, BJ Boersma, and J Westerweek. *Introduction to Theory and Applications of Turbulent Flows*. Springer, 2016.

[21] Henk Kaarle Versteeg and Weeratunge Malalasekera. *An introduction to computational fluid dynamics: the finite volume method*. Pearson education, 2007.

[22] E Fares and W Schröder. A differential equation for approximate wall distance. *International journal for numerical methods in fluids*, 39(8):743–762, 2002.

[23] Jonas Bredberg. On the wall boundary condition for turbulence models. *Chalmers University of Technology, Department of Thermo and Fluid Dynamics. Internal Report 00/4. Göteborg*, pages 8–16, 2000.

[24] Hermann Schlichting and Joseph Kestin. *Boundary layer theory*, volume 121. Springer, 1961.

[25] Hendrik Tennekes, John Leask Lumley, Jonh L Lumley, et al. *A first course in turbulence*. MIT press, 1972.

[26] Dmitri Kuzmin, Otto Mierka, and Stefan Turek. On the implementation of the κ-ε turbulence model in incompressible flow solvers based on a finite element discretisation. *International Journal of Computing Science and Mathematics*, 1(2-4):193–206, 2007.

[27] Jousef M. What is y+ (yplus)? URL `https://www.simscale.com/forum/t/what-is-y-yplus/82394`.

[28] Arnau Bayón. Wall functions | Introduction to CFD. URL `https://cfd.blogs.upv.es/turbulence/wall-functions/`.

[29] Thomas Borrvall and Joakim Petersson. Topology optimization of fluids in stokes flow. *International journal for numerical methods in fluids*, 41(1):77–107, 2003.

[30] Laurits Højgaard Olesen, Fridolin Okkels, and Henrik Bruus. A high-level programming-language implementation of topology optimization applied to steady-state navier–stokes flow. *International Journal for Numerical Methods in Engineering*, 65(7):975–1001, 2006.

[31] Tsuguo Kondoh, Tadayoshi Matsumori, and Atsushi Kawamoto. Drag minimization and lift maximization in laminar flows via topology optimization employing simple objective function expressions based on body force integration. *Structural and Multidisciplinary Optimization*, 45:693–701, 2012.

[32] Hao Li, Xiaohong Ding, Fanzhen Meng, Dalei Jing, and Min Xiong. Optimal design and thermal modelling for liquid-cooled heat sink based on multi-objective topology optimization: An experimental and numerical study. *International Journal of Heat and Mass Transfer*, 144:118638, 2019.

[33] Florian R Menter. Two-equation eddy-viscosity turbulence models for engineering applications. *AIAA journal*, 32 (8):1598–1605, 1994.

[34] Allan Gersborg-Hansen, Ole Sigmund, and Robert B Haber. Topology optimization of channel flow problems. *Structural and multidisciplinary optimization*, 30:181–192, 2005.

[35] Alejandro Diaz and Ole Sigmund. Checkerboard patterns in layout optimization. *Structural optimization*, 10:40–45, 1995.

[36] Boyan Stefanov Lazarov and Ole Sigmund. Filters in topology optimization based on helmholtz-type differential equations. *International Journal for Numerical Methods in Engineering*, 86(6):765–781, 2011.

[37] Fengwen Wang, Boyan Stefanov Lazarov, and Ole Sigmund. On projection methods, convergence and robust formulations in topology optimization. *Structural and multidisciplinary optimization*, 43:767–784, 2011.

[38] M. Padhma. End-to-end introduction to evaluating regression models. URL `https://www.analyticsvidhya.com/blog/2021/10/evaluation-metric-for-regression-models/#:~:text=RelativeRootMeanSquareError,tocomparedifferentmeasurementtechniques.`

[39] Anders Clausen, Niels Aage, and Ole Sigmund. Topology optimization of coated structures and material interface problems. *Computer Methods in Applied Mechanics and Engineering*, 290:524–541, 2015.

[40] Maarten J.B. Theulings. Towards improved porous models for solid/fluid topology optimization. 2022. [Unpublished].

[41] Djaïr Wijbenga. Design and verification of topology optimized liquid cooling infrastructure for high power density power modules. Master's thesis, Eindhoven University of Technology, 2021.

[42] Nicolas Huc. Conjugate Heat Transfer. 2014. URL `https://www.comsol.com/blogs/conjugate-heat-transfer/`. `https://www.comsol.com/blogs/conjugate-heat-transfer/`.

[43] Gil Ho Yoon. Topological design of heat dissipating structure with forced convective heat transfer. *Journal of Mechanical Science and Technology*, 24(6):1225–1233, 2010.

[44] David C Wilcox et al. *Turbulence modeling for CFD*, volume 2. DCW industries La Canada, CA, 1998.

[45] Turbulence intensity, 2022. URL `https://www.cfd-online.com/Wiki/Turbulence_intensity`.

[46] Diego Hayashi Alonso and Emílio Carlos Nelli Silva. Topology optimization applied to the design of tesla-type turbine devices. *Applied Mathematical Modelling*, 103:764–791, 2022.